(12)

STANFORD/NASA AMES JOINT INSTITUTE FOR SURFACE AND MICROSTRUCTURE RESEARCH
DEPARTMENT OF MATERIALS SCIENCE AND ENGINEERING
STANFORD UNIVERSITY
STANFORD, CA 94305

FABRICATION AND PROPERTIES OF MULTILAYER STRUCTURES

prepared by

W. A. Tiller

August 1982

SU-DMS-82-R-4

First Semiannual Technical Report for Period 1 September 1981 - 28 February 1982

prepared for

ADVANCED RESEARCH PROJECTS AGENCY
1400 Wilson Boulevard
Arlington, VA 22209

Department of MATERIALS SCIENCE AND ENGINEERING
STANFORD UNIVERSITY

SU-DMS-82-R-4

FIRST
SEMIANNUAL TECHNICAL REPORT
ON
FABRICATION AND PROPERTIES OF MULTILAYER STRUCTURES

1 September 1981 - 28 February 1982

This research was sponsored by the
Defense Advanced Research Projects
Agency under ARPA Order No. 3706
Contract No. MDA903-81-C-0578
Monitor: ONR Resident Representative

Contractor: Stanford University

Effective Date of Contract: September 1, 1981

Contract Expiration Date: September 30, 1982

Principal Investigator: William A. Tiller

Phone: (415) 497-3901

Stanford/NASA Ames Joint Institute for Surface and Microstructure Research
Department of Materials Science and Engineering
Stanford University, Stanford, CA 94305

UNCLASSIFIED
SECURITY CLASSIFICATION OF THIS PAGE (*When Data Entered*)

REPORT DOCUMENTATION PAGE

READ INSTRUCTIONS
BEFORE COMPLETING FORM

1. REPORT NUMBER
SU-DMS-82-R-4

2. GOVT ACCESSION NO.
AD-A120 779

3. RECIPIENT'S CATALOG NUMBER

4. TITLE (*and Subtitle*)
FABRICATION AND PROPERTIES OF
MULTILYAER STRUCTURES

5. TYPE OF REPORT & PERIOD COVERED
1st Semiannual Technical Report (9/1/81 - 2/28/82)

6. PERFORMING ORG. REPORT NUMBER

7. AUTHOR(*s*)
W. A. Tiller, T. W. Barbee, Jr., T. Halicioglu, L. Landsberger, C. Lee, G. McGlinn, A. Savan, K. Seaward

8. CONTRACT OR GRANT NUMBER(*s*)
MDA903-81-C-0578

9. PERFORMING ORGANIZATION NAME AND ADDRESS
Stanford/NASA
AMES Joint Institute for Surface and Microstructure
Research, Department of Materials Science & Engrg.
Stanford University, Stanford, CA 94305

10. PROGRAM ELEMENT, PROJECT, TASK AREA & WORK UNIT NUMBERS

11. CONTROLLING OFFICE NAME AND ADDRESS
Advanced Research Projects Agency (ARPA)
1400 Wilson Boulevard
Arlington, VA 22209

12. REPORT DATE
August 1982

13. NUMBER OF PAGES
116

14. MONITORING AGENCY NAME & ADDRESS(*if different from Controlling Office*)

15. SECURITY CLASS. (*of this report*)
Unclassified

15a. DECLASSIFICATION/DOWNGRADING SCHEDULE

16. DISTRIBUTION STATEMENT (*of this Report*)
Unlimited Distribution

17. DISTRIBUTION STATEMENT (*of the abstract entered in Block 20, if different from Report*)

18. SUPPLEMENTARY NOTES This contract is awarded under Basic Agreement No. 12740-01-0 dated 81-09-01, amended by modifications P00001 and P00002, issued by the Office of Naval Research. This research is sponsored by the Defense Advanced Research Projects Agency (DARPA).

19. KEY WORDS (*Continue on reverse side if necessary and identify by block number*)
REACTIVE SPUTTERING, FILM FORMATION, SILICON DIOXIDE, SILICON CARBIDE, SEMICONDUCTOR PROCESSING, THERMAL OXIDATION, INTERSTITIAL SPECIES, CRYSTALLOGRAPHY, MOLECULAR ORBITALS, AMORPHOUS FILMS, INTEGRATED CIRCUITS

20. ABSTRACT (*Continue on reverse side if necessary and identify by block number*)

This program has as its goal the development of vapor deposition processes for application to integrated circuit technology. Its purpose is to investigate vapor deposition techniques that offer potential for synthesis of materials having new, unique structures and/or of higher quality than currently attainable. Technological application of these materials will be a significant consideration in the selection of specific systems for study.

This report focuses on five individual work areas: (i) synthesis of SiO_x, (ii) synthesis of SiC, (iii) synthesis of Pd_2Si, (iv) electrical diagnostics of films, and (v) computer simulation of film synthesis.

INTRODUCTION

Despite the unfortunate circumstances of being unable to use the Vapor Phase Synthesis Laboratory for the months of October through January because of construction in that portion of the McCullough building, considerable progress has been achieved during the past six months. This report focuses on five individual work areas (i) synthesis of SiO_x, (ii) synthesis of SiC, (iii) synthesis of Pd_2Si, (iv) electrical diagnostics of films, and (v) computer simulation of film synthesis. In the SiO_2 area we have found that the film thickness is proportional to T^{-1} with an activation energy of 1.5 kcal/mole, that the film uniformity increased with P_{O_2} increases and that IR transmission spectra showed a spectral shift to higher wave numbers as the deposition temperature increased. In the SiC area, single source deposition led to β-SiC films with a (111) texture and measurements led to data on (a) film stoichiometry, (b) refractive index, (c) film structure and morphology, and (d) sheet resistivity. Steady progress has been made and the addition of tin as a mobility enhancer has produced the best quality film to date. Work has begun on the synthesis of (Pd, Pt, Ir) silicides and dual source deposition of Pd and Si has developed the composition and phase spread in that binary system. In the area of electrical diagnostics, theoretical review of the I-V, C-V and AC conductivity characteristics for p/n junction, heterojunction and metal insulator semiconductor diodes has been conducted and experimental measurements has been made on SiO_x MIS diodes. Another new area of study has been computer simulation of film synthesis where a number of new software programs have been developed. In addition, a special parametric study of a multilayer structure representing the Cu/Ag system has been conducted and special potential energy functions have been developed for the Si-O system in order to study its unique structural features.

A. EXPERIMENTAL RESULTS

1. Reactive Sputter Deposition of Oxide Films

(a) SiO_x via Simultaneous Deposition/Reaction

A number of experimental modifications have been made relative to the sputtering chamber configuration reported on previously(1) (see Fig. 1). An Argon ion gun was added for the removal of native oxide prior to deposition. This necessitated making flexible power leads for the substrate heater so that it could be rotated from under the ion gun to a position beneath the target. Nickel heat shields, having relatively inert oxides at high temperatures, were fabricated for the heater. In addition, a rectangular quartz oxygen dispersion ring was made in order to enhance deposition uniformity over the rectangular area dictated by the heater (see Fig. 1).

To ensure native oxide removal, an investigation of ion gun operating conditions was made. The critical variables were determined to be (a) ion gun to substrate distance, (b) ion gun power, and to a lesser extent, (c) chamber pressure. The thermal oxide etching rates for various ion gun etching parameters are given in Table 1. Etch rates of approximately 14 Å/min. were obtained at a 4 inch operating distance for the ion gun at 2kV and 2mA and the Argon chamber pressure at 4μm and 8μm. At a 5 inch operating distance, 2kV and 2mA, the etch rate was only 3 Å/min. for an Argon chamber pressure of 7.25μm. At a 3 inch operating distance, etch rates up to 22 Å/min. were obtained.

The thermal oxide etch profile was examined ellipsometrically and is shown in Fig. 2. Significant etching was accomplished over a region ∿1 inch diameter. For long etches, the profile was quite steeply sloped with a spot ∿ one-fourth inch diameter exhibiting a maximum and uniform etch. The effect of Argon chamber pressure on etch spot size or etch rate was negligible for Argon pressure variations in the range 4μm-8μm. It was also noticed that the film index of refraction (η_f) varied with the amount of material etched (see Fig. 3) which indicates possible damage to the thermal oxide (and also the ellipsometric sensitivity to such changes).

A series of oxide depositions were made in order to investigate the influence of substrate temperature as a deposition parameter with the other conditions such that SiO_2 should form. These deposition conditions are listed in Table 2. The temperature at the substrate was varied from 25°C to 660°C using a single element quartz heater and the resulting oxide thicknesses showed a non-linear decrease with increasing temperature. X-ray diffraction indicated that all the films were amorphous and electron microprobe analysis showed the oxygen/silicon ratio to be about 2/1 except in the case of run #81-218 where the index of refraction was 1.36 (indicating porosity or excess oxygen) and the O/Si ratio was ∿5/4. Since the microprobe samples a depth of ∿0.5μ, it is likely that the Si substrate was involved in the results of samples #81-220 and #81-221.

Because nickel has a high sputtering yield, the silicon mask shown in Fig. 4 was fabricated. A piece of quartz used to define a thickness step for step profile thickness measurements (ellipsometric calibrated). Using the ion gun parameters reported above, conditions of operation to achieve etching were chosen (3 inch gun to substrate distance, 2kV/2mA beam power, 4.25μm Argon pressure, 10 minute etch) and kept constant for the next set of depositions. A method for accurately locating the ion beam center was developed which, coupled with a knowledge of the etch profile, allowed localized areas of each substrate to be compared; i.e., native oxide removed areas with native oxide present areas.

Following this, a second series of depositions were made at varying substrate temperatures concentrating on the region of apparent non-linear behavior mentioned above (100°C-200°C). In this case, comparing regions of maximum oxide thickness on each substrate, the linear dependence of film thickness vs. T^{-1} shown in Fig. 5 was observed. The activation energy for this process is ∿1.5 kcal/mole. It is believed that film #81-218 (240°C) is anomalously too thick, perhaps due to an error in experimental procedure. Again X-ray diffraction indicated that all the films were amorphous.

To investigate whether or not the oxide uniformity could be improved, the oxygen flow rate was increased leading to the result indicated in Fig. 6. At the higher oxygen flow rate, an improvement in the index of refraction constancy over the substrate surface was noted; i.e., from $\eta_f = 1.45 \pm 0.07$ at $P_{O_2} = 0.38\mu m$ to $\eta_f = 1.458 \pm 0.003$ at $P_{O_2} = 0.53\mu m$. Unfortunately, the Si target was oxidized at the higher P_{O_2} resulting in a 50% drop in oxide thickness for equal deposition times. Just recently, a new Argon outlet became available which will permit the release of Argon radially around the surface of the Si target. This should provide much better isolation of the target from oxygen released at the substrate and hence permit higher P_{O_2} values to be used without target oxidation.

Auger studies have shown the earlier SiO_x films to be uniformly dispersed on an atomic scale rather than dispersions of Si clusters in SiO_2 such as found in SIPOS material. Infrared transmission spectra studies on the amorphous SiO_2 films show that those deposited at higher temperature ($T \sim 700°C$) have a shifted spectra (to higher wave numbers) compared to those deposited at lower temperatures ($T \sim 25°C$). A typical IR spectrum for amorphous SiO_2 is shown in Fig. 7 while the data comparison for various T is shown in Fig. 8. Thus, we expect that the relative perfection of these films can be simply monitored by following the IR transmission peak shifts.

(b) SiO_x via Cyclic Deposition/Reaction

In a previous report,(1) Table III describes the synthesis conditions for SiO_x compounds by atomic layer growth. Here, the substrates are mounted on a turntable rotating at a fixed rate controlled to 0.1% and first passed beneath a sputter source of the metal atom before reaching a region where the newly deposited layer was exposed to the reactive gas, etc. The individual metal layer thickness was controlled by the rotation rate of the substrate table and the sputtering power of the metal target. The partial pressure of the reactive gas over the substrate coupled with the rate of substrate motion determined the exposure of the deposition surface. For this reason, we can consider this a cyclic deposition/reaction mode of film formation.

The process data for three of these samples are listed in Table 3 while Figs. 9 and 10 present measurements on film thickness, t_f, and index of refraction, η_f, as a function of radial distance on the wafer. The film thickness was determined by the Tally-step method. As expected, the film thickness increases and the index of refraction decreases as the rotation period decreases (more complete oxidation). The remarkably uniform index of refraction observed at the fastest rotation rate is of significant interest.

(c) ZnO_x via Simultaneous Deposition/Reaction

In Table IV of a previous report,(2) the synthesis process parameters for several ZnO_x films were tabulated and the electrical resistance of one of them (#024   ) was presented (Fig. 6).(2)

Electron microprobe results on this film as a function of radial position from the center of the wafer is given in Fig. 11 so we see that the film composition changes by ∿15% from the center to the periphery while the electrical resistance changes by a factor ∿5 over the same distance. It is the index of refraction data of Fig. 12 for this film that is most interesting. It reveals the presence of several singularities along the radial coordinate indicating that the film is rich in structural variations that need to be carefully explored.

2. Single Source Sputter Deposition of SiC Films

In a previous report,(1) the experimental arrangement and initial progress on the single source deposition of SiC was described and compared with earlier dual-source work. The dual source work had yielded a non-uniform composition, but in the region of Si:C = 1:1, the film exhibited columnar growth with ∿100 Å grain diameter and ∿500 Å grain length as 111 β-SiC preferred orientation grains at ±25° relative rotation. This region of the film had a refractive index of 2.68 and a sheet resistivity of ∿2Ω cm. The initial single-source depositions were uniform in composition, appeared stoichiometric and strong 111 preferred orientation was observed by x-ray analysis of films deposited at 700°C on (111) Si substrates cleaned in situ by Argon ion bombardment. The present report describes the continuation of the single-source work and seven of the eighteen depositions to date (see Table 4) have been selected to describe our progress.

The deposition apparatus (see Fig 13) and procedure are the same as reported previously(1) and three films have been deposited with cosputtered tin. This involves rotating the heated substrate under the ion gun for a surface clean before rotating it through the tin spray to a position under the SiC source which was peripherally located in the tin spray region. The SiC source was operated in the RF mode, nearly always at 600W, while the Sn source was operated in the DC mode at low power (∿20W). The system Argon pressure was reduced to 4μm during deposition. At the completion of deposition, the substrate was moved back under the ion gun and a slow cool-down period ensued. The latest depositions (with the tin added) showed the best film structure and properties to date.

(a) Film Analysis

A number of thin films have been deposited under various conditions as listed in Table 4. The process column describes, in order, the SiC target power, substrate temperature, source-to-substrate distance, ion gun voltage, ion etching chamber pressure and tin target power. Of the work represented by Table 4, the depositions #222-#233 were made during this reporting period. Detailed analysis of representative films (indicated with a star in Table 4) has been started where the choice was made based upon the presence of significant x-ray 111 β-SiC reflections.

(b) Film Stoichiometry

Film compositions were measured by electron microprobe and all samples, except those involving the tin source, had profiles that were flat to within the reproducibility of the technique. In Fig. 14, the data are presented for the atomic percent Si found in the representative thin films. A standard of single crystal α-SiC was used to determine the relative amounts of carbon and silicon. As seen in the figure, films 177, 178, and 228 are about 52% Si. The two samples made by cosputtering tin, 231 and 233, are quite different. These vary from 45% to 49% Si with the variation not being fully understood at this time (it may relate to surface solubility and sticking coefficient changes because of an expected tin thickness variation). The values for Si content are considered close enough to 50% to be stoichiometric SiC, except for deposition #184 at 200 watts. In this case, the Si is ∿45 At% indicating a change in the Si sticking coefficient for this lower SiC target power. As shown later, some of these samples (particularly 178 and 233) have significant β-SiC 111 x-ray reflections.

(c) Refractive Index

The refractive index of the selected samples was increased using an automated Guertner ellipsometer with a HeNe laser. To enhance the variation in ψ for an expected index ∿2.7, the measuring angle was set to 50° instead of at the usual 70° angle of incidence. These results are listed in Table 5 where we see that the refractive index values differ from the literature range of 2.65 - 2.70 for SiC.(3) The early depositions, 177 and 178, are quite high while the more recent depositions, 184-233, are in the proper range and the low index value for sample 180 (on sapphire) is attributed to substrate surface roughness.

(d) Film Structure and Morphology

The thin film structure was determined from x-ray diffractometry. Typically, the only x-ray reflection observed was the β-SiC 111 reflection, indicating that the films had a strong texture. Accordingly, Read camera photographs were taken in a cylindrical camera using a 15° angle of incidence. From conventional diffractometry, peak heights were measured and used to compare the thin films to one another as shown in Table 6. The two films of particular interest are 178 and 233, both exhibiting very strong β-SiC 111 reflections. The angular spread of the 111 reflection can be measured on the Read patterns; i.e., the arc length is approximately equal to the angle between the 111 reflection and the thin film surface normal. In the Read photographs, other reflections were observed but they were very faint and Table 6 presents a summary of this analysis.

The latest deposition, #233, exhibits the highest degree of preferred orientation. For this sample, the primary processing differences were (a) high ion-gun cleaning voltage and (b) low power tin co-sputtering. More samples need to be generated under these conditions to confirm the importance of the tin additive.

For all depositions with a substrate $T > 700°C$ and the substrate surface had been ion-gun etched, a surface roughening problem appeared, primarily along the line of the heater. This roughening appears to the eye as a whitish area on the film. We plan to change heaters, from the quartz lamp type to a carbon-cloth type for the next few depositions in order to gain a better perspective on this phenomenon.

All of our samples are being analyzed by TEM for orientation and grain size and by SEM for a detailed look at the surface. The TEM selected area diffraction patterns (SADP's) will provide further evaluation of the crystalline perfection. To date, samples 177 and 184 have undergone TEM analysis and the SADP for the interfacial region of 177 reveals a high degree of crystallinity, although it has some curious features. A two-layer film is suggested by the overlap of the 001 and 112 type zone axes, the latter of which is twinned. The dark field image revealed small grains ∿100 Å diameter and larger grains ∿400 Å diameter. The 111 type zone axis was viewed for #184 and the spot pattern suggests less perfection than for #177.

(e) Sheet Resistivity

Of the seven thin films chosen for detailed study, only #180 is on sapphire so the sheet resistivity, ρ_s, could be measured with a four-point probe. For the thin films on silicon, the substrate is more conducting than the thin film so the electrical measurements are more ambiguous. For this section, <u>all</u> the single source films deposited on sapphire have been measured as have the six selected depositions on Si. There is a substantial difference in ρ_s depending on the substrate as expected. The values for SiC on Si are far too low to represent the SiC (typically $\sim 0.1\Omega$ cm for a 1μm film). This suggests that the region sampled included a significant depth into the silicon substrate. In contrast, for depositions on sapphire, ρ_s exhibits reasonable values. A listing of the ρ_s values for thin films on sapphire substrates is given in Table 8. The expected order of resistivity for an undoped film of about 1μm thickness should be $\sim 10^3\Omega$ cm.(4) Two of the thin films, #122 and #124, are close to this range. The lower ρ_s value for #125 reflects the Si deficiency of this film deposited at 200W.

(f) Conclusions and Future Steps

The SiC deposition process is continually improving. Subsequent depositions will place primary emphasis on the tin source parameters, on improved surface cleaning technique and higher substrate temperatures. In addition to continuing the TEM and starting the SEM work on the samples discussed in this report, optical transmission measurements are underway for the films on sapphire. Optical transmission may be possible for some of the films on Si by using a special sample preparation technique (similar to TEM sample preparation).

3. Synthesis of (Pd, Pt, Ir) Silicide Films

It is our intention to consider the important compounds in the quaternary system (Pd, Pt, Ir, Si) and fabricate high quality Schottky barriers of these selected silicides. Ultimately, using these special compounds, we propose to make multilayer structures with Si for IR detector applications. The key steps in the effort sequence are as follows:

(i) using multiple sources, determine the phase spreads for all the binaries Pd-Si, Pt-Si, Ir-Si and pseudo binaries (Pd,Pt)-Si, (Pd,Ir)-Si and (Pt,Ir)-Si,

(ii) development of single source deposition for special compounds in the set,

(iii) development of grain size control in films of these special compounds,

(iv) determination of Schottky barrier heights for these Si/(Pd,Pt,Ir)Si heterojunctions, and

(v) development of multilayer structures with the heterojunctions.

(a) (Pd, Pt) Silicide Film Synthesis

A literature survey has been conducted to gain structural, phase equilibrium and electrical characteristics information concerning these films.

The Pt_2Si infrared detector is a photoconductor with a high dark current. At the heterojunction between a silicide and silicon, the conduction band of Si bends up a distance ϕ where $\phi(Pt_2Si) = 0.27$ev and $\phi(Pd_2Si) = 0.72$ev. The absorbtion of infrared photons by the silicide at this junction causes changes in conductivity ($\lambda_c = 4.6\mu m$ for

Pt_2Si and λ_c = 1.7μm for Pd_2Si). Devices are usually made on 20-50Ω cm n-type (100) Si although electrical measurements are easier on 2-6Ω cm material and better interface definition and uniformity are possible on <111> Si. It is the extreme uniformity of large staring arrays that make these silicides useful as IR detectors. One would like to extend this capacity to lower barrier height heterojunctions to sample the 3-6μm and the 8-12μm ranges.

The literature shows that Pd_2Si has been grown epitaxially on Si and it may be possible to grow Si epitaxially on Pd_2Si. This is because the Si-Si spacing in the Pd_2Si basal plane is 3.75 Å which is close to the Si-Si spacing of 3.84 Å in the (111) plane of Si. The major compounds in the Pd-Si system are PdSi (orthorhombic), Pd_2Si (hexagonal), Pd_3Si (orthorhombic-cementite structure), Pd_4Si_2 (orthorhombic-metastable) and Pd_5Si which melts congruently. PdSi is not an equilibrium phase below 600°C and Pd_4Si is a common amorphous composition. Pd_2Si is not a line compound and there is some evidence that it has a hexagonal superlattice with cell dimensions 2a and 8c (similar to Fe_2P).

Although one may seek a heterojunction between Si and the different silicides to obtain a lower barrier height, other mechanisms of barrier height modification exist. Three examples of this are (1) ion bombardment to produce deep levels which lead to interface states and thus a recombination current → barrier lowering; (2) Pd_2Si growth into Si pushes impurities leading to a sharply peaked distribution at the interface → barrier lowering, and (3) composition variations → barrier lowering. Thus, the barrier height at the Pd_2Si/Si junction may be due to interface nonstoichiometry.

On the experimental side, both the Pd and Si sources have been characterized with respect to deposition rate versus source power and the dual source Pd-Si phase spread synthesis. Figure 16 illustrates the dual source sputtering configuration while Figs. 17 and 18 provide deposition rate data as a function of electrical characteristics for Si and Pd respectively. In Fig. 19, the dependence of relative Si deposition rate with Argon pressure and position is presented. Combining this data, the composition spread, and thus the phase spread, relative to distance from the Pd source is given in Fig. 20. The predicted position of occurrence of the Pd_2Si composition is also indicated in Fig. 20 (6 cm from the Pd source).

4. Electrical Diagnostics of SiO_x Films

(a) I-V and C-V Characteristics

The current vs voltage plots (I-V) have been made using a DC sweep voltage while the capacitance vs voltage plots (C-V) have been made with a DC bias sweep voltage plus a 1MHz, 10 mV signal. The procedures for these plots are extensively developed and well documented for SiO_2. The two important macroscopic electrical parameters obtained from these plots are the bulk resistivity, $\bar{\rho}$, from the I-V plot and the bulk permittivity, $\bar{\varepsilon}$, from the C-V plot. These standard tests have been made for the samples listed in Table 9 at a number of different locations on the sample (p-type substrates). Such measurements were made both before annealing (BA) and after annealing (AA) at 435°C for 25 minutes. The voltage range was ±20V and several I-V measurements were made per dot until consistent readings were recorded. This stable measurement endured in subsequent testing of the same dot. Table 9 gives a listing of the resistance and capacitance measurements in the BA and AA condition (here, N • R $\equiv$ not reliable and S • R $\equiv$ same range as the BA condition). For this type of diode, it is the negative part of the voltage sweep that leads to current flow (negative) in the forward bias direction vis-a-vis the p/n junction diode model. They may be visualized as being inverted through the origin for comparison purposes.

In Figs. 21a and 21b, we see the BA and AA for $X \simeq 2$ (in SiO_x) on dot #2. After annealing, only a small change is noted in the onset of the forward current but a very large change is seen in the reverse current which is the feature expected for short circuit conduction paths through the transition region (see Fig. 38d-theory). Figs. 22a, 22b, and 22c exhibit the BA results for other locations on the wafer and illustrate the same behavior as Fig. 21a (note the change in scale for Fig. 22b). This indicates electrical uniformity of the film and a junction that produces Igen = 86nA ± 10%. Annealing of the wafer led to a reverse current slope for dot #1 almost identical with that of Fig. 21b. In Figs. 23a and 23b, the C-V results on this sample for the BA and AA respectively are given. The BA result reveals what appears to be the normal junction capacitance plus two significant interface states, one appearing at $V \sim 0$ and the other at $V \sim -7$ volts. The AA result also reveals both of these features with the state at -7V increasing greatly in magnitude at the expense of the depletion layer capacitance.

At X = 1.5 for sample 81-083 ($SiO_{1.5}$), a similar behavior is exhibited except that there is a greater variance from dot to dot. Figs. 24a and 24b give the BA and AA respectively for dot #1 on this sample and we notice a significant change in the contact potential effect for this sample compared to that represented by Fig. 21. The point of transition to the forward current is significantly changed in the AA case compared to the BA case and is probably due to the short circuiting effect of the transition layer. For this sample, the variance in the key parameters, (i) slope of reverse characteristic, (ii) slope of forward characteristic, (iii) onset voltage for the forward characteristic, etc., has increase to ±35%. The C-V plots in the BA and AA condition for this dot are presented in Figs. 24c and 24d and, although these samples do not clearly reveal special interface states, other dots on this sample do reveal such states.

As X decreases further, the onset voltage for the transition to the forward characteristic increases further and the variance of the key characteristics, dot to dot on the same sample, increases. In fact, for $X \sim 0.8$, the dot to dot variance is greater than the average variance between two samples of different X.

(b) AC Conductance Characteristics

For reliable measurements, a finely adjustable probe was used to contact the Al dots on the oxide side while the Si side had a large area Al contact held to a vacuum chuck and the entire system was contained in a shielded metal box. Fig. 25 is the result for sample 81-084 (SiO with data analysis leading to C = 132pF and $\rho = 1.68 \times 10^8 \Omega$ cm for an estimated R of 280KΩ. The measurement indicated by * was made after turning off the vacuum chuck that held the sample to the contact base and the result shows the addition of a large series capacitance due to a poor contact to the base. Fig. 26, made with a 1 volt signal strength reveals the presence of two coupled circuits. The data can be described as the superposition of two semicircles; each with its center slightly below the abscissa. This indicates the existence of two parallel RC circuits connected in series with each circuit having frequency dependent parameters. Assuming frequency independent parameters (a reasonable first order approximation), we find C_1 = 79pF, R_1 = 50kΩ and $\rho_1 = 0.33 \times 10^8 \Omega$ cm plus C_2 = 252pF, R_2 = 300kΩ and $\rho_2 = 2.0 \times 10^8 \Omega$ cm.

In Figs. 27 and 28, the ρ and ε values for these films have been plotted versus X. We find a considerable difference between samples measured at a 50mV vs a 1000mV signal strength as expected if interface states are strongly involved in the measurement. We likewise find a significant difference between SiO_x samples made by cyclic layer deposition (moving substrate) vs simultaneous Si/O_2 deposition (fixed substrate).

B. THEORETICAL RESULTS

1. Review of the Electrical Characteristics of MIX and Heterojunction Diodes

It is our intention to gain special insights into the detailed structural features of bulk films, semiconducting, insulating and metallic, and into the electronic states at the interface between substrate and film by careful electrical characterization of the composite system. The main experimental techniques to be used are I-V and C-V characterization of the diode characteristics followed by AC conductance characterization. In many of the samples to be studied, a thin native oxide exists on top of the substrate prior to film deposition. In many cases, this has been removed by Argon-ion etching.

A useful analogy with which to begin discussion is the Si p/n junction diode. The next step toward reality is the heterojunction diode and the most complex case is the MIS diode. We shall proceed via these steps and follow the discussion of Sze.(5) In Fig. 29, the energy bands, Fermi energy, E_F, and electrostatic macropotential, V, is given for the isolated p-type and n-type material as well as for the junction where electron spill-over from n to p has produced a shift in the electrostatic potential so that the Fermi energies become aligned and the energy bands become shifted.

In Fig. 30a, the energy band diagram for two isolated pieces of semiconductor is given. The two semiconductors were assumed to have different band gaps, E_g, different permittivities, ε, different work functions, ϕ_n, and different electron affinities, χ. Work functions and electron affinity are defined as that energy required to remove an electron from the Fermi level, E_F, and from the bottom of the conduction band, E_c, to a position just outside the material (vacuum level). When an ideal abrupt heterojunction without interface traps is found between these semiconductors, the energy band profile at equilibrium is as shown in Fig. 30b for an n-p anisotype heterojunction. Since the Fermi level must coincide on both sides in equilibrium, the discontinuity in conduction band edges, ΔE_c, and valence band edges, ΔE_v, is invariant with doping in those cases where E_g and χ are not functions of doping (i.e., nondegenerate semiconductors).

The energy band diagram for an ideal MIS structure, for V = 0, is shown in Fig. 31b for a p-type semiconductor. An ideal MIS diode is defined as follows: (1) at zero applied bias there is no energy difference between the metal work function ϕ_n and the semiconductor work function (i.e., equal Fermi levels) so that a flat band condition obtains; (2) the only charges that can exist in the structure under any biasing conditions are those in the semiconductor and those with the equal but opposite sign on the metal surface adjacent to the insulator; and (3) there is no carrier transport through the insulator under DC biasing conditions or the resistivity of the insulator is infinity. When an ideal MIS diode is biased with negative or positive voltages, the three cases that may exist at a p-type semiconductor interface for increasing voltage are (a) accumulation, (b) depletion, and (c) inversion. In Fig. 31c the band diagram for the case of inversion is illustrated where the surface potential, ψ_s, is positive and larger than the midgap value, ψ_b (potential difference between the Fermi level and the intrinsic level of the bulk). The typical variation of the space-charge density per unit area of interface required to produce this potential, Q_s, as a function of the surface potential, ψ_s is shown in Fig. 32 for p-type silicon with $N_A = 4 \times 10^{15}$ cm^{-3} at room temperature.

The state of charge and electric field in the vicinity of the p/n junction and the heterojunction of Fig. 30 are illustrated in Fig. 33. The chief difference here, which has not been illustrated, is that the heterojunction may contain a population of charged interface states (traps). In case (a), we have that the negative of the contact potential is simply the area under the $\xi(x)$ vs x triangle leading to

$$V_o = -\frac{1}{2}\,\xi_o W = \frac{1}{2}\,\frac{q}{\varepsilon}\,N_D\,x_{n_o} W \tag{1}$$

$$= \frac{1}{2}\,\frac{q}{\varepsilon}\,\left(\frac{N_D N_A}{N_D + N_A}\right) W^2 \tag{2}$$

where

$$W = x_{p_o} + x_{n_o} = W\left(\frac{N_D}{N_D + N_A}\right) + W\left(\frac{N_A}{N_D + N_A}\right) \tag{3}$$

$$= \left[\frac{2\varepsilon kT}{q^2}\,\left(\ell n\,\frac{N_D N_A}{\eta_i^2}\right)\left(\frac{1}{N_A} + \frac{1}{N_D}\right)\right]^{\frac{1}{2}} \tag{4}$$

In case (b), the continuity of electric displacement applies at the interface ($\varepsilon_1 \xi_1 = \varepsilon_2 \xi_2$) and we obtain

$$X_1 = \left[\frac{2\,N_{A2}\varepsilon_1\varepsilon_2(V_{bi} - V)}{q\,N_{D1}(\varepsilon_1 N_{D1} + \varepsilon_2 N_{A2})}\right]^{\frac{1}{2}} \tag{5}$$

and

$$X_2 = \left[\frac{2\,N_{D1}\varepsilon_1\varepsilon_2(V_{bi} - V)}{q\,N_{A2}(\varepsilon_1 N_{D1} + \varepsilon_2 N_{A2})}\right]^{\frac{1}{2}} \tag{6}$$

The relative voltage supported in each semiconductor is

$$\frac{V_{b1} - V_1}{V_{b2} - V_2} = \frac{N_{A2}\varepsilon_2}{N_{D1}\varepsilon_1} \tag{7}$$

where $V = V_1 + V_2$. It is apparent that Eqs. 5-7 will reduce to the expressions for the p/n junction (homojunction) when both sides of the heterojunction have the same materials.

Figure 34a shows the band diagram of an ideal MIS structure. The charge distribution is shown in Fig. 34b. For charge neutrality of the system it is required that

$$Q_M = Q_n + qN_AW = Q_s \tag{8}$$

where Q_M is the charges per unit area on the metal, Q_n is the electrons per unit area in the inversion region, qN_AW is the ionized acceptors per unit area in the space charge region with space charge width W and Q_s is the total charges per unit area in the semiconductor. The electric field and potential, as obtained by first and second integrations of Poisson's equation, are shown in Figs. 34c and 34d respectively. In the absence of any work function differences, the applied voltage will appear partly across the insulator and partly across the semiconductors; i.e.,

$$V = V_i + \psi_s \tag{9}$$

where V_i is the potential across the insulator and is given by (see Fig. 34c)

$$V_i = \frac{Q_s d}{\varepsilon_i} = \frac{Q_s}{C_i} \qquad (10)$$

where C_i is the insulator capacitance.

Figure 35 shows the band diagram, the charge distributions, the electric field and the potential for an MIS diode with both surface states and insulator space charge. Comparing this figure with Fig. 34 for the ideal MIS diode we note that, for the same surface potential ψ_s, the applied voltage V is reduced indicating a voltage shift of the C-V curve toward negative voltage. The voltage shift, ΔV, due to the space charge density $\rho_i(x)$ is given by

$$\Delta V = \frac{-1}{C_i d} \int_{-d}^{o} x \; \rho_i(x) d_x \qquad (11)$$

(a) I-V Characteristics

If we now turn our attention to the steady-state conditions for both forward and reversed biased junctions we notice that, for the p/n junction case, the change in the contact potential difference and in the energy band picture is as given in Fig. 36. The transition width, W, decreases under forward bias and increases under reverse bias and the contact potential difference changes in the same way. This gives rise to the classical I-V characteristic for a p/n junction shown in Fig. 37

wherein the total current is given by

$$I = |I(\text{gen})|(e^{qV/kT} - 1) \quad . \tag{12}$$

In Eq. (12), the applied voltage V can be positive or negative, $V = V_f$ or $V = -V_r$. The current thus increases exponentially with forward bias. When V is negative, the exponential approaches zero and the current is given by $-|I(\text{gen})|$ which is in the n to p (negative) direction. This current is called the generation current or the reverse saturation current and is due to the resulting drift of minority carriers, produced by the thermal excitation of electron-hole pairs within a diffusion length of the junction, across the junction; i.e.,

$$-|I(\text{gen})| = -qA\left(\frac{D_p}{L_p} p_n + \frac{D_n}{L_n} n_p\right) \tag{13}$$

where A is the cross-sectional area of the junction, L_n and D_n are the diffusion length and diffusivity of electrons on the n-side of the junction while n is the minority carrier population on the p-side of the interface. The reverse breakdown current is ascribed to either (a) Zener breakdown due to carrier tunnelling across a heavily doped junction under reverse bias conditions, or (b) avalance breakdown due to impact ionization for lightly doped junctions.

In the foregoing, it was implicitly assumed that all of the applied bias voltage V appears across the transition region rather than in the neutral n and p regions. Of course, there will be some voltage drop in the neutral material if a current flows through it; however, for moderate to heavy doping the resistance of this neutral material is small and the IR drop can be neglected. For the MIS diode, on the other hand, this will not be true so that the current through the semiconductor/insulator junction must be given by

$$I = |I(\text{gen})| \, [\exp(q\{V-IR\}/kT) - 1] \qquad (14)$$

and the qualitative change in the I-V characteristic for this case is illustrated in Fig. 38a. We note a bending over of the current at a large forward bias as the characteristic associated with this effect. We should thus expect this behavior for thick oxides and high resistivity oxides.

In analyzing the p/n junction, it is generally assumed that recombination and thermal generation of carriers occur primarily in the neutral p and n regions, outside the transition region. In this model, forward current of the diode is carried by the recombination of excess minority carriers injected into each neutral region by the junction. Similarly, the reverse saturation current is due to the thermal generation of electron-hole pairs in the neutral regions and the subsequent diffusion of the generated minority carriers to the transition region, where they are swept to the other side by the field. In many cases this model is adequate; however, for the MIS diode junction a more complete description may be necessary which includes recombination and generation within the transition region itself.

This effect produces a negative slope to the reverse saturation current as illustrated in Fig. 38b.

Another important diode characteristic is noted in Fig. 38c for heavily doped p-n junction diodes having different band gaps. The I-V characteristics appear more square than exponential, the current being very small until a critical forward bias is reached and then the current increases rapidly. This occurs because of the difference between low-level and high-level carrier injection in a junction. When the injected excess carriers are negligible compared to the equilibrium majority carrier densities, the simple diode equation is valid. However, the resulting current may be very small particularly in heavily doped junctions and at low temperatures. As the injection level is increased to the point where the majority carrier densities deviate significantly from their equilibrium values, a more complete expression must be used; i.e.,

$$I = qA\{[\frac{e^{qV/kT}-1}{1 - e^{-2q(V_o-V)/kT}}][\frac{D_p p_n}{L_p}(1 + \frac{n_i^2}{p_p^2} e^{qV/kT}) + \frac{D_n n_p}{L_n}(1 + \frac{n_i^2}{n_n^2} e^{qV/kT})]\} \quad (15)$$

As the applied voltage approaches the contact potential, the current increases rapidly. The contact potential limits the forward bias which can be applied to the junction. In effect, the contact potential serves as a barrier to the net injection of excess carriers across a junction. If V_o is small, the diode current can be significant at fairly low voltage; however, if V_o is essentially the full band gap voltage, the current is negligible until the forward bias approaches E_g/q.

For an MIS diode of $Si/SiO_x/M$, as x is decreased from 2 in the SiO_x film, the film becomes more conducting, its Fermi energy increases, its contact potential difference w.r.t. the p-Si substrate increases and it contributes electrons to the substrate leading to a greatly increased V_o compared to that illustrated for the homojunction. As x decreases, we should expect to see the knee of the forward characteristics on the I-V plot move to larger values of V.

The effect of a graded rather than an abrupt p/n junction does not change the qualitative features of our conclusions. However, it will alter the quantitative conclusions. The effect of short circuit conduction paths through the transition region on the SiO_x side, on the other hand, will produce qualitative changes. In the forward direction, this should act like an additional current that is linearly proportional to the applied voltage and inversely proportional to the leakage resistance. In the reverse direction, this should act like a generation current that is linearly dependent on the applied voltage. Fig. 38d illustrates the qualitative type of behavior expected.

(b) C-V Characteristics

There are basically two types of capacitance associated with a junction: (1) the junction capacitance due to the dipole in the transition region and (2) the charge storage capacitance, or diffusion capacitance, arising from the lagging behind of the voltage as the current changes, due to charge storage effects. The junction capacitance is dominant under reverse bias conditions while the charge storage capacitance is largest when the junction is forward biased. For a p/n junction, the junction capacitance, C_j, is given by

$$C_j = \frac{\varepsilon A}{W} = \frac{A}{2}\left[\frac{2q\varepsilon}{(V_o - v)}\frac{N_D N_A}{N_D + N_A}\right]^{\frac{1}{2}} \tag{16}$$

where v is the AC voltage, eq. 4 has been used for W and the quasi steady state approximation has been used to obtain the excess carrier density associated with changes in v with time.

For forward bias, the charge storage capacitance, C_s, is calculated using a small signal AC analysis of the injected carrier distribution and one finds that

$$i_{AC} = G_s v_{AC} + C_s \frac{dv_{AC}}{dt} \tag{17a}$$

where

$$G_s = \frac{q}{kT} I_{DC} = \frac{q^2}{kT}\frac{AL_p}{\tau_p} p_n e^{qV_{DC}/kT} \tag{17b}$$

and

$$C_s = G_s \tau_p \tag{17c}$$

In eqs. 17, τ_p is the average lifetime of a hole in the n-type material. The factor G_s is an AC conductance. The charge storage capacitance can be a serious limitation for p/n junctions at high frequency. In Fig. 39a, the C-V plot for the p/n junction under reverse bias is essentially the capacitance associated with the depletion layer.

The capacitance for the heterojunction is given by

$$C_{het} = \left[\frac{qN_{D1}N_{A2}\varepsilon_1\varepsilon_2}{2(\varepsilon_1 N_{D1} + \varepsilon_2 N_{A2})(V_{bi} - V)}\right]^{\frac{1}{2}} \tag{18}$$

For the ideal MIS diode, the total capacitance, C, of the system is the series combination of the insulator capacitance, $C_i\,(=\varepsilon_i/d)$ and the semiconductor space-charge capacitance, C_D; i.e.,

$$C = \frac{C_i C_D}{C_i + C_D} \tag{19}$$

For a given insulator thickness, d, the value of C_i is constant and corresponds to the maximum capacitance of the system. The semiconductor capacitance, C_D, depends upon voltage according to the following equation

$$C_D = \frac{\partial Q_s}{\partial \psi_s} = \frac{\varepsilon_s}{L_D}\left[\frac{1 - e^{-\beta\psi_s} + \frac{n_{po}}{p_{po}}(e^{\beta\psi_s} - 1)}{F(\beta\psi_s, \frac{n_{po}}{p_{po}})}\right] \tag{20}$$

where

$$\beta = q/kT, \; L_D = (2\varepsilon_s/qp_{po}\beta)^{\frac{1}{2}}$$

and

$$F(\beta\psi, \frac{\eta_{po}}{p_{po}}) = [(e^{-\beta\psi} + \beta\psi - 1) + \frac{\eta_{po}}{p_{po}}(e^{\beta\psi} - \beta\psi - 1)]^{\frac{1}{2}} \gtrless 0 \qquad (21)$$

At the flat-band condition, $\psi_s = 0$ and C_D becomes

$$C_D(\text{flat-band}) = \sqrt{2}\; \varepsilon_s/L_D \qquad (22)$$

The complete description of C for the ideal MIS curve is given in Fig. 40 where the total capacitance at the flat-band condition is given, for p-type Si, by

$$C_{FB} = \varepsilon_i/[d + (\frac{\varepsilon_i}{\varepsilon_s})\sqrt{\frac{kT\varepsilon_s}{p_{po}\, q^2}}] \qquad (23)$$

On the left side of Fig. 40, we have an accumulation of holes and therefore a high differential capacitance of the semiconductor so that $C \rightarrow C_i$. The capacitance goes through a minimum in the depletion region and increases again as the inversion layer of electrons forms at the surface. The increase of that capacitance is dependent upon the ability of the electron concentration to follow the applied AC signal. This is only possible at low frequencies where the recombination-generation rates of minority carriers (here, electrons) can keep up with the small signal variation and lead to charge exchange in the inversion layer in step with the measurement signal. As a consequence, MIS curves measured to high frequencies do not show the increase of capacitance on the right side (Fig. 40b).

For the non-ideal MIS diode (Fig. 35), analysis of the space-charge region yields a shift, ΔV, in the silicon surface potential due to the different space charge densities, $\rho_i(x)$, in the insulator (see Eq. 11). The distance x in this formula is measured from the metal/oxide interface so it should be obvious that charges near the silicon interface will give rise to the largest voltage shift. When $\rho_i(x)$ is independent of the externally applied voltage, the effect of the localized charges on the MIS C-V curve is a parallel shift of the curve along the voltage axis by the amount illustrated in Fig. 39a. However, when a part of $\rho_i(x)$ is dependent on the applied voltage, as is the case for interface states, one has more difficulty because the interface state capacitance must be extracted from the measured capacitance.

When a voltage is applied, the interface levels will move up and down with the valence and conduction bands while the Fermi level remains fixed. A change of charge in the surface state occurs when it crosses the Fermi level. This change of charge will contribute to the MIS capacitance and alter the ideal MIS curve. The basic electrical equivalent circuit incorporating the surface state effect is shown in Fig. 41a. Here, C_s and R_s are the capacitance and resistance associated with the surface states and are functions of the surface potential, ψ_s. The product C_sR_s is defined as the interface state lifetime, τ, and determines the frequency behavior of the interface states. The parallel branch of the equivalent circuit of Fig. 41a can be converted into a frequency dependent capacitance C_p in parallel with a frequency dependent conductance G_p as shown in Fig. 41b where

$$C_p = C_D + \frac{C_s}{1 + \omega^2\tau^2} \tag{24}$$

and

$$\frac{G_p}{\omega} = \frac{C_s\,\omega\tau}{1 + \omega^2\tau^2} \quad . \tag{25}$$

Thus, the differentiation of the interface state capacitance from the measured capacitance as in Fig. 41a does not apply to the equivalent parallel conductance measurement because conductance arises solely from the steady-state loss due to the capture and emission of carriers by interface states and is thus a more direct measure of these properties. Both capacitance and equivalent parallel conductance, as functions of voltage and frequency, contain identical information about interface states. However, as Nicollian and Goetzberger(6) have shown, greater inaccuracies arise in extracting this information from a capacitance measurement. This is illustrated in Fig. 39b which shows both the measured capacitance and the equivalent parallel conduction cn p-type Si/SiO_2 having an $N_A \sim 2 \times 10^{16} cm^{-3}$ and an interface state density in the $10^{11} cm^{-2}$ - eV range and measured at δ-kH_z and 100 kH_z. The largest capacitance spread is 14% while the magnitude of the conductance peak is over one order of magnitude in this frequency range. We note that conductance measurements yield more accurate and reliable results particularly when the density of states is low as in the thermally oxidized Si system. In a system like Si/SiO$_x$, one expects the density of states to be quite large and there may be a number of important states to consider. Thus, one might expect bumps to appear in the C-V plots in certain voltage ranges for the Si/SiO$_x$ system.

Before closing this section, we should also note that the fixed oxide charge reported in the Si/SiO$_2$/M system causes a voltage shift, ΔV, via E. 11 due to the product $x\rho_i$ where $\rho_i > 0$. The identical effect would occur for a suitable dipole layer with the positive charge layer being closer to the Si since $x^+\rho^+ - x^-\rho^- > 0$ for this case. Thus, this same effect could be accounted for by a thin layer of altered dielectric constant at the interface (decreased). We thus see that C_i in Fig. 41 might perhaps be thought of as two capacitors in series. If the oxide also contains mobile ionic charges, then one of these capacitances at lease will exhibit a frequency dependence at low frequency.

(c) AC Conductance Characteristics

The most straightforward expressions of useful electrical quantities are as complex numbers in the frequency domain. A valuable technique for the representation of these quantities is to plot the real versus the imaginary parts of the quantity at various frequencies. The frequency dispersion of these values then produces geometric loci of points which are combinations of, or variations on, semicircles or vertical lines. These shapes allow for extrapolation to critical frequency ranges at which actual property values for particular network components can be obtained. As an example, consider Figs. 42a and 42b, where two simple networks are shown along with their corresponding plots of imaginary (X) versus real (R) impedance components.

Figures 42c and 42d illustrate the effect of adding one more parameter to the circuit. Note that, in Fig. 42c, the R_1-C_1 and R_1-C_2 relaxation times are sufficiently different that the semicircle and straight line are distinct. However, if C_1 and C_2 are similar (say within two orders of magnitude), the shapes will overlap. The analysis of Fig. 42d, then, consists of separating out contributions to the curve shape which corresponds to a particular relaxation time or R-C combination.

The complexity of any real system makes this a difficult problem which is compounded by the limitation of the experimentally available frequency range. Often not realized, however, is the considerable complementary information obtained by converting impedance values to those of other electrical quantities such as admittance and permittivity (complex dielectric constant). Since admittance is the reciprocal of impedance, a series R-C combination now plots as a semicircle in the complex plane while a parallel combination gives a straight line. The permittivity plot offers the additional advantage of extrapolating to values of dielectric constant on the abscissa. The simple relations between these quantities are

$$Z^* = \text{impedance} - R - jX \tag{26}$$

$$Y^* = \text{admittance} = G + jB \tag{27}$$

$$\varepsilon^* = \text{permittivity} = \varepsilon' - j\varepsilon'' \tag{28}$$

$$G = \text{conductance} = R/(R^2 + X^2) \tag{29}$$

$$B = \text{susceptance} = X/(R^2 + X^2) \tag{30}$$

$$\varepsilon' = \text{dielectric constant} = B/\omega\varepsilon_o \tag{31}$$

$$\varepsilon'' = \text{dielectric loss} = G/\omega\varepsilon_o \tag{32}$$

where R is resistance, X is reactance, ω is the radial frequency and ε_o is the permittivity of free space. It will also be seen that, over a given frequency range, one plot may prove much more valuable than another for the purposes of extrapolation.

If all the components of a real equivalent circuit were discrete frequency independent parameters, the analysis would be relatively straightforward. This, however, is never the case and considerable controversy has been generated over apparently frequency-dependent resistances and capacitances which cause complex plane circles to appear to be centered below the real axis and straight lines to be inclined from the vertical.

Warburg(7) first considered the electrical response of the interface between a metal electrode and a liquid electrolyte. He found that, at a single frequency, $X = R$ and that, over a limited frequency range $X, R \propto \omega^{-\frac{1}{2}}$. Although later work(8) showed this to be only approximately true, it is still generally accepted as Warburg's law that

$$R = A_1 \omega^{-\alpha_1} \quad ; \quad X = A_2 \omega^{-\alpha_2} \tag{33}$$

where α_1, $\alpha_2 \sim 0.5$ and $A_1 \sim A_2$. This type of behavior can be caused by Faradaic processes in which current crosses the interface by means of an electrochemical reaction. This is in contrast to a non-Faradaic process in which the charged particles do not cross the interface but instead charge and discharge the electrical double layer. Many other examples of Faradaic processes exist.(9) In any event, considering the frequency dependent aspects of the net capacitance in MIS diodes, we are well to consider the use of a diffusional admittance of the form

$$Y_z^* = A_1 \omega^{\alpha_1} + jA_2 \omega^{\alpha_2} \tag{34}$$

The foregoing plus the voltage sensitive circuit parameters of Fig. 41b make the data analysis a delicate issue. A system of measurement is needed wherein rapid representation of the three key complex plane plots and rapid discrimination of key circuit components from these plots can be obtained. One wishes to then rapidly subtract these known contributions from the data and then replot the remainder. One then iterates the previous step until all the circuit components are identified and quantitatively evaluated.

2. Film Formation Modeling via Computer Simulation

An important adjunct to the present experimental program is the use of a large high speed computer to simulate semiconductor or insulator film formation on a specific substrate. The rapidly increasing capacity of new computers makes them an ideal candidate to bridge the gap between atomic level considerations and macroscopic continuum (thermodynamic) level considerations of surfaces and interfaces. It allows us to explore the domain of experimental variable space for the film deposition process and identify potentially successful areas for experimentation. Through the Joint Stanford/NASA Ames Surface and Microstructure Institute, we have extraordinary access to such a computer.

The objective of this study is the analysis of surface and interface properties at microscopic levels and is designed to furnish all the available theoretical tools to combine with our experimental efforts in the best possible way. Two types of simulations have been initiated (1) parametric investigations and (2) specific case study. The parametric investigations are made for the purpose of analyzing the general behavior of different systems comparatively and to classify the important factors which influence both the structure and the energy-related properties of surfaces and interfaces for these systems. In this type of study, a molecular dynamics technique based upon Lennard-Jones type pair interactions is used to investigate time-dependent as well as equilibrium properties. The specific case study deals with systems containing Si and O atoms. In this case a more involved potential energy function (PEF) is employed and the system is simulated via a Monte-Carlo procedure. This furnishes the equilibrium properties of the system at its interfaces and surfaces as well as in the bulk.

(a) Parametric Investigation

The following progress has been made during this first six-month period:

(1) A molecular dynamics program (MOLDY) based on the Nordsieck-gear algorthim has been prepared. The program is able to deal with the bulk as well as with the surface and interface regions for systems containing up to three different atomic species.

(2) A utility package has been prepared for the evaluation of the MOLDY results. This package consists of several programs and uses the data generated by MOLDY as an input. It has the following capabilities:

  (i) The radial distribution function, virial, density and energy profiles across the interface can be obtained.

(ii) It can perform time series analysis: correlation functions (density or velocity auto-correlation) and vibrational frequency spectra of the particles in motion can be calculated. The program has the flexibility of calculating components of a vibrational frequency spectrum for any number of particles and for any desired subsection of the system. It uses a fast fourier transformation routine and accepts velocity components of the particles generated by MOLDY. The program requires relatively small amount of CPU time.

(3) A graphic software package has also been developed which provides visual inspection of the whole system as well as of any local region of the system. It can be employed for generating a single frame for any desired time step or it can be used to produce a movie for the real time simulation of individual atomic motions.

The package also includes a program which can be used to generate trajectories of individual particles for quick inspection.

At the moment a test case is under investigation for the analysis. The system consists of two different atomic species to represent an interface between a substrate and an adlayer. Figure 43 demonstrates the system schematically. It contains 927 particles (with 381 particles (Cu) in the adlayer and the rest, 546 particles (Ag), in the substrate). The reduced parameters used in the molecular dynamics procedure (representative of a Cu/Ag system) were:

$\varepsilon^*_{ad} = 1.1872$ $\sigma^*_{ad} = 0.8846$

$\varepsilon^*_{sub} = 1.0$ $\sigma^*_{sub} = 1.$

Time step, $dt^* = 0.01$

Temperature, $T^* = 0.3$

No periodic boundary condition has been imposed because of the binary nature of the system. The particles (Ag) within the three bottom layers of the substrate were held fixed during the run; but, they were permitted to interact with the rest of the system contributing to the total potential energy. The test system was run up to 1000 time steps. The first 200 steps were used for the temperature rescaling process, and the rest employed in the analysis. All the thermodynamic quantities were calculated considering only the "core" region of the hexagonal slab (to eliminate the surface effect). The core included all the atoms within a radius of 2.8 σ^*_{sub} from the center. Figure 44 demonstrates mobile atoms during the equilibration; and Figure 45 is a close-up view of the same region around the interface. Figure 46 shows trajectories of the atoms within the top layer of the substrate, and Fig. 47 is a trajectory plot for the bottom layer of the adsorbate (which is facing the layer in Fig. 46).

Figure 48 demonstrates the potential energy profile across the interface which is located between the third and the fourth peaks. The difference between these peaks indicates the stronger binding among the adatoms. Figure 49 is the virial profile similar to Fig. 48. Because of its differential character, the virial reflects the mismatch of the sites at the interface. The difference in atomic sizes causes the adlayer side to dilate while the substrate side contracts. The dilation is exhibited by a negative virial while the contraction by an added positive contribution as expected.

(b) Simulation of Systems with Si and O Atoms

For a more quantitative representation of systems involving Si and O atoms we considered a general type of potential energy function which is based on two-body and three-body interactions. The most serious difficulty involved in simulation studies of such systems is, in general, due to the potential energy function and its ability to represent the system adequately. The analytical form of the potential energy function and the evaluation of its parameters that are being used are described briefly.

For a system of N particles the total potential energy Φ may be expressed as:

$$\phi = \frac{1}{2!} \sum_{i \neq j}^{N} \sum^{N} u(\vec{r}_i, \vec{r}_j) + \frac{1}{3!} \sum_{i \neq j \neq k}^{N} \sum^{N} \sum^{N} u(\vec{r}_i, \vec{r}_j, \vec{r}_k) + \ldots$$

$$\ldots + \frac{1}{n!} \underset{i \neq j \neq \ldots \neq n}{\sum_{i}^{N} \sum_{j}^{N} \ldots \sum_{n}^{N}} u(\vec{r}_i, \vec{r}_j, \ldots, \vec{r}_n) + \ldots \qquad (35)$$

where, $u(\vec{r}_i, \vec{r}_j)$, $u(\vec{r}_i, \vec{r}_j, \vec{r}_k)$, ..., $u(\vec{r}_i, \vec{r}_j, ..., \vec{r}_n)$ are the two-, three- and n-body potentials respectively; $\vec{r}_j$ denotes the position of the j^{th} particle. Clearly, the most important term in this expansion is the first term involving the two-body potential. Therefore, in the majority of the atomistic calculations to date only pairwise additive potentials have been used. In this investigation not only two-body but also three-body interactions are taken into consideration. Because this expression (Eq. 35) will be used in lengthy machine computations, the functional form of $u(\vec{r}_i, \vec{r}_j)$ and $u(\vec{r}_i, \vec{r}_j, \vec{r}_k)$ must be very simple. The two-body part, therefore, is represented by a Mie-type potential.

$$u(r_{ij}) = \frac{\varepsilon}{m-n} [n(\frac{r_o}{r_{ij}})^m - m(\frac{r_o}{r_{ij}})^n] \qquad (36)$$

with $r_{ij} = |\vec{r}_i - \vec{r}_j|$, while r^o denotes the equilibrium separation and ε is the energy at $r_{ij} = r^o$. The exponents m and n account for the repulsive and attractive terms, respectively. For the intermediate to large separations the three-body interactions may be expressed as:

$$u(\vec{r}_i, \vec{r}_j, \vec{r}_k) = \sum_{\ell} Z_\ell \cdot G_\ell(\vec{r}_i, \vec{r}_j, \vec{r}_k) \qquad (37)$$

where, the summation includes all triple multiple interactions resulting from the expansion of the third-order interaction energy for three atoms. Each term in the summation is expressed as the product of a geometrical factor $G(\vec{r}_i, \vec{r}_j, \vec{r}_k)$ which depends on the relative positions of the three atomic nuclei and an interaction constant which depends only on the atomic species involved in the interaction. Here, we employ only the triple-dipole interaction which has been shown to be the dominant contribution:

$$u(\vec{r}_i, \vec{r}_j, \vec{r}_k) = Z_1 \cdot G_1(\vec{r}_i, \vec{r}_j, \vec{r}_k) \tag{38}$$

with

$$G(\vec{r}_i, \vec{r}_j, \vec{r}_k) = \frac{1 + 3\mathrm{Cos}\ \theta_i \mathrm{Cos}\ \theta_j \mathrm{Cos}\ \theta_k}{(r_{in} \cdot r_{ik} \cdot r_{jk})^3} \tag{39}$$

where, θ_i, θ_j, θ_k and r_{ij}, r_{ik}, r_{jk} represent the angles and the sides of the triangle formed by the three particles i, j and k.

Now, combining equations 35 through 39, and neglecting the four-body and higher terms one obtains:

$$\Phi = \Psi_2 + \Psi_3 \tag{40a}$$

with

$$\Psi_2 = \frac{1}{2} \sum_{\substack{i \\ i \neq j}}^{N} \sum_{j}^{N} \frac{\varepsilon}{m-n} \left[n\left(\frac{r^o}{r_{ij}}\right)^m - m\left(\frac{r^o}{r_{ij}}\right)^n\right] \tag{40b}$$

and

$$\Psi_3 = \frac{1}{6} \sum_{i}^{N} \sum_{\substack{j \\ k \neq j \neq k}}^{N} \sum_{k}^{N} Z_1 \frac{(1 + 3\mathrm{Cos}\theta_i\ \mathrm{Cos}\theta_j\ \mathrm{Cos}\theta_k)}{(r_{ij} \cdot r_{ik} \cdot r_{jk})^3} \tag{40c}$$

In this general form the total potential energy Φ is a function of the parameters, ε, r^o, m, n and Z_1, and the atomic configuration of the system. The parameters are assumed to be independent of the atomic positions and the geometry of the system. They depend only on the atomic properties of species involved.

For a binary system of types 1 and 2 [1 ≡ silicon, and 2 ≡ oxygen] with the corresponding number of particles N_1 and N_2, equation 6 may be rewritten as:

$$\Phi = \Psi_2 + \Psi_3 \tag{41}$$

with,

$$\Psi_2 = \sum_{\alpha}^{2} \sum_{\beta}^{2} \frac{N_\alpha \, \varepsilon_{\alpha\beta}}{2(m-n)} [n \; a_{\alpha\beta}^{(m)} \; R_{\alpha\beta}^{m} - m a_{\alpha\beta}^{(n)} \; R_{\alpha\beta}^{n}] \tag{42}$$

and

$$\Psi_3 = \sum_{\alpha}^{2} \sum_{\substack{\beta \\ \beta \leq \gamma}}^{2} \sum_{\gamma}^{2} \frac{N_\alpha \, Z_{\alpha\beta\gamma}}{3d^9} \cdot T_{\alpha\beta\gamma} \tag{43}$$

$\alpha = 1,2$
$\beta = 1,2$
$\gamma = 1,2$

where,

$$R_{\alpha\beta} = \frac{r^{o}_{\alpha\beta}}{d} \qquad (44)$$

$$a^{(m)}_{\alpha\beta} = \sum_{j}^{N_\beta} \left(\frac{d}{r_{\alpha j}}\right)^m \qquad r_{\alpha j} \neq 0 \ . \qquad (45)$$

$$a^{(n)}_{\alpha\beta} = \sum_{j}^{N_\beta} \left(\frac{d}{r_{\alpha j}}\right)^n \qquad r_{\alpha j} \neq 0 \ . \qquad (46)$$

and

$$T_{\alpha\beta\gamma} = \sum_{\substack{j \\ j<k}}^{N_\beta} \sum_{k}^{N_\gamma} G(r_{\alpha j}, r_{\alpha k}, r_{jk}) \left\{ \begin{array}{l} r_{\alpha i} \neq 0 \\ r_{\alpha j} \neq 0 \end{array} \right. \qquad (47)$$

$r^{o}_{\alpha\beta}$ represents the equilibrium separation between the two species α and β for the two-body part ($r^{o}_{\alpha\beta} \equiv r^{o}_{\beta\alpha}$); "d" is a critical distance parameter which is used as a normalizing factor. Φ is independent of the value of d. $r_{\alpha j} = |\vec{r}_\alpha - \vec{r}_j|$, where $\vec{r}_\alpha$ denotes the position of an atom of type α taken as the central particle for the summation. The total number of particles in the system is given by $N_{Tot} = N_1 + N_2$.

The parameters (such as $\varepsilon_{\alpha\beta}$, $r^{o}_{\alpha\beta}$, $a_{\alpha\beta}$, $Z_{\alpha\beta\gamma}$ and $T_{\alpha\beta\gamma}$) were obtained using isolated microclusters and the bulk property data for pure Si and O, as well as data for SiO_2 forms. Furthermore, for the evaluation of the parameters, the stability criterion was considered that is given as:

$$\left(\frac{\partial \Phi}{\partial V}\right)_{T_o} = 0 \quad . \tag{48}$$

For a start, exponents m and n in the two-body term were assumed to be equal to 12 and 6, respectively. Values for $a_{\alpha\beta}^{(m)}$, $a_{\alpha\beta}^{(n)}$ amd $T_{\alpha\beta\gamma}$ are computed directly from the crystallographic data for the corresponding SiO_2 forms (see Table 10). The parameters ($\varepsilon_{\alpha\beta}$, $r_{\alpha\beta}^{o}$ and $Z_{\alpha\beta\gamma}$) for silicon were calculated from experimental bulk and small cluster data, and for oxygen they were obtained from thermodynamic data reported for the O_2 molecule as:

$$\varepsilon_{11} = 37745 \ (^{o}K)$$

$$r_{11}^{o} = 2.3516 \ (\text{Å})$$

$$Z_{111} = 6.136 \times 10^{6} (^{o}K \cdot \text{Å}^{9})$$

$$\varepsilon_{22} = 59943 \ (^{o}K)$$

$$r_{22}^{o} = 1.2078 \ (\text{Å})$$

$$Z_{222} = \sim 0.2623 \times 10^{6} (^{o}K \cdot \text{Å}^{9})^{(*)}$$

---

[*] This value is only an approximation at this stage. However, (if needed) it may be perfected using bulk SiO_2 data.

Next, we used thermodynamic data (namely cohesive energies) for α-quartz and α-cristabolite. Employing equations 6 and 14, the rest of the potential energy parameters were calculated as:

$$\varepsilon_{12} = 42531.7\ (^{o}K)$$

$$r^{o}_{12} = 1.6259\ (\mathring{A})$$

$$Z_{112} = 5.0086 \times 10^{6}\ (^{o}K * \mathring{A}^{9})$$

$$Z_{122} = 3.9999 \times 10^{6}\ (^{o}K * \mathring{A}^{9})$$

This set of parameters, furthermore, used in equation 40 and the cohesive energies for the β-cristabolite and β-quartz were calculated. Results are found to be in good agreement with the experiments. Calculated energies were:

$$\phi_{(\beta\text{-cristabalite})} = -414.9\ (\text{kcal/mole})$$

$$\phi_{(\beta\text{-quartz})} = -406.5\ (\text{kcal/mole})$$

experimental cohesive energies were tabulated in Table 10.

For further investigation of SiO_2 systems, the following programs are under preparation.

(1) Monte-Carlo Program: This program is written to handle systems containing up to three different atomic species. It uses equation 40 and generates appropriate Markov chain configurations of the system in a very efficient way. It stores the list of neighbors using the "large core memory" (in a CDC 7600) that reduces the computation time considerably, in particular, for larger systems. This program is now in its debugging stage.

(2) A Software Package for Structural Characteristics of SiO_2 Systems:

This package contains basically two different programs. The first is to calculate the radial distribution function of the system. It provides the radial distribution function associated with any portion of the system; and it is able to calculate partial (i.e., $g^{(R)}_{(Si-Si)}$, $g^{(R)}_{(Si-O)}$ or $g^{(R)}_{(O-O)}$) or the total g(R) of any SiO_2 system. The second program is to calculate angular distributions for the whole system or for any subsection of the system. In particular, it is designed to calculate the distributions for angles such as ((Si - O - Si) and (O - Si - O) between the neighboring atoms.

References

(1) W. A. Tiller, "Fabrication and Properties of Multilayer Structures," Fourth Semiannual Technical Report for Period March 1, 1981-August 31, 1981, ARPA.

(2) W. A. Tiller and T. W. Barbee, Jr., "Fabrication and Properties of Multilayer Structures," Third Semiannual Technical Report for Period September 1, 1980-February 28, 1981, ARPA.

(3) Handbook of Physics and Chemistry, Chemical Rubber Co., Cleveland, Ohio 197

(4) Silicon Carbide, Eds. R. C. Marshall, J. W. Faust, Jr., and C. E. Ryan (U.S. Carolina Press, Columbia, N.Y.) 1974.

(5) S. M. Sze, Physics of Semiconductor Devices (John Wiley & Sons, N.Y.), 1981.

(6) E. H. Nicollian and A. Goetzberger, Bell Syst. Tech. J. 46. 1055 (1967).

(7) E. Warburg, Annalen der Physik und Chemie 67. 493 (1899).

(8) H. Fricke, Physics, 1. 106 (1931).

(9) D. C. Grahame, J. Electrochem Soc. 99, 370 (1952).

Table 1

Ion Gun Etch Parameters

Ion Gun to Substrate Distance (inches)	Operating Voltage (kV)	Chamber Pressure (μm Ar)	Etching Time (min.)	Thickness Change (Å)	Etch Rate (Å/min.)
3	2.0	4	9	120	15.6
3	2.0	4	30	650	21.7
3	2.0	8	15	320	18.9
3	2.0	8	30	575	18.7
4	0.75	4	30	none	-
4	0.75	8	40	none	-
4	2.0	4	20	245	12.25
4	2.0	4	40	650	16.2
4	2.0	8	20	270	13.5
4	2.0	8	40	580	14.5
5	0.75	4	20	none	-
5	0.75	4	30	none	-
5	0.75	4	40	none	-
5	0.75	8	20	none	-
5	0.75	8	40	none	-
5	2.0	7.5	15	none	-
5	2.0	7.5	20	none	-
5	2.0	7.25	40	130	3.25

Note: (1) All substrates were ∿1μm thermal oxide on Silicon.

(2) Operating current was 2 mA in all cases.

Table 2

Temperature Dependence of Oxide Depositions

substrates: (111)Si
source: 3" Si
distance: 4"
ion etch: 750V, 2 mA, 40 min.
deposition power: 500 W (rf)
time: 20 min.
oxygen pressure: 0.30 ± 0.015 μm
Argon pressure: 4.0 μm

Run Number	Temperature (°C)	Thickness (Å)	Refractive Index	O/Si (At %)
81-215	25	7000	1.47	65.6/34.4
81-219	25	7300	1.46	66.6/33.4
81-216	240	6550	1.50	63.4/36.6
81-217	340	4650	1.46	60.1/39.9
81-218	500	3500	1.53	55.4/44.6
81-220	660	(2500)	(1.45)	57.6/42.4
81-221	660	4500	1.45	47.0/53.0

Table 3

Cyclic Formation of SiO_x Layers

Sample Number	Si Deposition Rate (Å / sec)	Rotation Period (sec)	Si Layer Thickness (Å)	Number of Layers	Exposure (torr sec)	Gross Composition Si/O (At %)
81-083	2.05	0.52	1.1	3461	1.1×10^{-4}	45:55
81-084	2.05	5.2	10.7	156	1.5×10^{-3}	49.5:50.5
81-085	2.05	10.2	20.9	176.5	2.5×10^{-3}	57:43

Table 4

Single Source Depositions

Film Number	Substrate	Process: SiC target power, T, source-substrate distance, ion gun voltage, P, Sn target power.
122	Al_2O_3	600W, 25°C, 3"
124	Al_2O_3	600W, 700°C, 3"
125	Al_2O_3	200W, 820°C, 3"
* 177	(100)Si	600W, 720°C, 3", 750V, 8μ
* 178	(111)Si	600W, 700°C, 3", 750V, 8μ
* 180	Al_2O_3	600W, 660°C, 4", 750V, 8μ
* 184	(111)Si	200W, 700°C, 4", 750V, 8μ
210	(100)Si	600W, 25°C, 4", 750V, 8μ
211	(100)Si	600W, 615°C, 4", 750V, 8μ
212	(100)Si	600W, 715°C, 4", 750V, 8μ
222	(111)Si	600W, 25°C, 5", 750V, 8μ
223	(111)Si	600W, 750°C, 5", 750V, 8μ
224	(111)Si	600W, 700°C, 5", 750V, 8μ
225	(111)Si	600W, 615°C, 5", 750V, 8μ
* 228	(111)Si	600W, 750°C, 5", 2000V, 4μ
229	(111)Si	600W, 750°C, 5", 1000V, 4μ, 145W
* 231	(111)Si	600W, 750°C, 5", 1000V, 4μ, 18W
* 233	(111)Si	600W, 750°C, 5", 4000V, 4μ, 16W

Table 5

Refractive Index Measurements of Selected SiC Thin Films

Sample Number	Substrate	Refractive Index	Stoichiometry Si : C
177	(100)Si	3.03	52:48
178	(111)Si	3.21	52:48
180	ribbon Al_2O_3	2.34	51:49
184	(111)Si	2.71	45:55
228	(111)Si	2.76	53:47
231	(111)Si	2.54	47:53
233	(111)Si	2.73	48:52

Table 6

Representative SiC Depositions and Relative X-ray Peak Heights

Film Number	Substrate	Process
177	(100)Si	600W, 720°C, 3", 750V, 8µ
178	(111)Si	600W, 700°C, 3", 750V, 8µ
180	Al_2O_3	600W, 660°C, 4", 750V, 8µ
184	(111)Si	200W, 700°C, 4", 750V, 8µ
228	(111)Si	600W, 700°C, 5", 2kV, 4µ
231	(111)Si	600W, 750°C, 5", 1kV, 4µ, 18W
233	(111)Si	600W, 750°C, 5", 4kV, 4µ, 18W

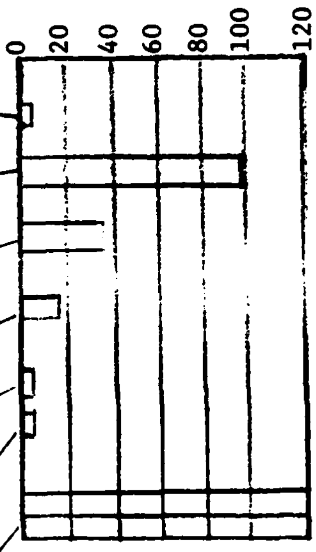

Table 7

Read Camera Analysis

Sample Number	β-SiC reflections present 111	220	311	200	arc length of 111 ∿ deviation from surface normal
177	x		x	x	±30°
178	x	x	x		±25°
180	x				+20°, -35°
184	x				±30°
228	x	x	x		±25°
231	x				±90°
233	x				±5°

Table 8

Sheet Resistivity of SiC Thin Films Measured with a 4-Point Probe

Sample	Substrate	Deposition Temperature °C	SiC Target Power	Film Thickness µm	Sheet Resistivity Ω cm	Si:C Film Composition
122	$1\bar{1}02$ Al_2O_3	25	600W	0.85	265	51:49
124	$1\bar{1}02$ Al_2O_3	700	600W	0.52	320-590	50:50
125	$1\bar{1}02$ Al_2O_3	820	200W	0.55	6-24	46:54
180	ribbon Al_2O_3	660	600W	1.40	260	51:49

Table 9

SiO$_x$ Measurements

Sample	X	Thickness (Å)	Dot		Resistance (Ω)				Capacitance (pF)			
			Number	Diameter (mm)	BA		AA		BA		AA	
					V < 0	V < 0	V < 0	V < 0	V < 0	V < 0	V < 0	V < 0
81-079	2			1.3	500	10^8	500	1.5×10^4	10	220	.15	N.R.
81-083	1.5	1300		1.5-1.8	10^3	10^4-10^5	10^4	10^4	50	100	S.R.	S.R.
81-084	1.2	1360		1.0	2×10^3	10^5	2×10^4		20	70	S.R.	S.R.
81-085	0.8	4450		1.0	10^3-10^4	10^5-10^8	$\sim10^4$	$\sim10^4$	10-20	75	S.R.	S.R.
80-191	0.1	5000		1.0	10^3	10^8	$< 10^3$	10^4	25	100		

Table 10

	α-Crist.	α-quartz	β-Crist.	β-quartz
R(Si-Si)	3.0767	3.0579	3.0880	3.0982
R(Si-O)	1.60	1.60	1.55	1.63
R(O-O)	2.60	2.63	2.53	2.60
a^m_{11}	4.0575	4.1148	4.0388	4.1048
a^m_{12}	9722.33	8328.37	9796.98	9870.78
a^m_{22}	41.3494	36.7629	42.0266	48.1561
a^m_{21}	4861.17	4164.88	4898.46	4929.74
a^n_{11}	5.2401	5.6759	5.0999	5.6325
a^n_{12}	202.442	188.962	202.892	204.702
a^n_{22}	19.5795	20.2410	19.3041	21.5124
a^n_{21}	101.221	94.4946	101.444	102.302
T_{111}	5.7840	8.3242	4.94088	8.0688
T_{112}	-191.313	-117.663	-202.276	-175.685
T_{122}	174.512	195.381	167.158	195.231
T_{222}	62.0504	76.5891	57.5318	73.9876
T_{221}	174.555	195.427	167.131	195.237
T_{211}	-47.8405	-29.4278	-50.5788	-43.9041
Cohesive Energy (kcal/mole)	-412.14	-412.540	-417.43	-417.85

Figure Captions

1. (a) Arrangement of deposition source, Ar-cleaner, oxygen supply ring and substrate heater used in the reactive sputtering of SiO_x films.

   (b) Expanded view of the quartz ring for supplying O_2 to the rectangular substrate surface.

2. Ion-gun etching profile for the following conditions:

Run	Power	Distance	Chamber Pressure	Etch Time	Etch Rate
---	2kV, 2mA	3 in	8 μm(ar)	30 min	18.7 Å/min
— .	2kV, 2mA	3 "	8 " "	15 "	18.9 "
— ..	2kV, 2mA	3 "	4 " "	30 "	21.7 "
———	2kV, 2mA	3"	4 " "	9 "	15.6 "

3. Index of refraction profile for the same conditions as in Fig. 2.
4. Configuration of reactive sputtering deposition mask.
5. SiO_2 thickness vs. deposition temperature.
6. Topographic map of deposit thickness via ellipsometry for samples 82-030 and 82-031.
7. Infrared transmission spectra for typical amorphous SiO_2.
8. IR Transmission spectra for amorphous SiO_2 at several deposition temperatures illustrating the wavenumber shift.
9. Thickness profiles, determined by the Tally-step method, for SiO_x formed via the cyclic deposition/reaction technique.
10. Index of refraction profiles, determined ellipsometrically, for SiO_x formed via the cyclic deposition/reaction technique.

11. Plot of ZnO_x stoichiometry profile over the substrate for the simultaneous deposition/reaction technique.
12. Plot of index of refraction variation for the sample in Fig. 11.
13. Single-source SiC sputtering system with ion gun for substrate surface cleaning and with portable tin source in a likely position.
14. Stoichiometry of selected thin films as measured by electron microprobe.
15. Figure withdrawn from report.
16. Dual source sputtering configuration used in these studies.
17. Silicon deposition rate as a function of R.F. power.
18. Palladium deposition rate as a function of current of the D.C. power source.
19. Film deposition characteristics for Si for various argon pressures.
20. Relative Pd/Si deposition rate as a function of distance from the Pd source.
21. I-V plots for SiO_x samples both before annealing (BA) and after annealing (AA).
22. I-V plots (BA) for SiO_x at different locations on the same sample.
23. C-V plots for SiO_x both BA and AA at one location.
24. I-V and C-V plots for SiO_x at one location (BA and AA).
25. A-C conductance plots (reactance vs. resistance) for SiO_x (BA) at an oscillator amplitude of 50 mV.
26. A-C conductance plot for SiO_x at an oscillator amplitude of IV.
27. SiO_x resistivity as a function of stoichiometry (BA) for both the fixed substrate (simultaneous deposition) and the moving substrate (sequential deposition) cases.

28. SiO_x deliectric constant (BA) for the fixed substrate (F.S.) and moving substrate (M.S.) cases.

29. Properties of an equilibrium p-n junction: (a) isolated, neutral regions of p-type and n-type material and energy bands for the isolated regions; (b) junction, showing space charge in the transition region W, the resulting electric field $\mathcal{E}$ and contact potential V_o, and the separation of the energy bands; (c) directions of the four components of particle flow within the transition regions and the resulting current directions.

30. (a) Energy-band diagram for two isolated semiconductors in which space-charge neutrality is assumed to exist in each region.

    (b) Energy-band diagram of an ideal n-p anisotype heterojunction at thermal equilibrium.

31. (a) Metal-insulator-semiconductor (MIS) diode.

    (b) Energy-based diagram of ideal MIS diode at $V = 0$ for a p-type semiconductor.

    (c) Energy-band diagram of ideal MIS diode at $V > 0$.

32. Variation of space-charge density in the semiconductor as a function of the surface potential ψ_s for p-type silicon with $N_A = 4 \times 10^{15}$ cm^{-3} at room temperature; ψ_B is the potential difference between the Fermi level and the intrinsic level of the bulk semiconductor.

33. (a) Space charge and electric field distribution within the transition region of a p/n junction with $N_d > N_a$: top, the transition region with $x = 0$ defined at the metallurgical junction; middle, charge density within the transitional region, neglecting the free carriers; bottom, the electric field distribution, where the reference direction for $\mathcal{E}$ is arbitrarily taken as the +x direction.

(b) The same for Si/SiO$_x$ heterojunction.

34. (a) Band diagram of an ideal MIS diode

(b) Charge distribution under inversion condition

(c) Electric field distribution

(d) Potential distribution.

35. An MIS diode with fixed oxide charge and oxide trapped charge.

(a) Band diagram

(b) Charge distribution

(c) Field

(d) Potential.

36. Effects of bias at a p-n junction; transition region width and electric field, electrostatic potential, energy band diagram, and particle flow and current directions within W for (a) equilibrium, (b) forward bias and (c) reverse bias.

37. I-V characteristic of a p/n junction.

38. Various non-ideal p/n junction diode effects.

39. (a) Ideal p/n junction C-V plot plus real Si/SiO$_2$ heterojunction C-V plot illustrating the flat band shift, ΔV, due to the charge effects at the non-ideal junction.

(b) Capacitance and equivalent parallel conductance measurement at 5 kHz and 100 kHz on a p-type sample having an acceptor density of 2.08 x 10^{16} cm^{-3} and interface state density in the 10^{11} cm^{-2} -eV^{-1} range.

40. MIS capacitance-voltage curves: (a) low frequency, (b) high frequency, (c) deep depletion.

41. (a) Electrical equivalent circuit of the MIS incorporating the surface state effect (C$_S$ and R$_S$ are capacitance and resistance associated

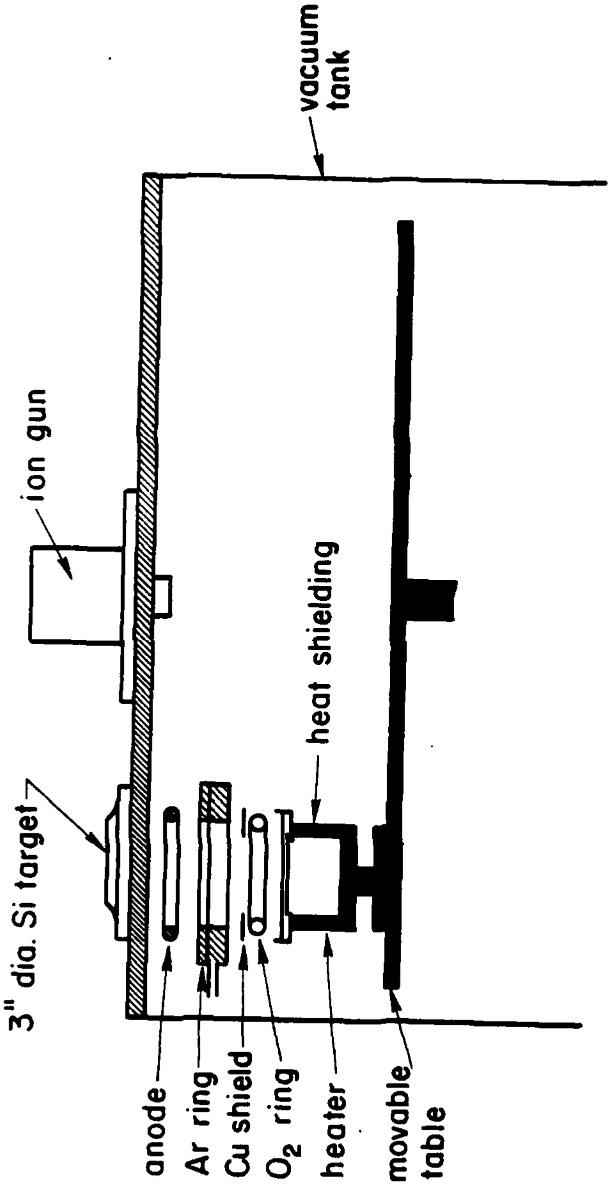
vacuum tank
ion gun
heat shielding
3" dia. Si target
anode
Ar ring
Cu shield
O_2 ring
heater
movable table

FIGURE 1(a)

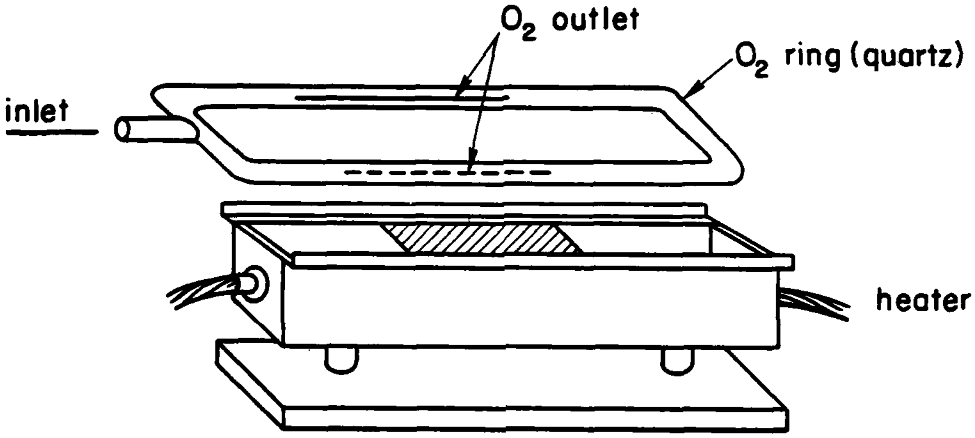

FIGURE 1(b)

ION GUN ETCH PROFILE
(INDEX OF REFRACTION- n_f)

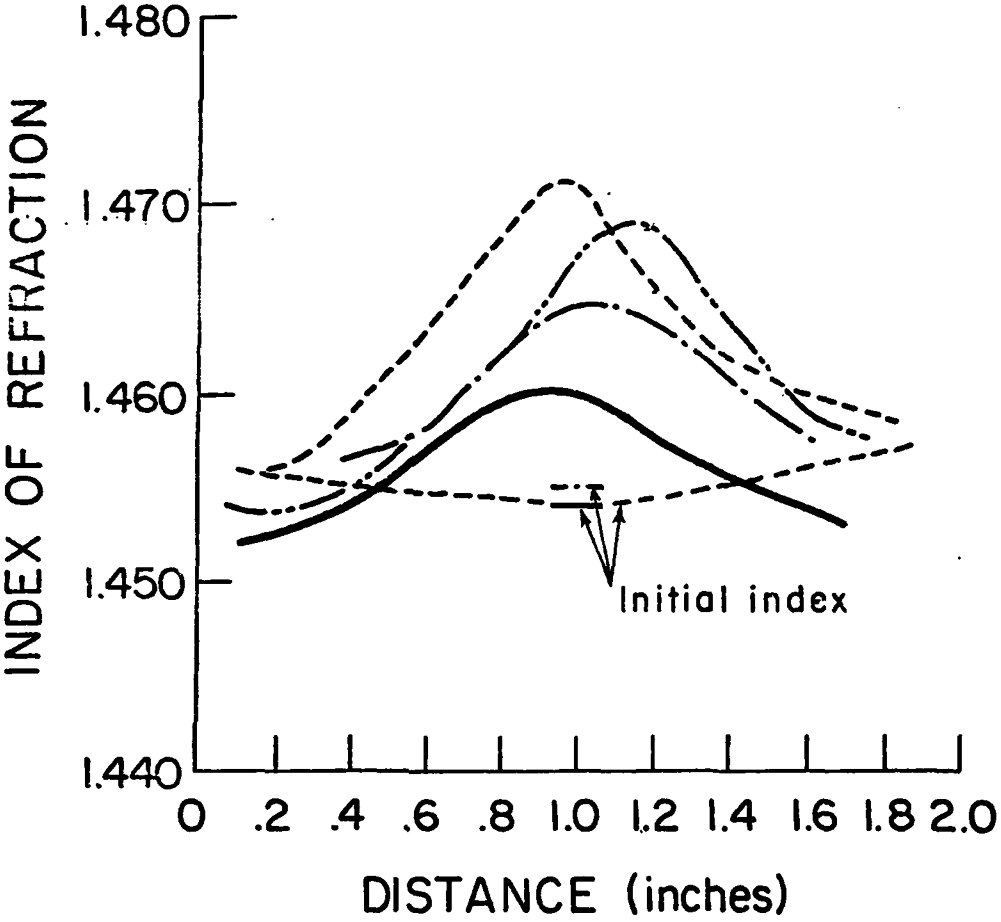

FIGURE 2

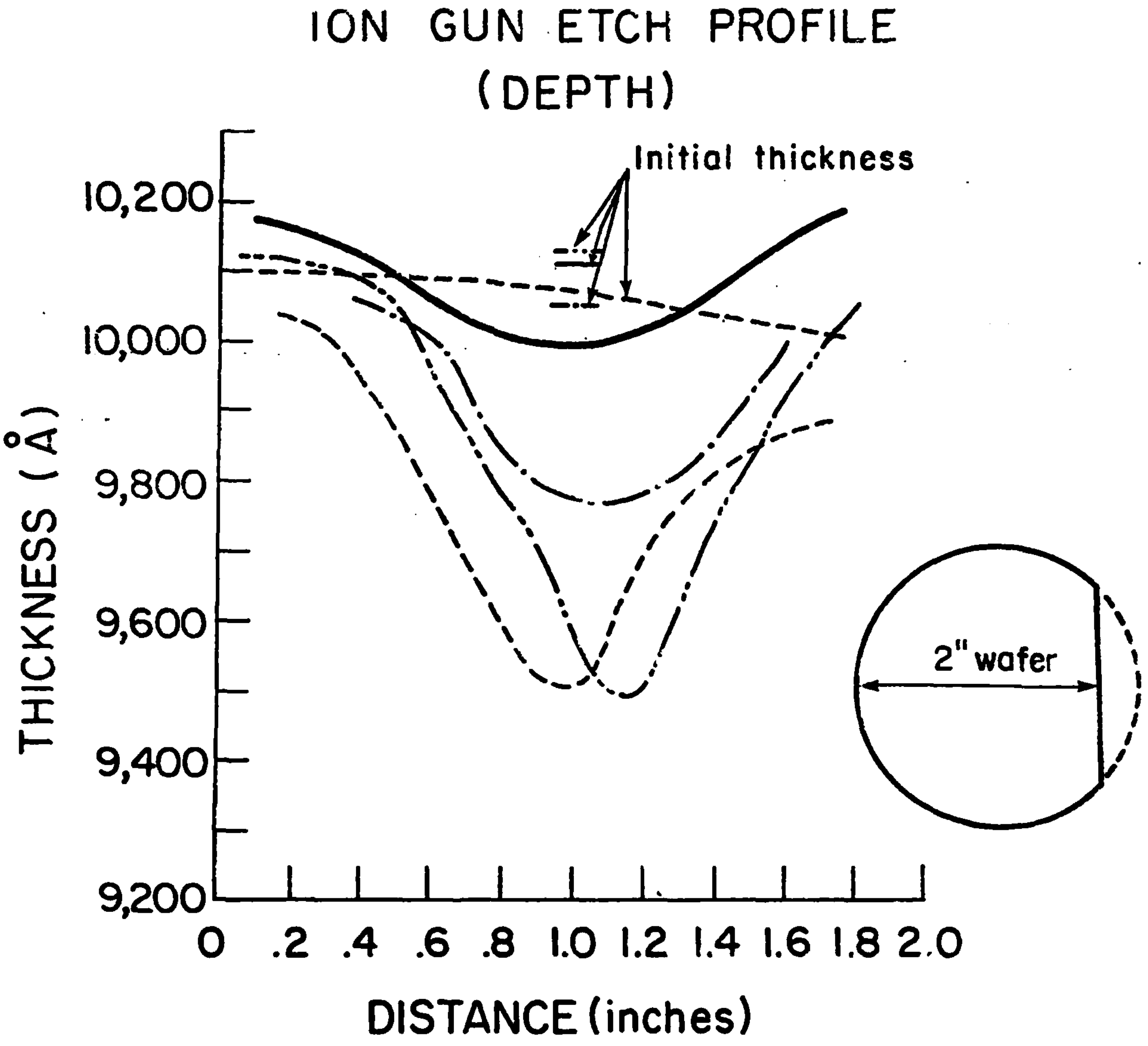
ION GUN ETCH PROFILE
(DEPTH)
Initial thickness
10,200
10,000
9,800
9,600
9,400
9,200
THICKNESS (Å)
0
.2
.4
.6
.8
1.0
1.2
1.4
1.6
1.8
2.0
DISTANCE (inches)
2" wafer

FIGURE 3

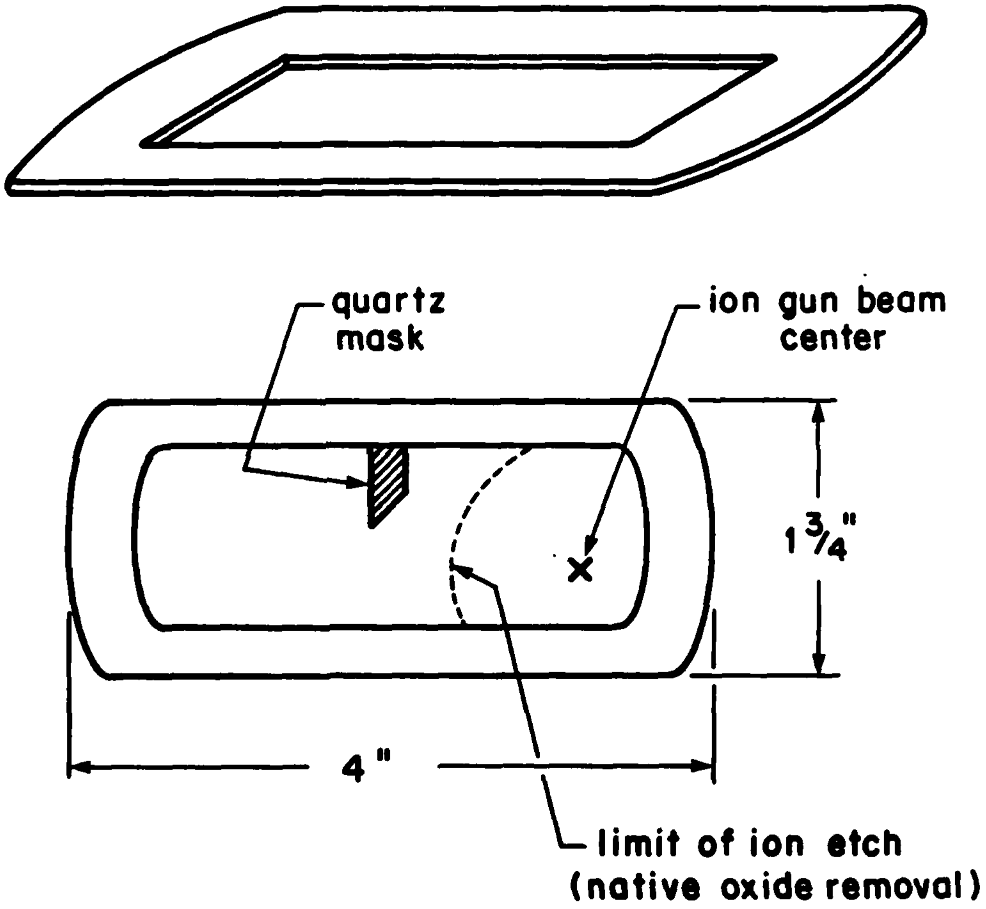

REACTIVE SPUTTERING DEPOSITION MASK

FIGURE 4

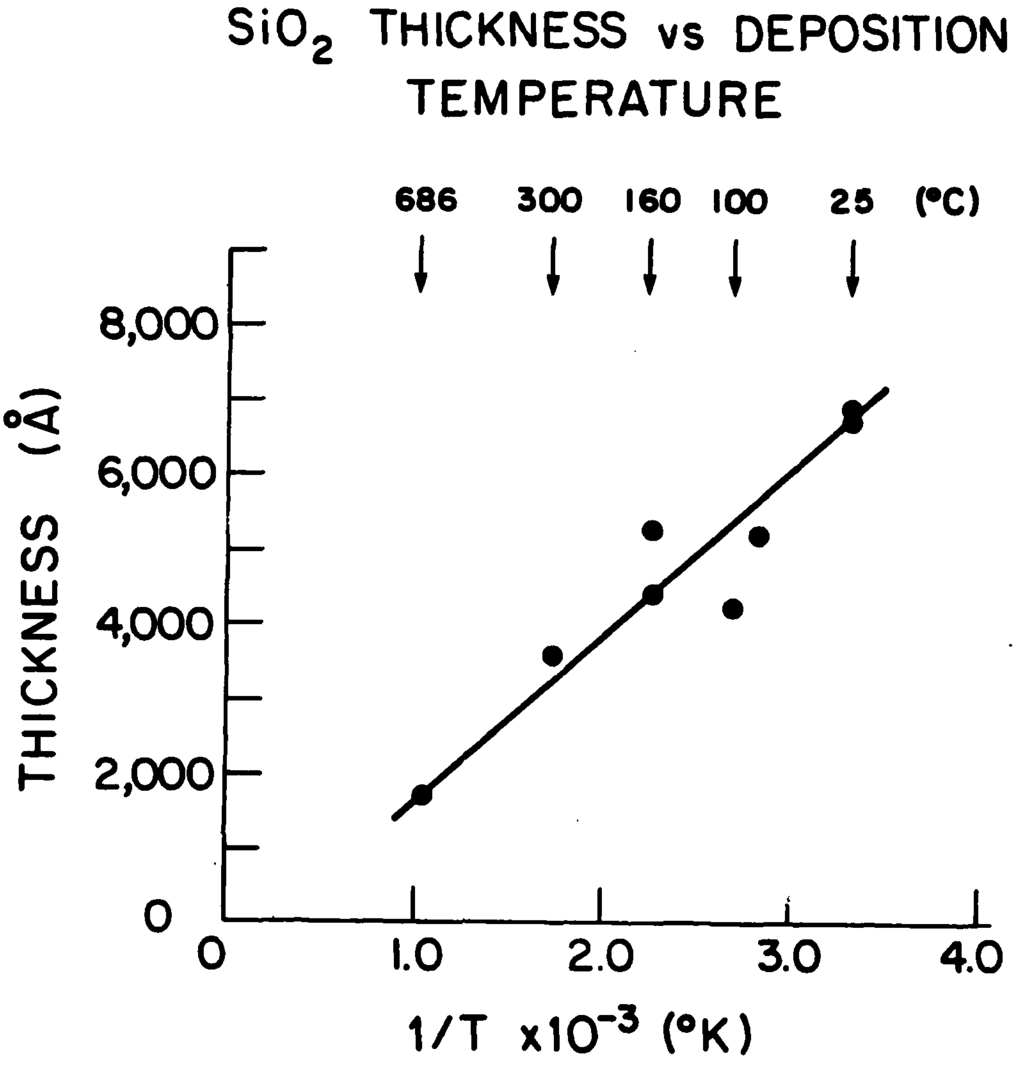
SiO_2 THICKNESS vs DEPOSITION TEMPERATURE
686
300
160
100
25
(°C)
THICKNESS (Å)
8,000
6,000
4,000
2,000
0
0
1.0
2.0
3.0
4.0
1/T x10^{-3} (°K)

FIGURE 5

FILM UNIFORMITY

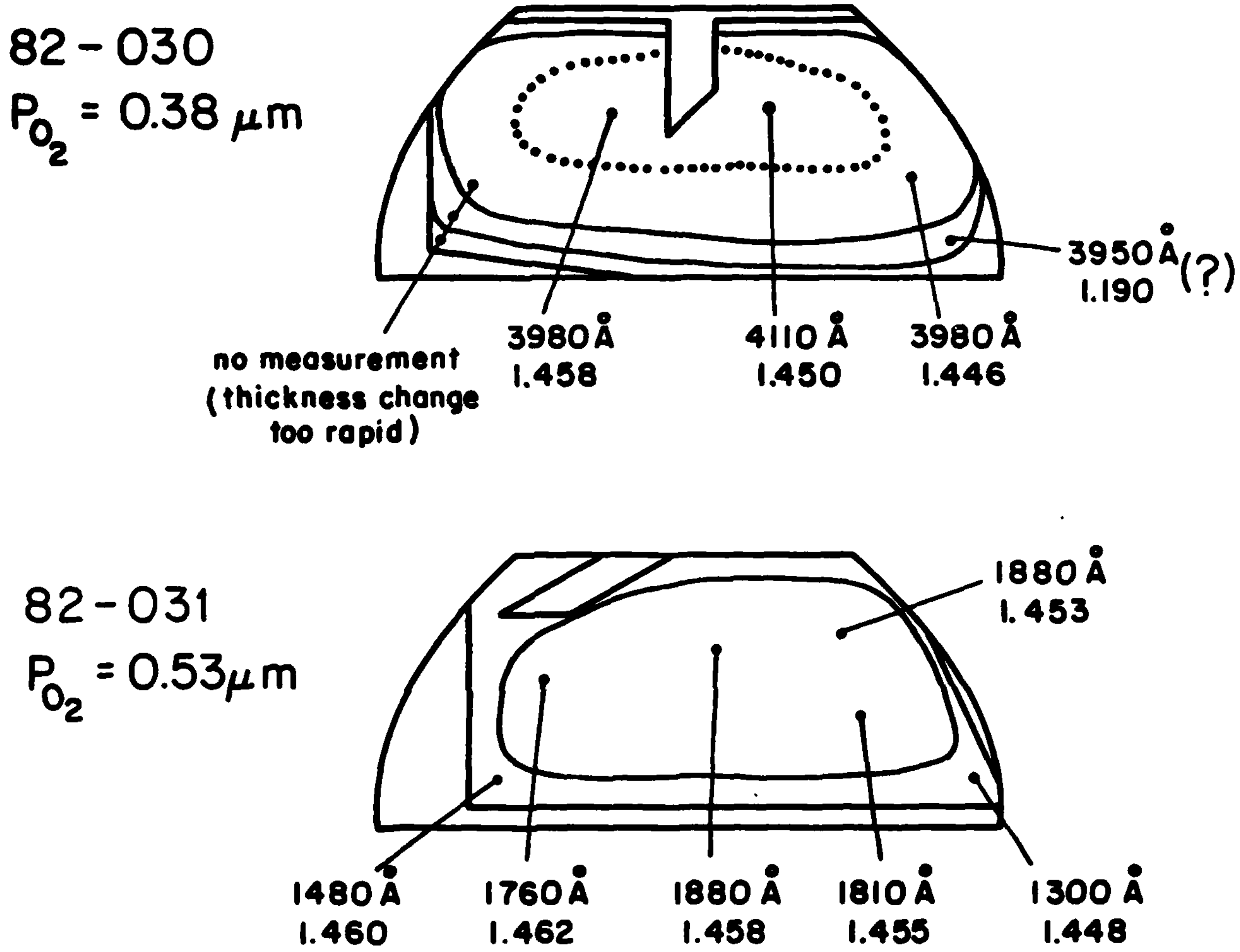

FIGURE 6

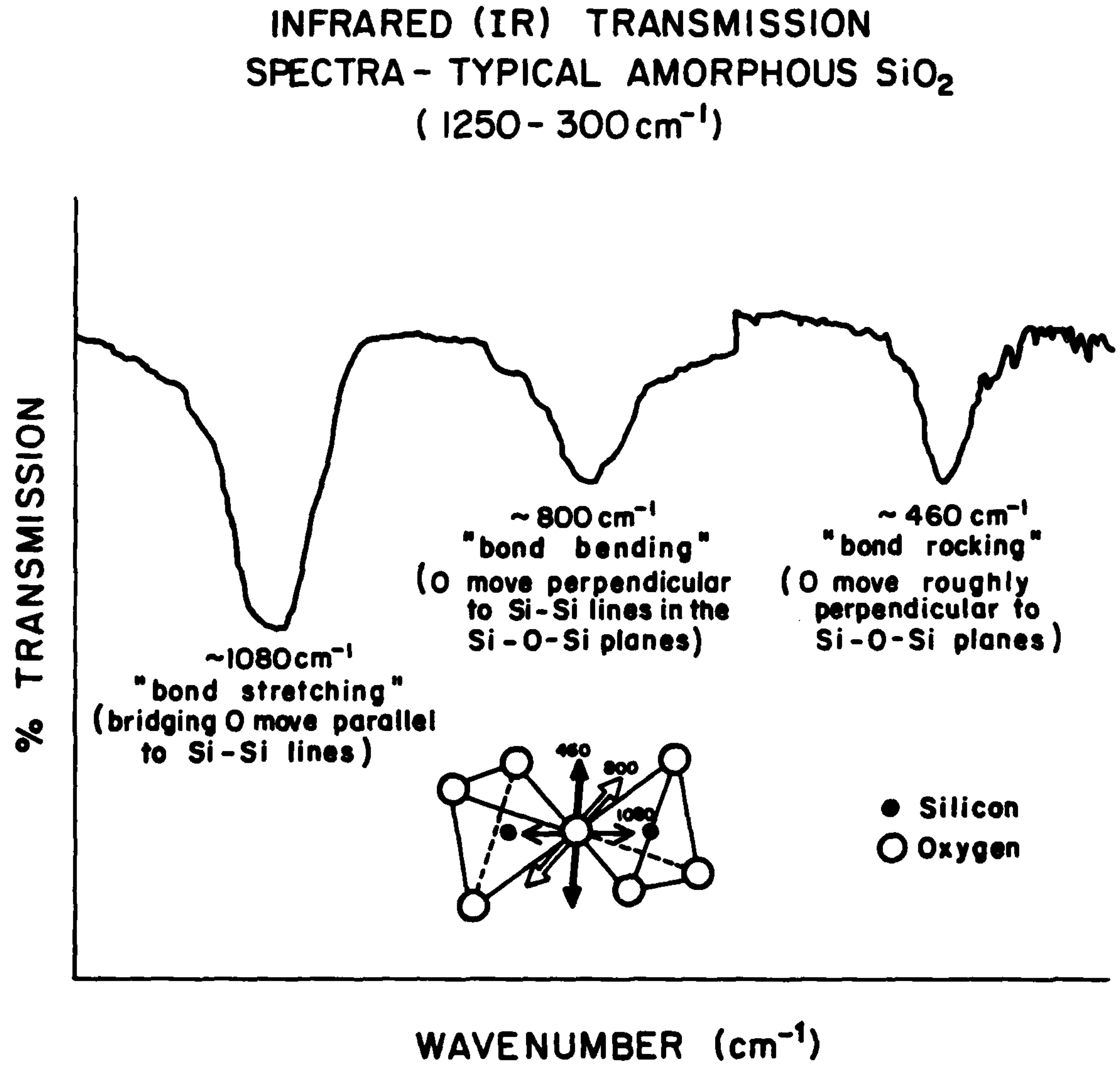

INFRARED (IR) TRANSMISSION SPECTRA - TYPICAL AMORPHOUS SiO_2 ($1250 - 300 cm^{-1}$)

FIGURE 7

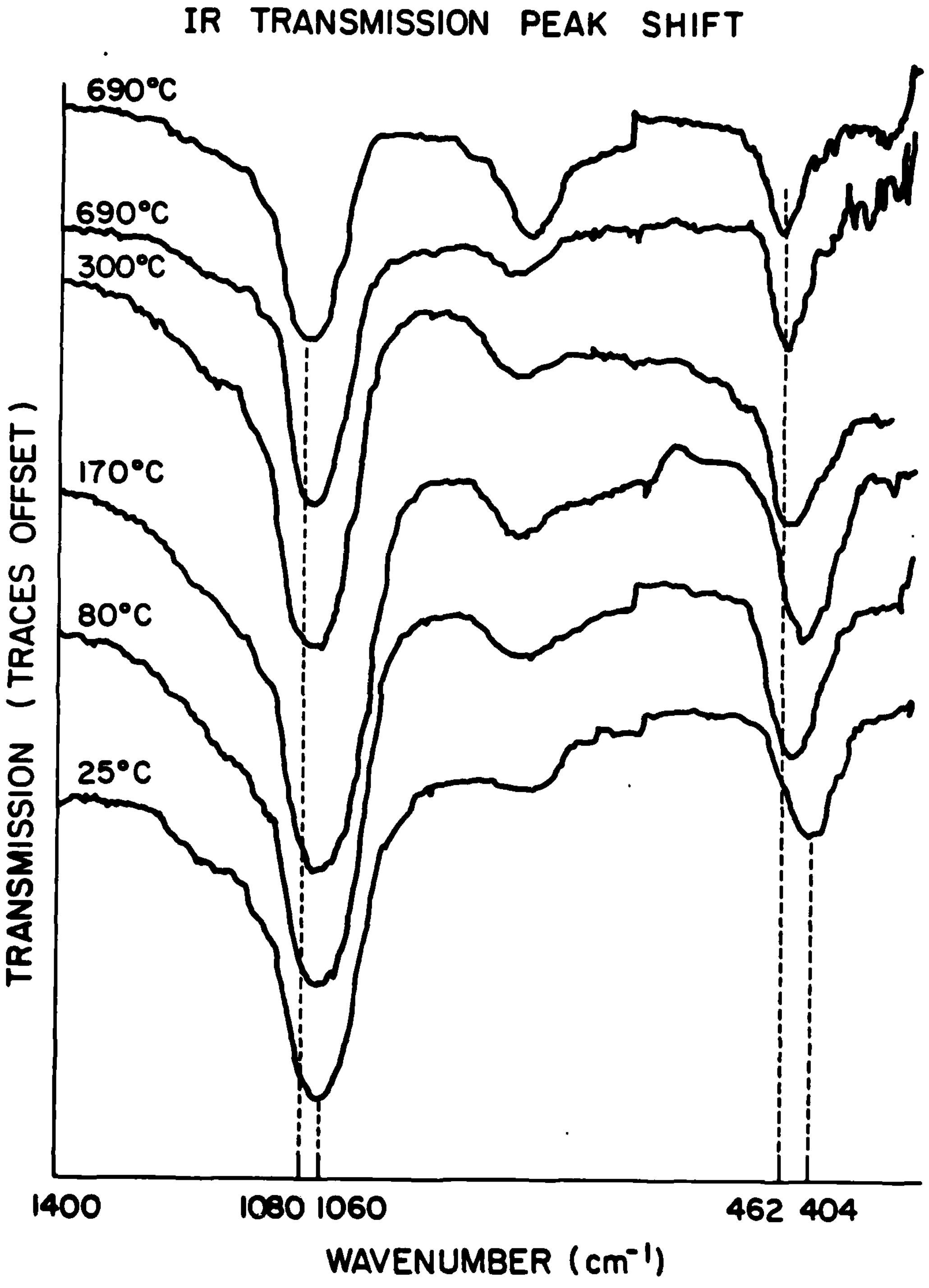
IR TRANSMISSION PEAK SHIFT
690°C
690°C
300°C
170°C
80°C
25°C
TRANSMISSION (TRACES OFFSET)
1400
1080
1060
462
404
WAVENUMBER (cm^{-1})

FIGURE 8

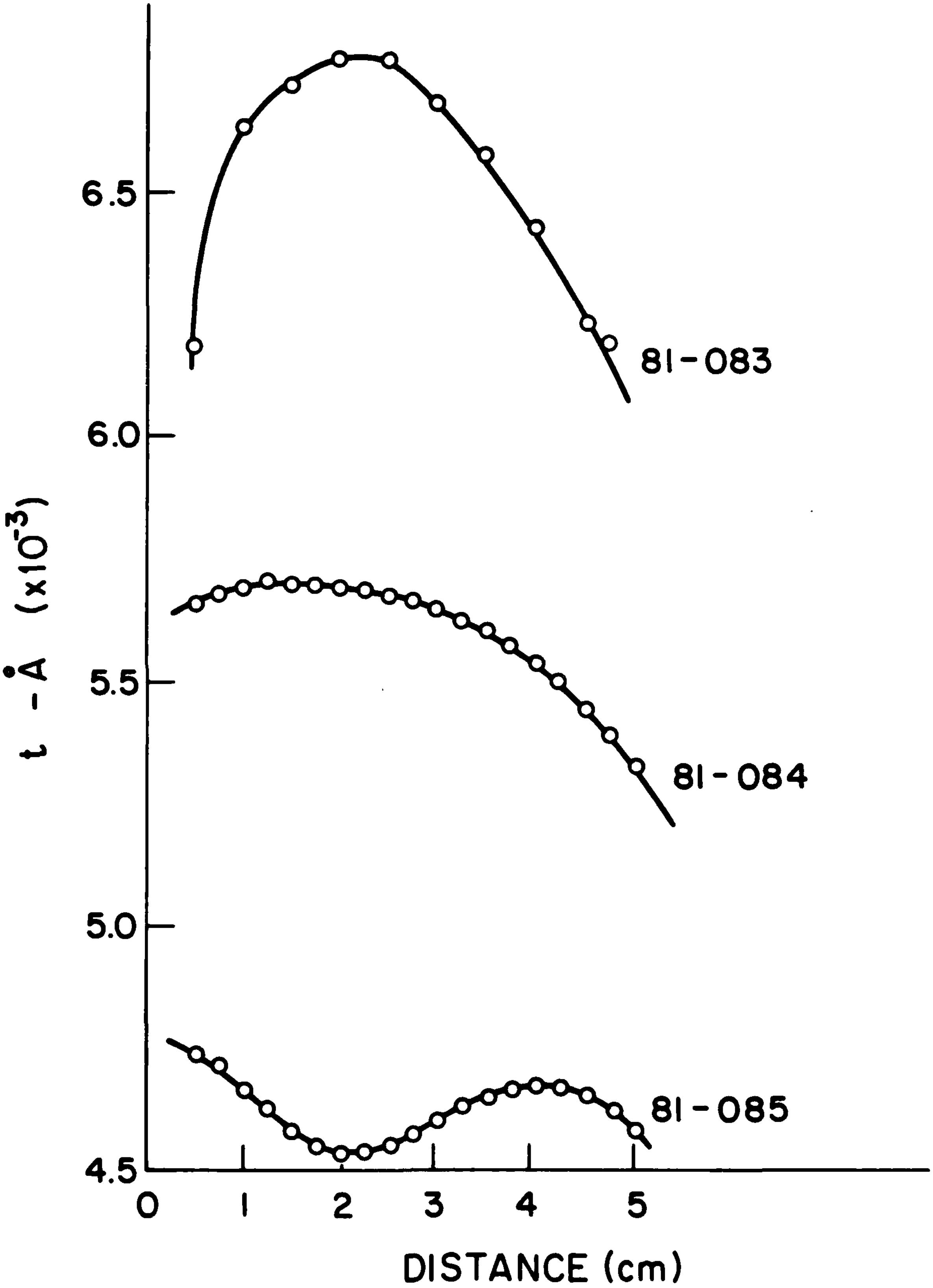

FIGURE 9

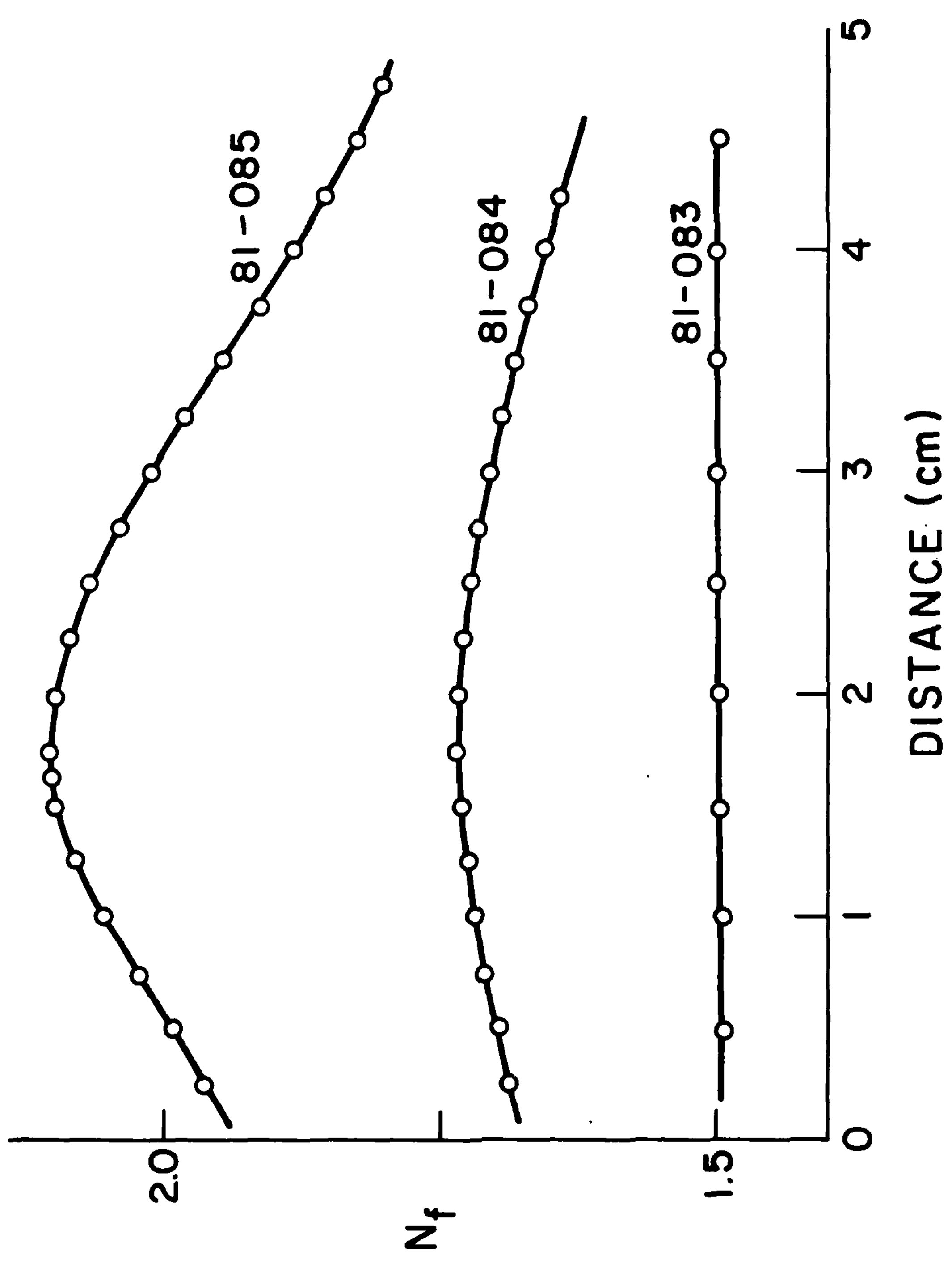

FIGURE 10

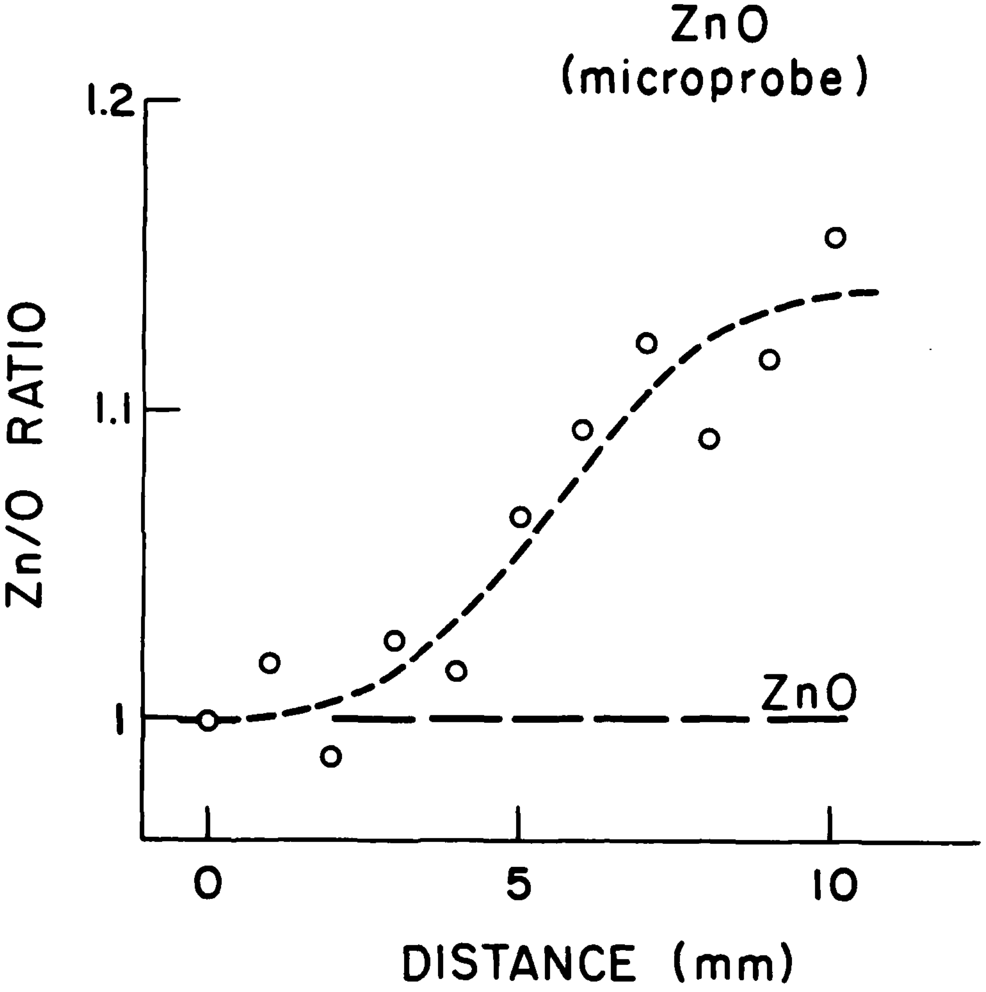

FIGURE 11

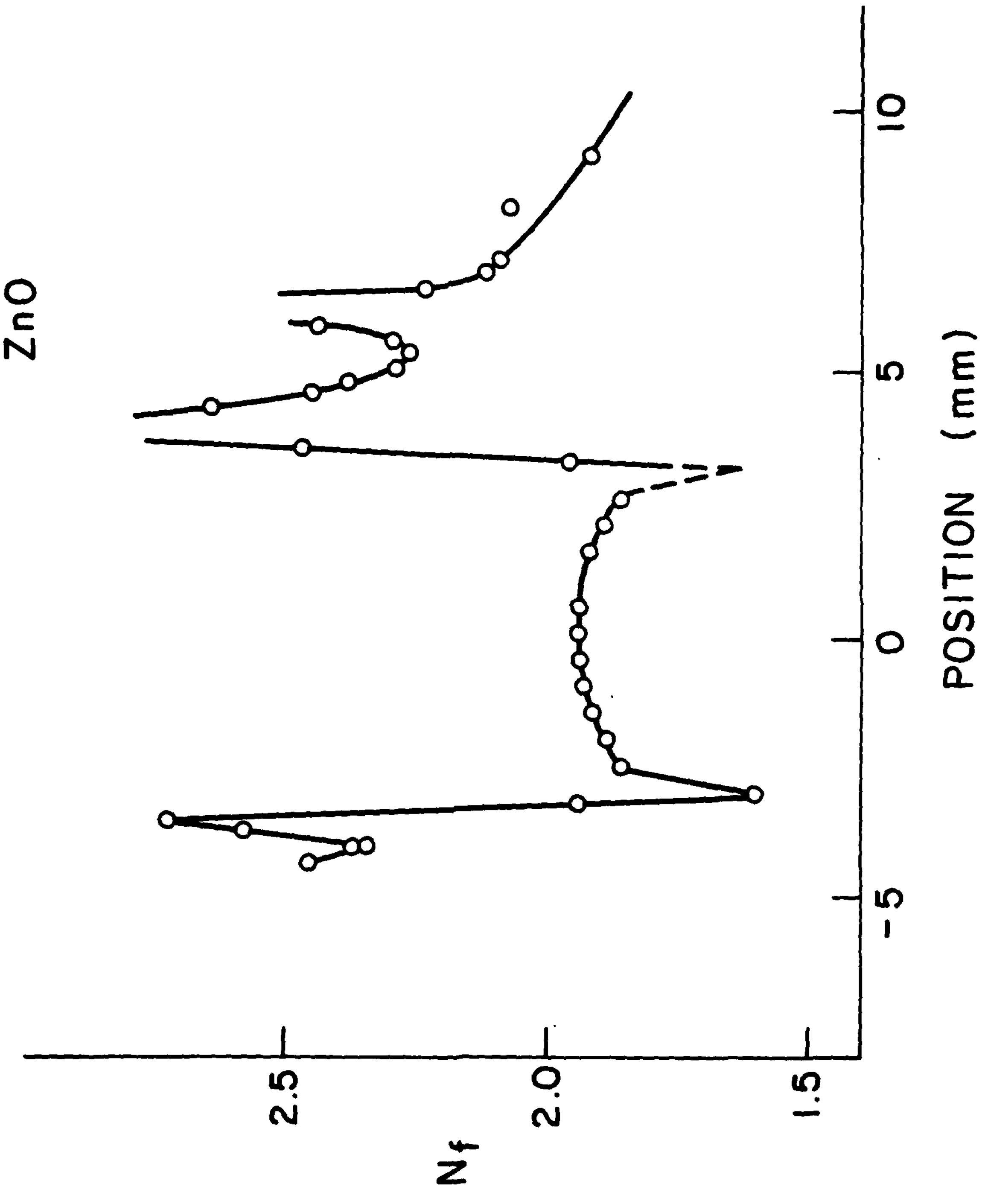

FIGURE 12

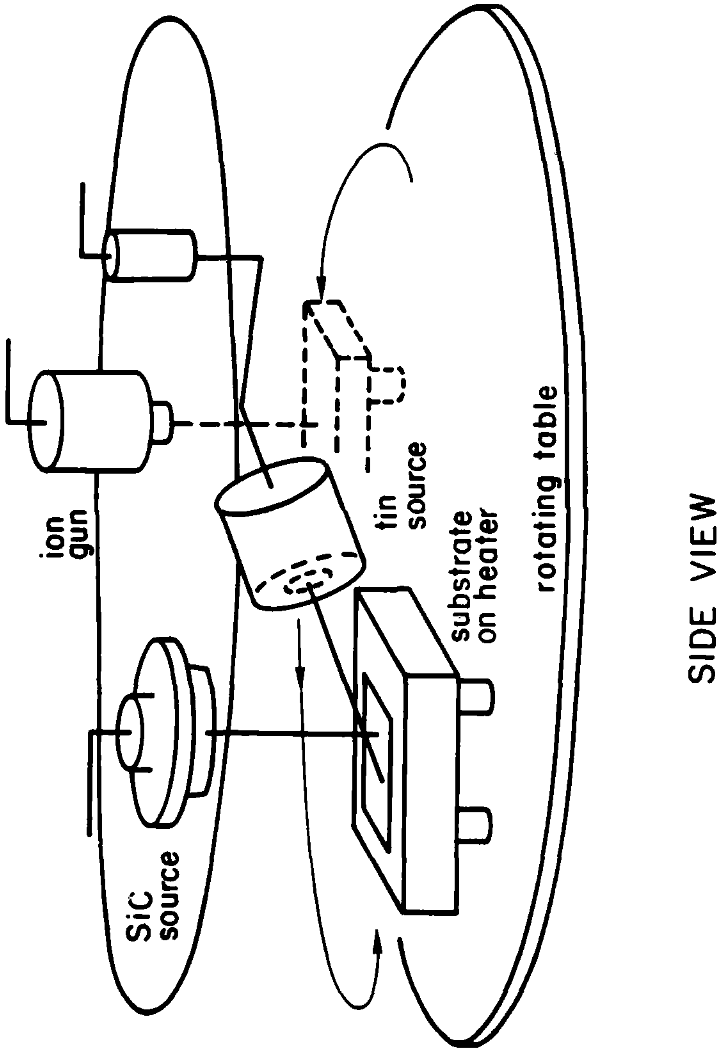
ion gun
tin source
substrate on heater
rotating table
SiC source
SIDE VIEW

FIGURE 13a

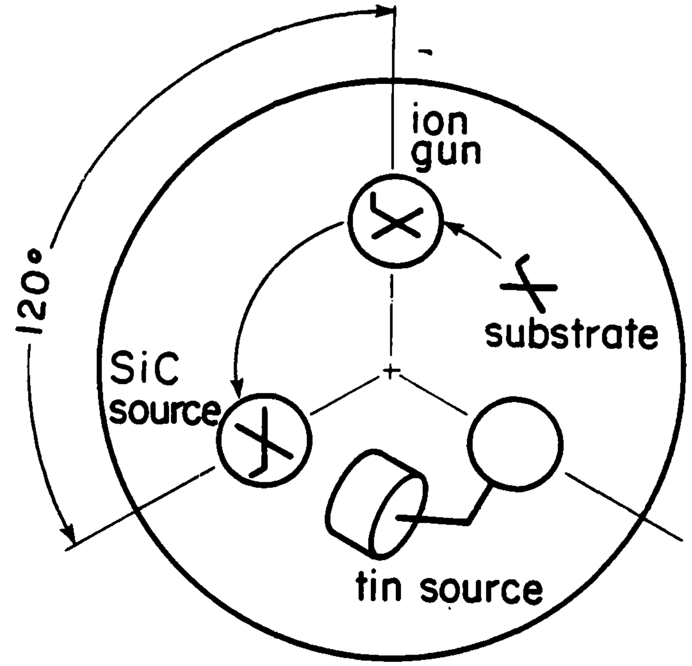

TOP VIEW

FIGURE 13b

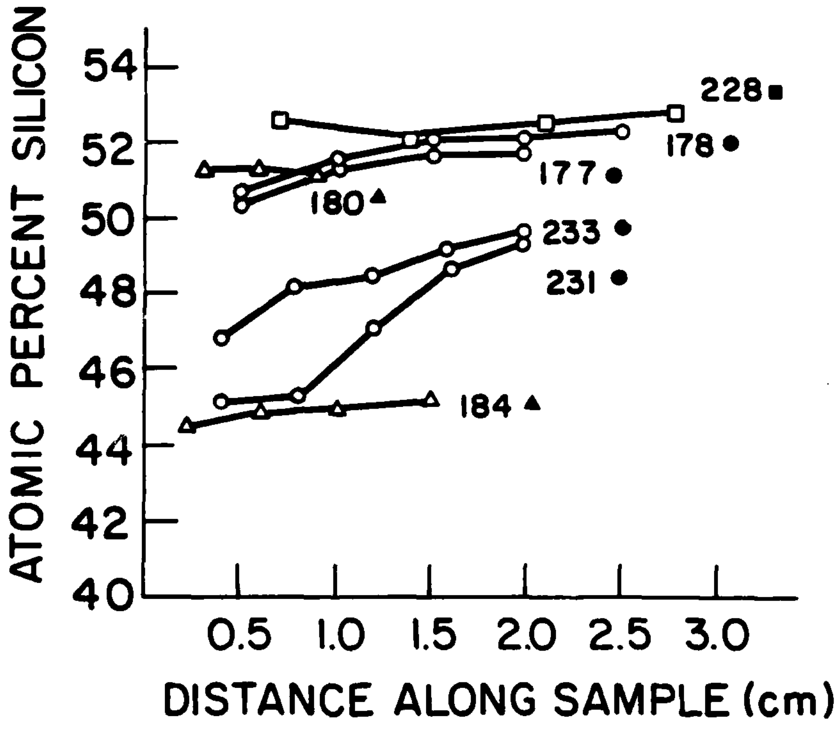
ATOMIC PERCENT SILICON
54
52
50
48
46
44
42
40
0.5
1.0
1.5
2.0
2.5
3.0
DISTANCE ALONG SAMPLE (cm)
228 ■
178 ●
177 ●
180 ▲
233 ●
231 ●
184 ▲

FIGURE 14

TWO SOURCE SPUTTERING CONFIGURATION

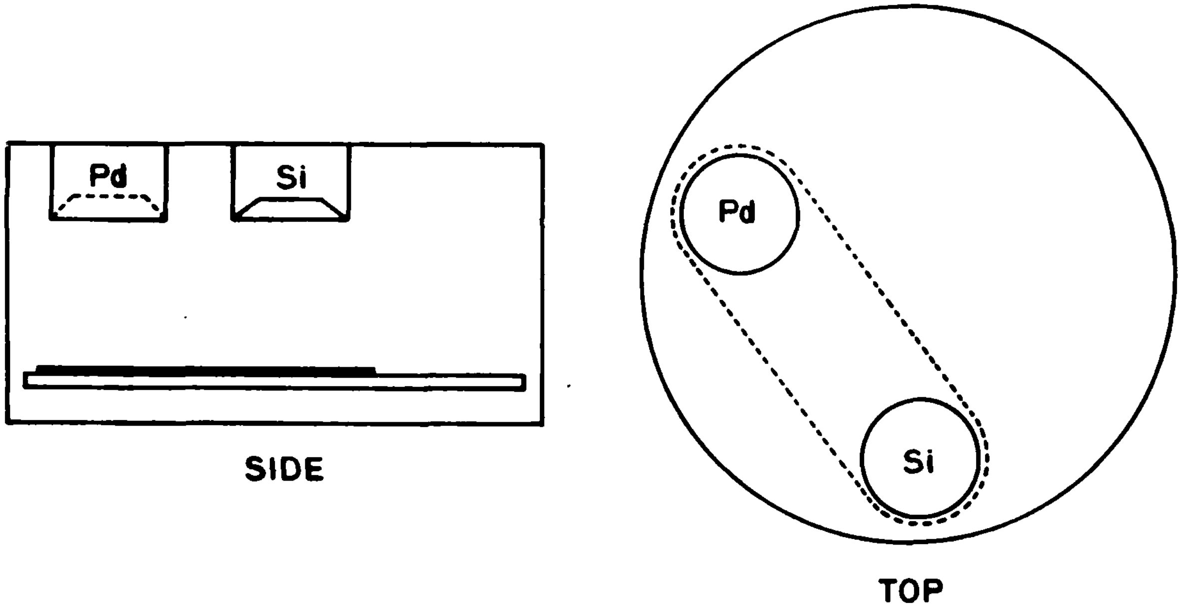

FIGURE 16

Silicon Deposition Rate (R. F. mode)

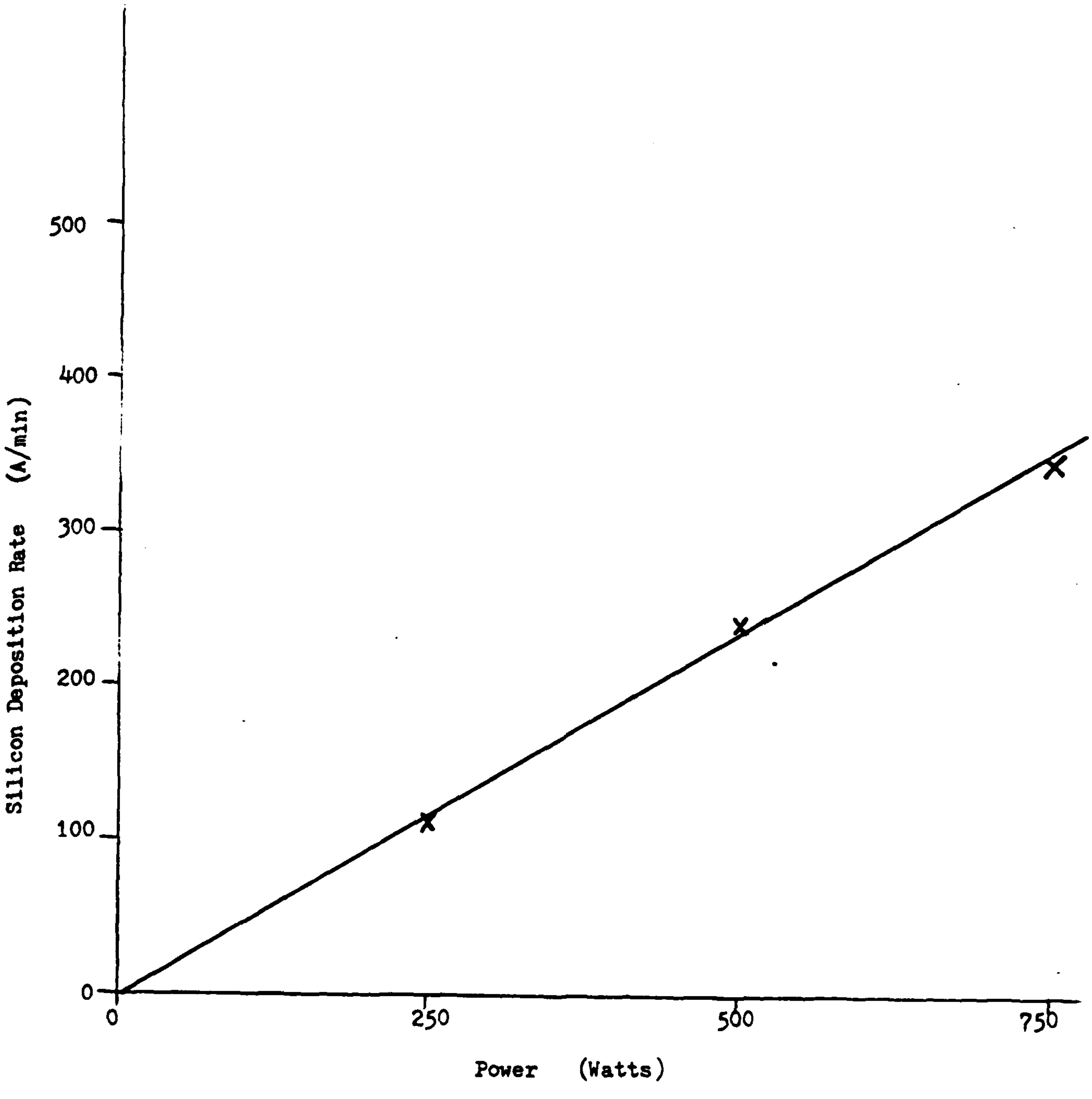

FIGURE 17

Palladium Deposition Rate (D. C. mode)

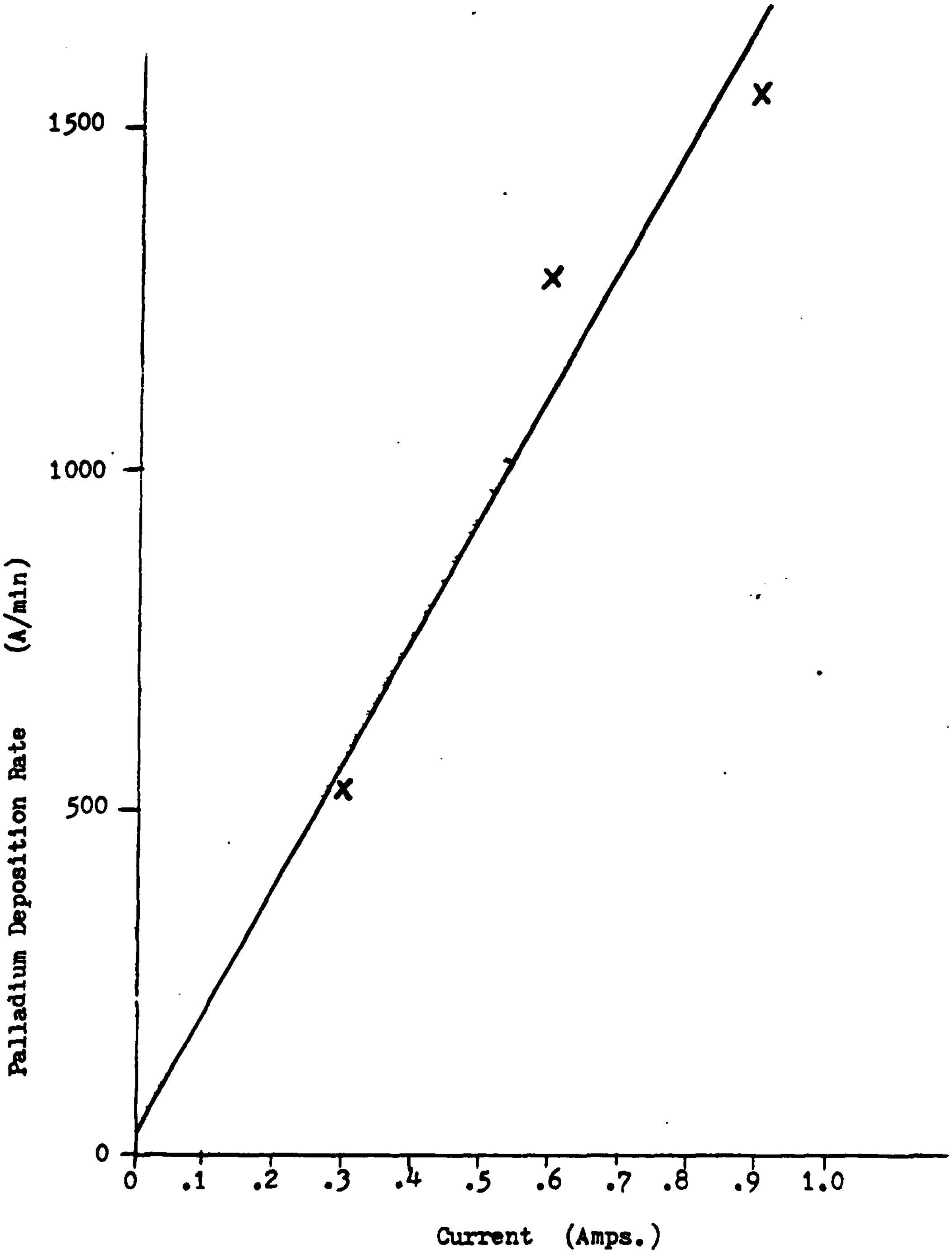

FIGURE 18

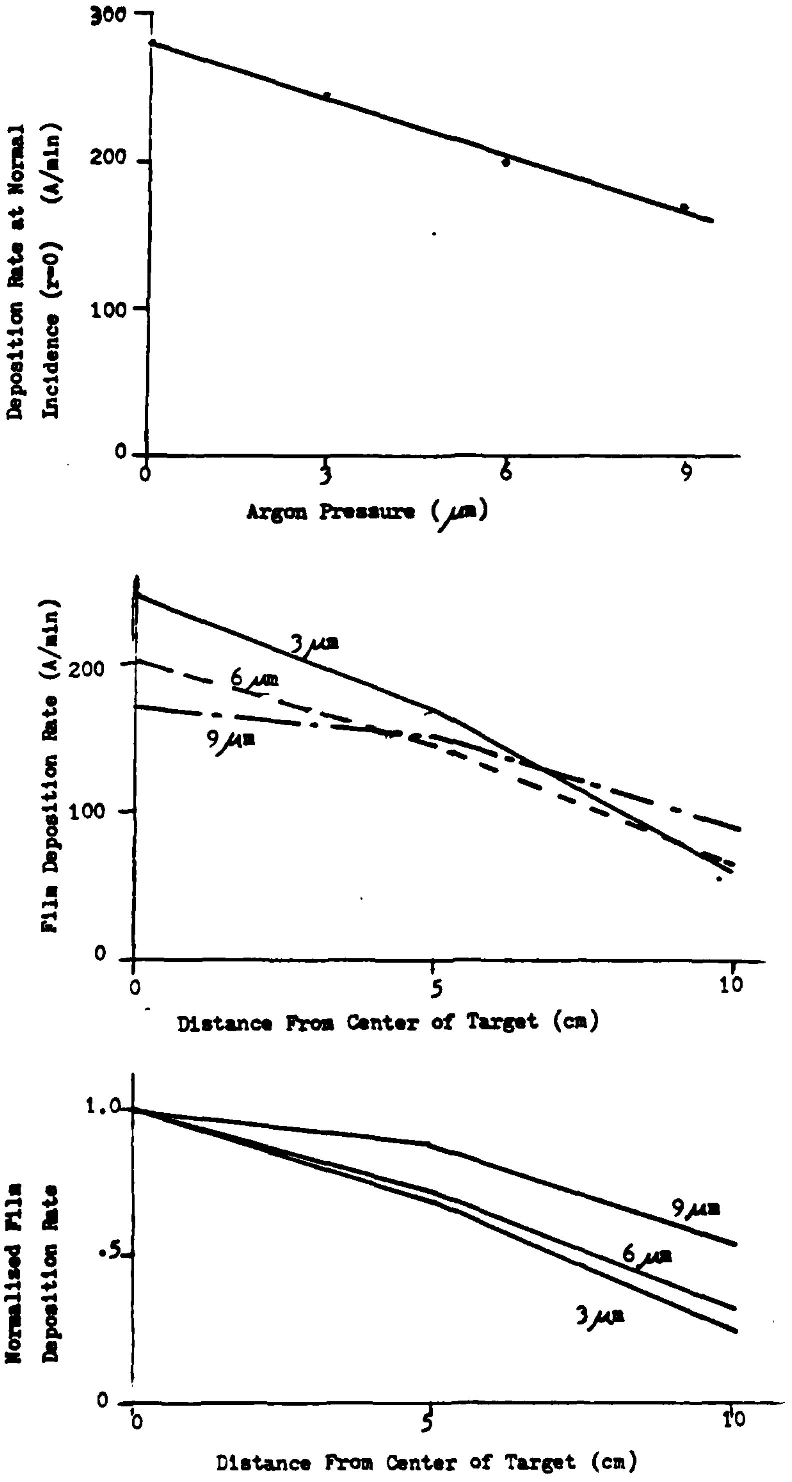
300
200
100
0
Deposition Rate at Normal Incidence (r=0) (A/min)
0
3
6
9
Argon Pressure (μm)
200
100
0
Film Deposition Rate (A/min)
3 μm
6 μm
9 μm
0
5
10
Distance From Center of Target (cm)
1.0
.5
0
Normalized Film Deposition Rate
9 μm
6 μm
3 μm
0
5
10
Distance From Center of Target (cm)

FIGURE 19

Palladium-Silicon Phase Spread

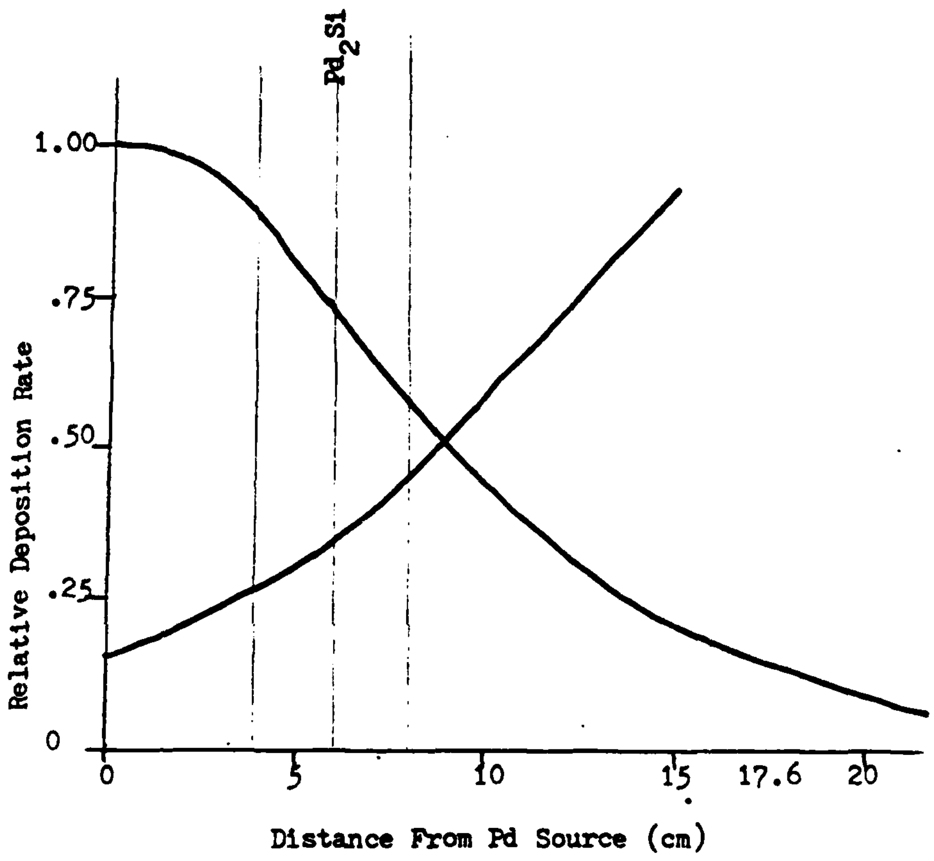

Pd_2Si should occur at 6.0 cm from the Pd source.

$$\frac{\text{Atomic density of Pd} = 6.8 \times 10^{22}/cm^3}{\text{Atomic density of Si} = 5.0 \times 10^{22}/cm^3} = \frac{1.36}{1}$$

Therefore for equal atomic rates the Si source must deposit 1.36 times the thickness of the Pd source.

FIGURE 20

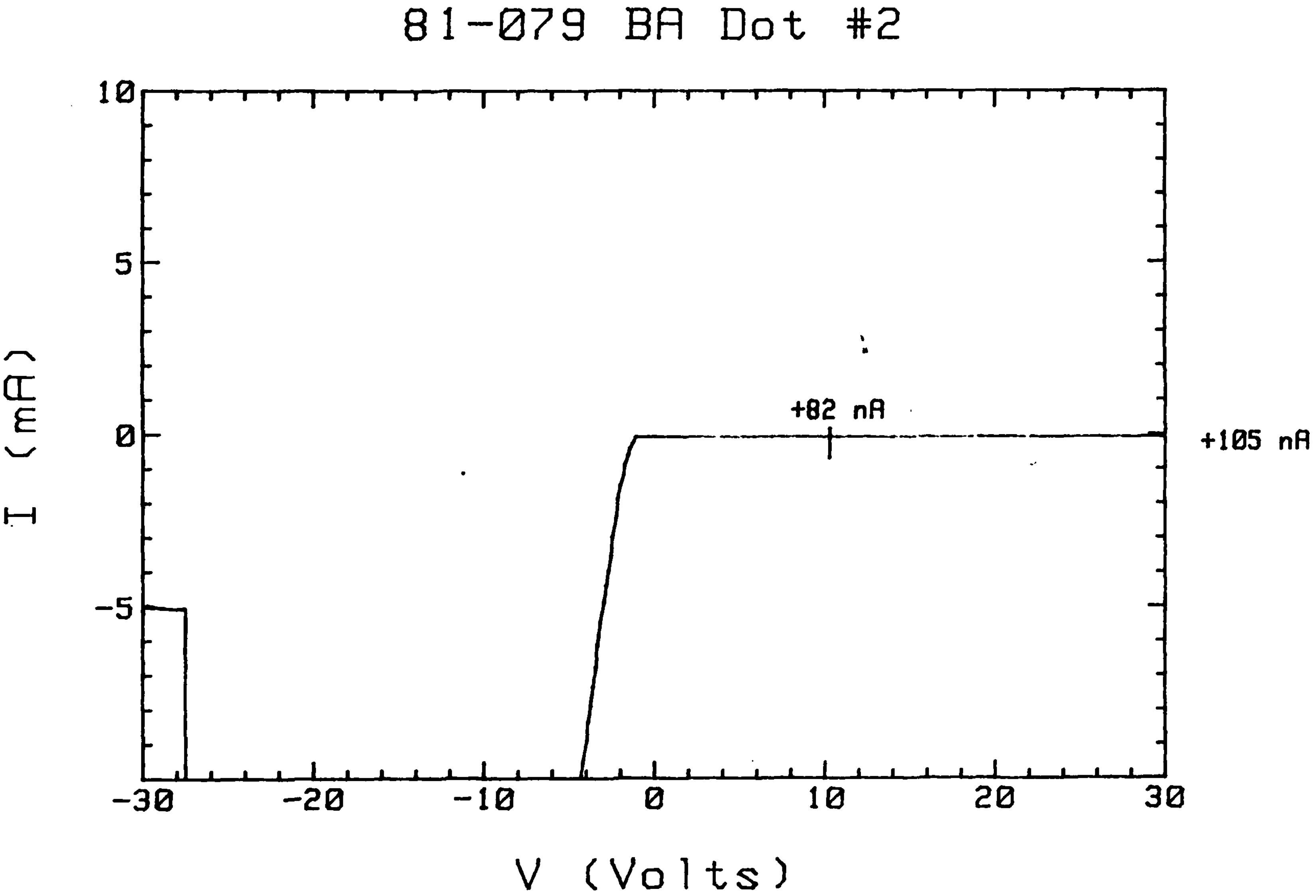

FIGURE 21a

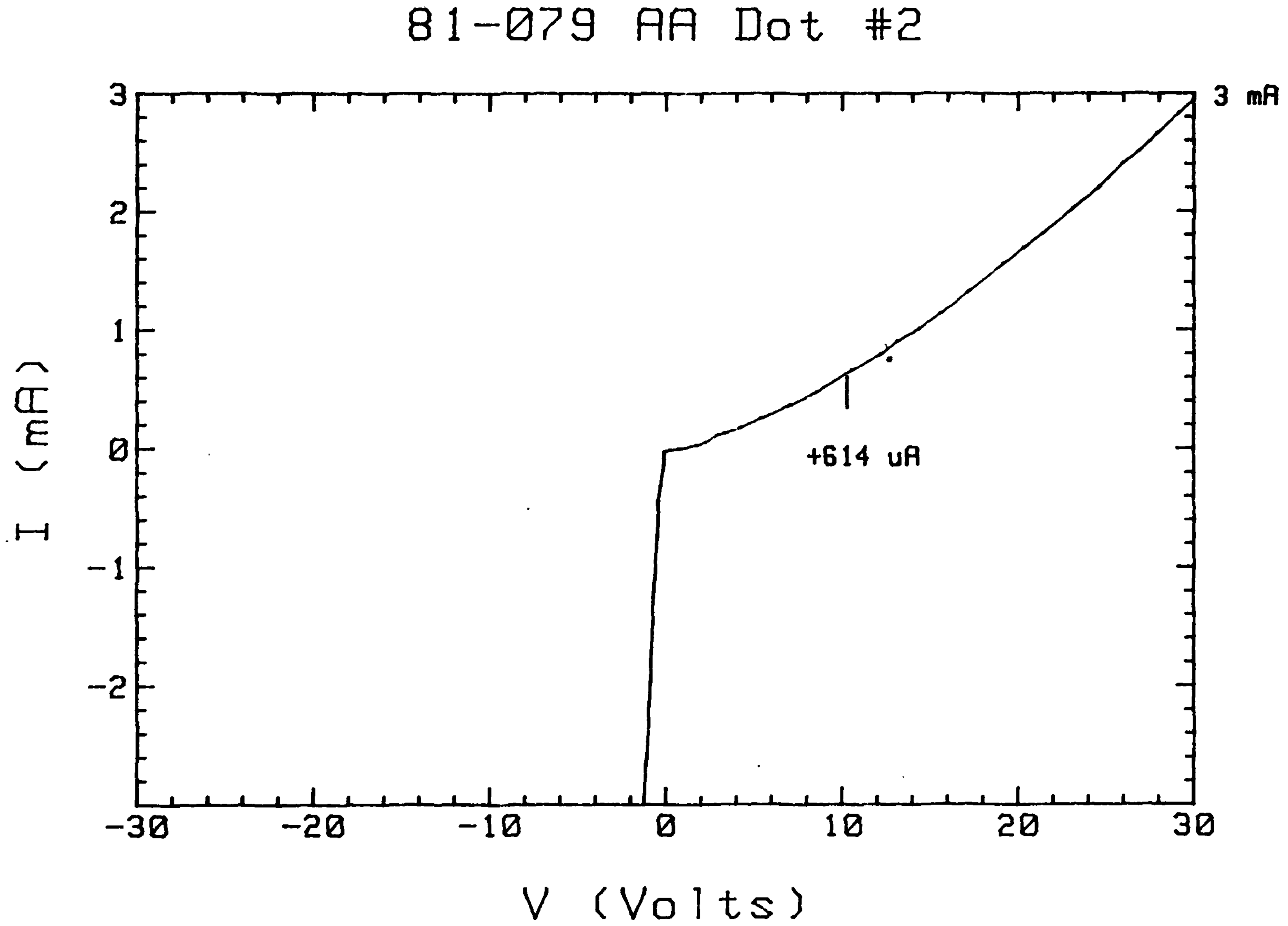

FIGURE 21b

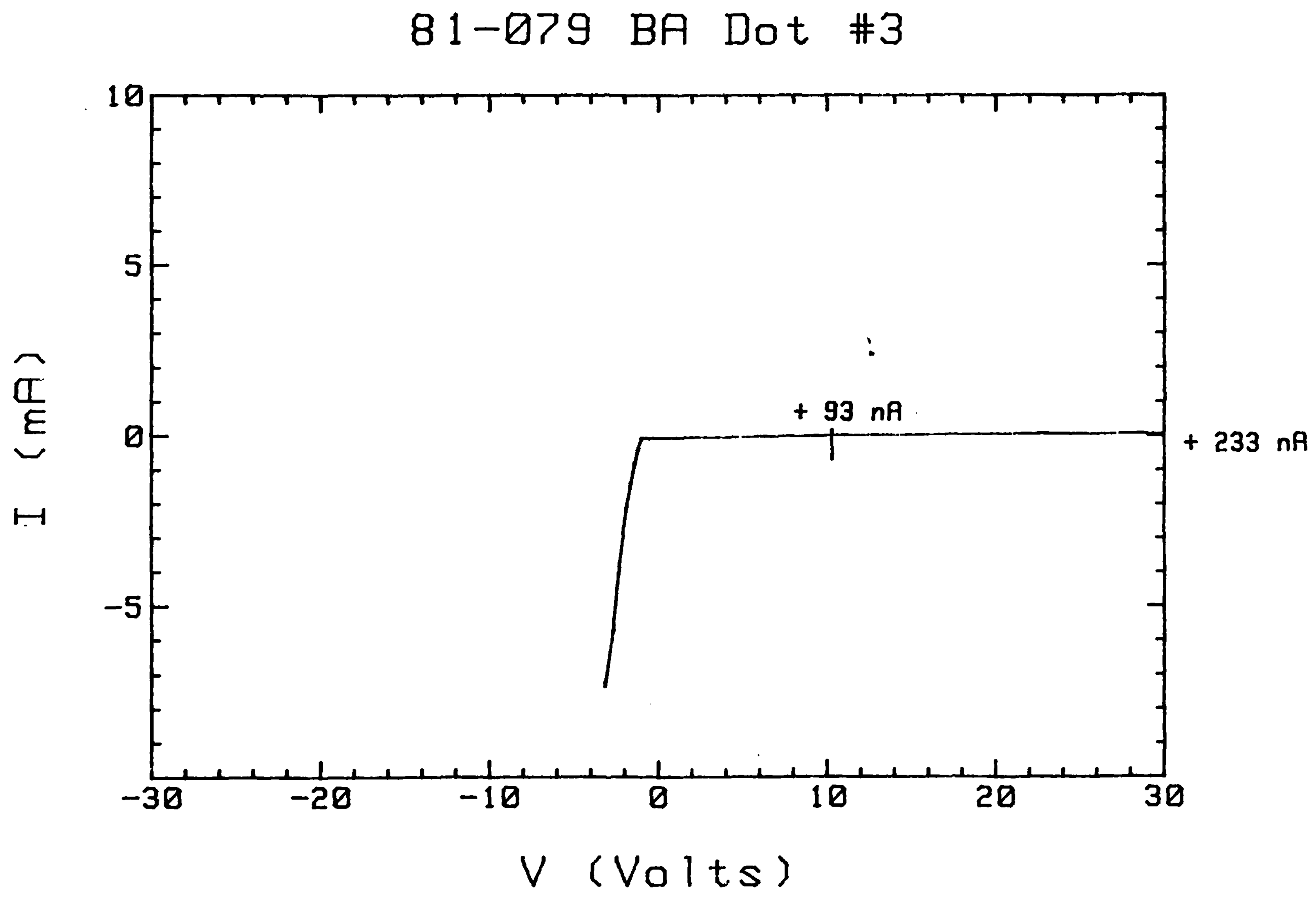

FIGURE 22a

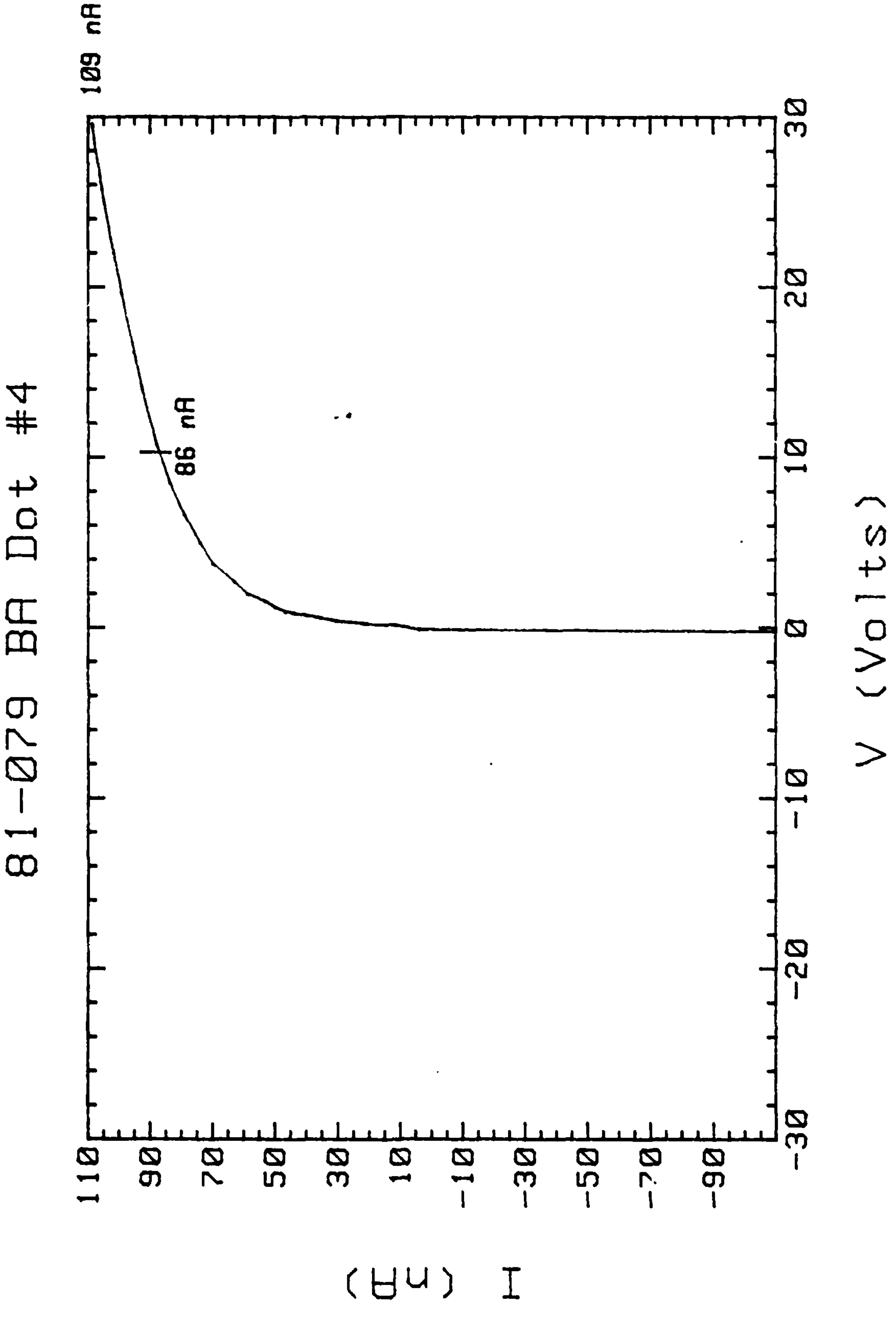
81-079 BA Dot #4
109 nA
86 nA
I (nA)
110
90
70
50
30
10
-10
-30
-50
-70
-90
V (Volts)
-30
-20
-10
0
10
20
30

FIGURE 22b

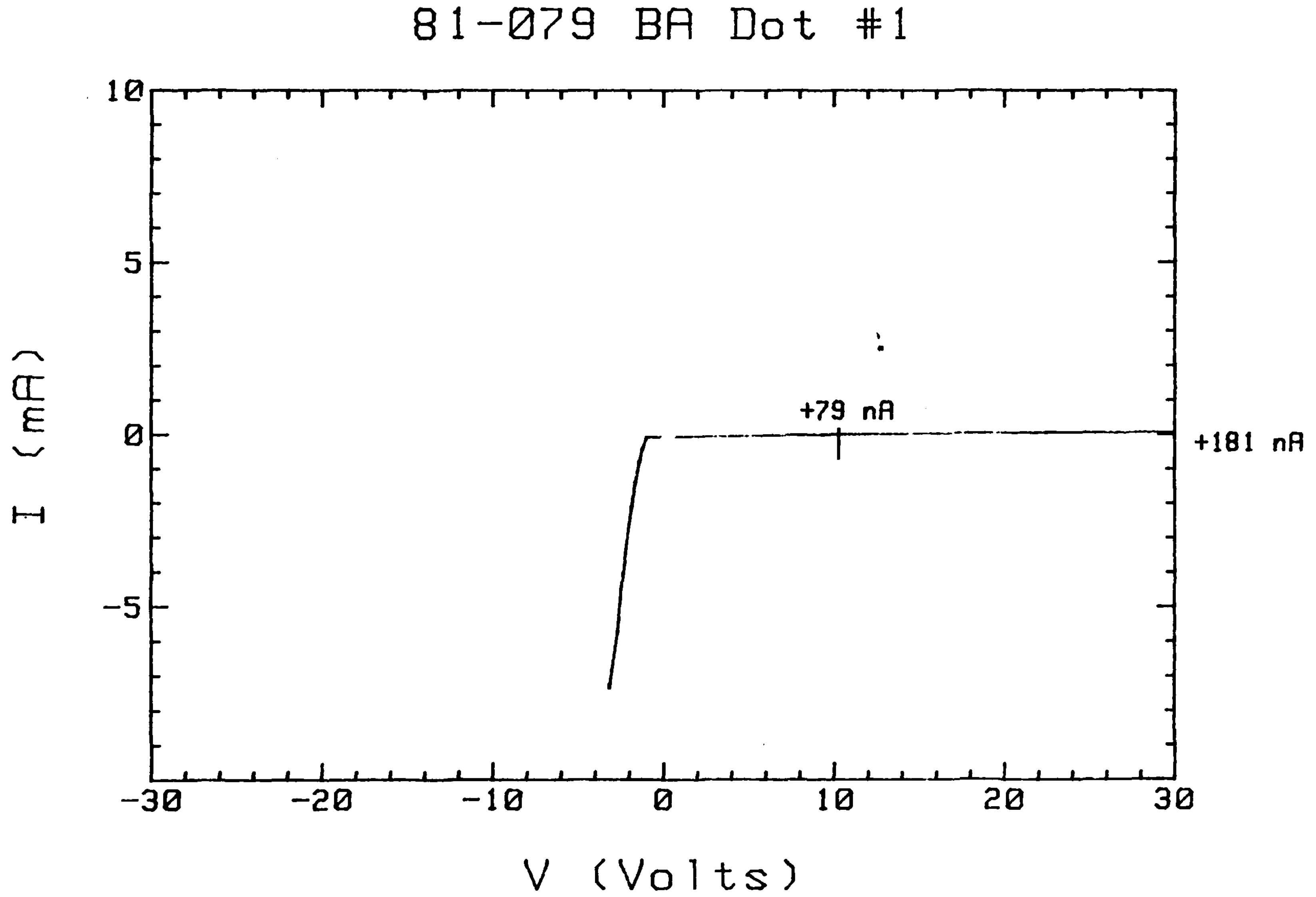

FIGURE 22c

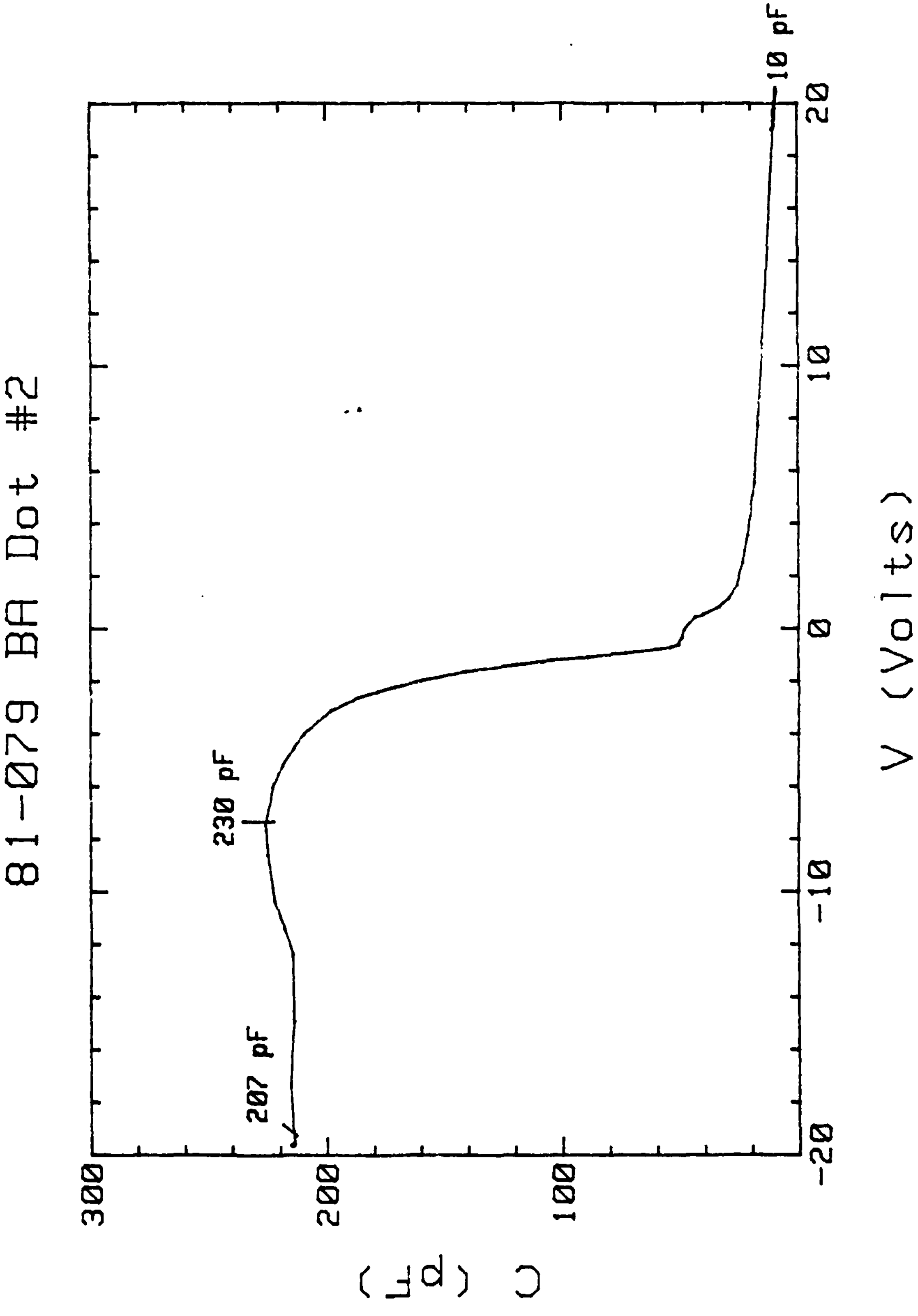
81-079 BA Dot #2
C (pF)
300
200
100
-20
-10
0
10
20
V (Volts)
207 pF
230 pF
10 pF

FIGURE 23a

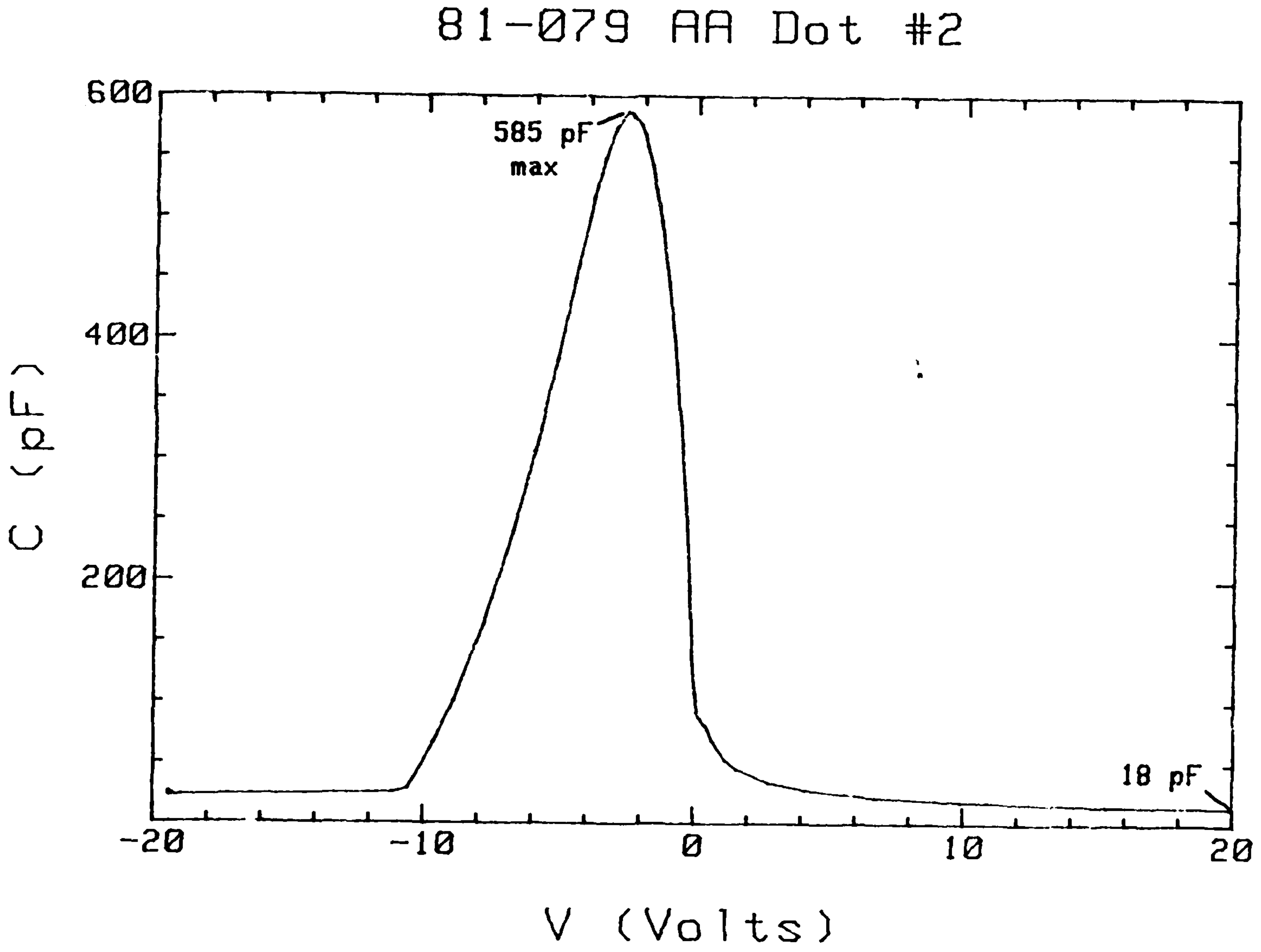
81-079 AA Dot #2
585 pF
max
18 pF
600
400
200
C (pF)
-20
-10
0
10
20
V (Volts)

FIGURE 23b

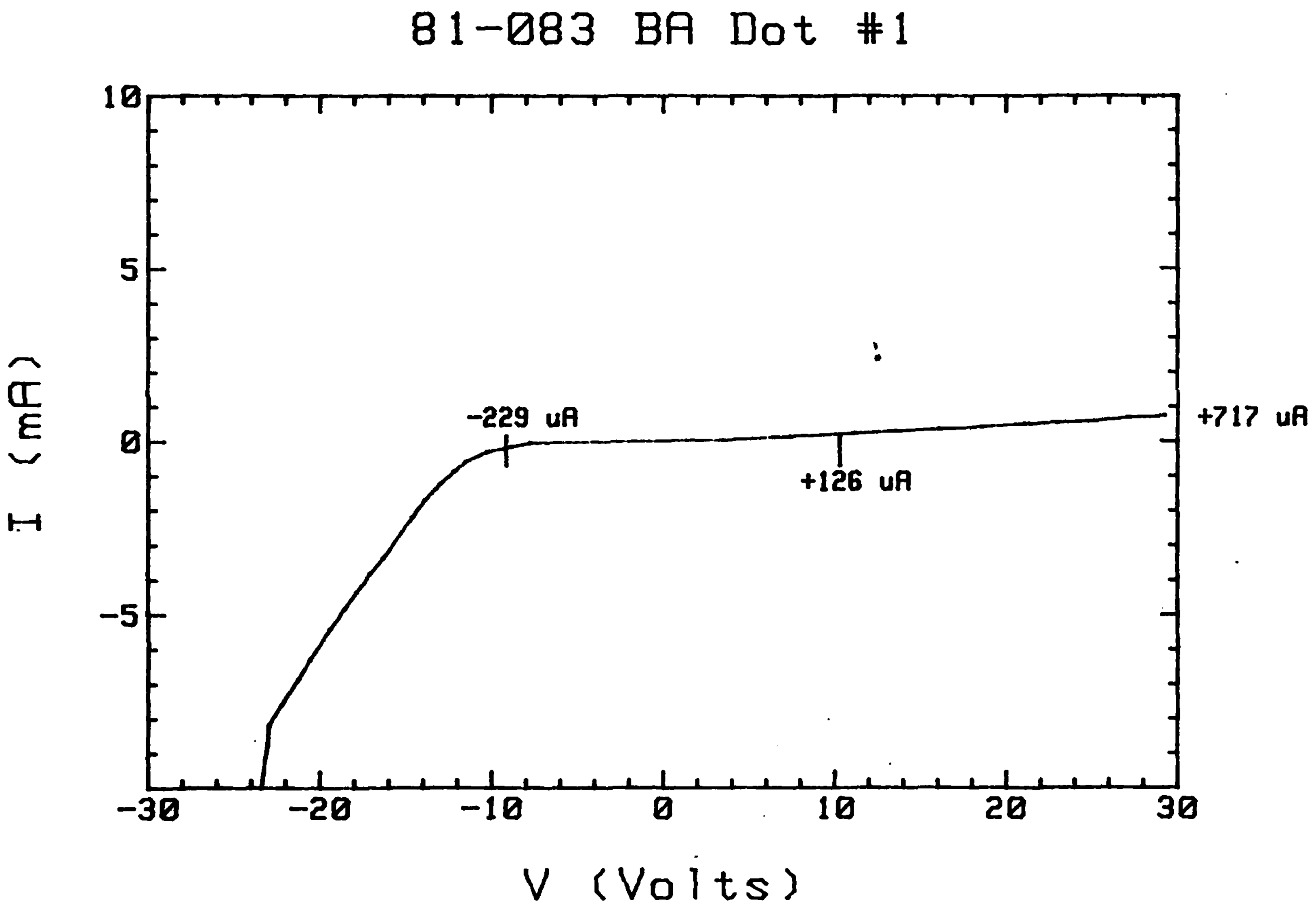
81-083 BA Dot #1
10
5
0
-5
I (mA)
-30
-20
-10
0
10
20
30
V (Volts)
-229 uA
+126 uA
+717 uA

FIGURE 24a

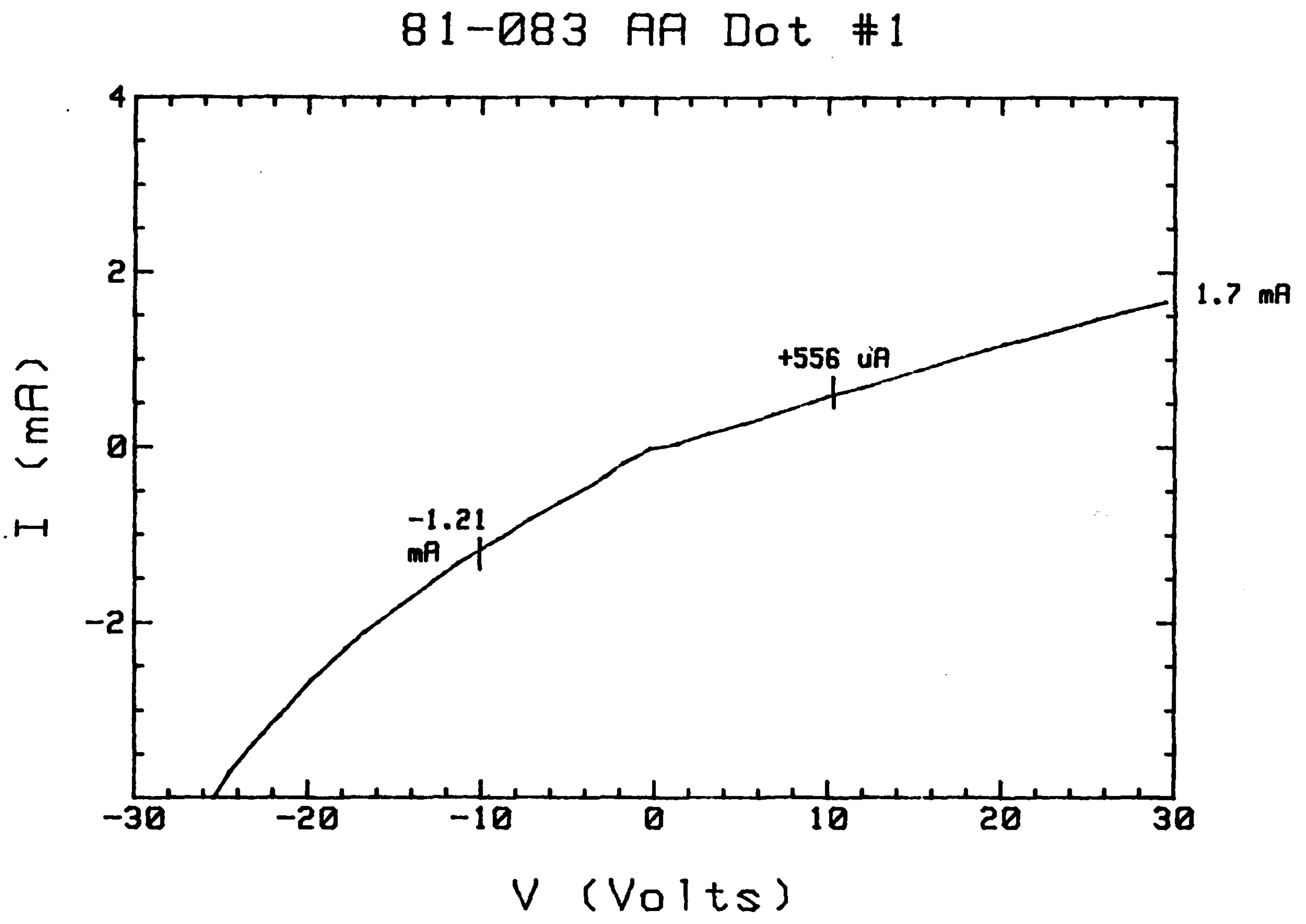
81-083 AA Dot #1
I (mA)
4
2
0
-2
1.7 mA
+556 uA
-1.21 mA
-30
-20
-10
0
10
20
30
V (Volts)

FIGURE 24b

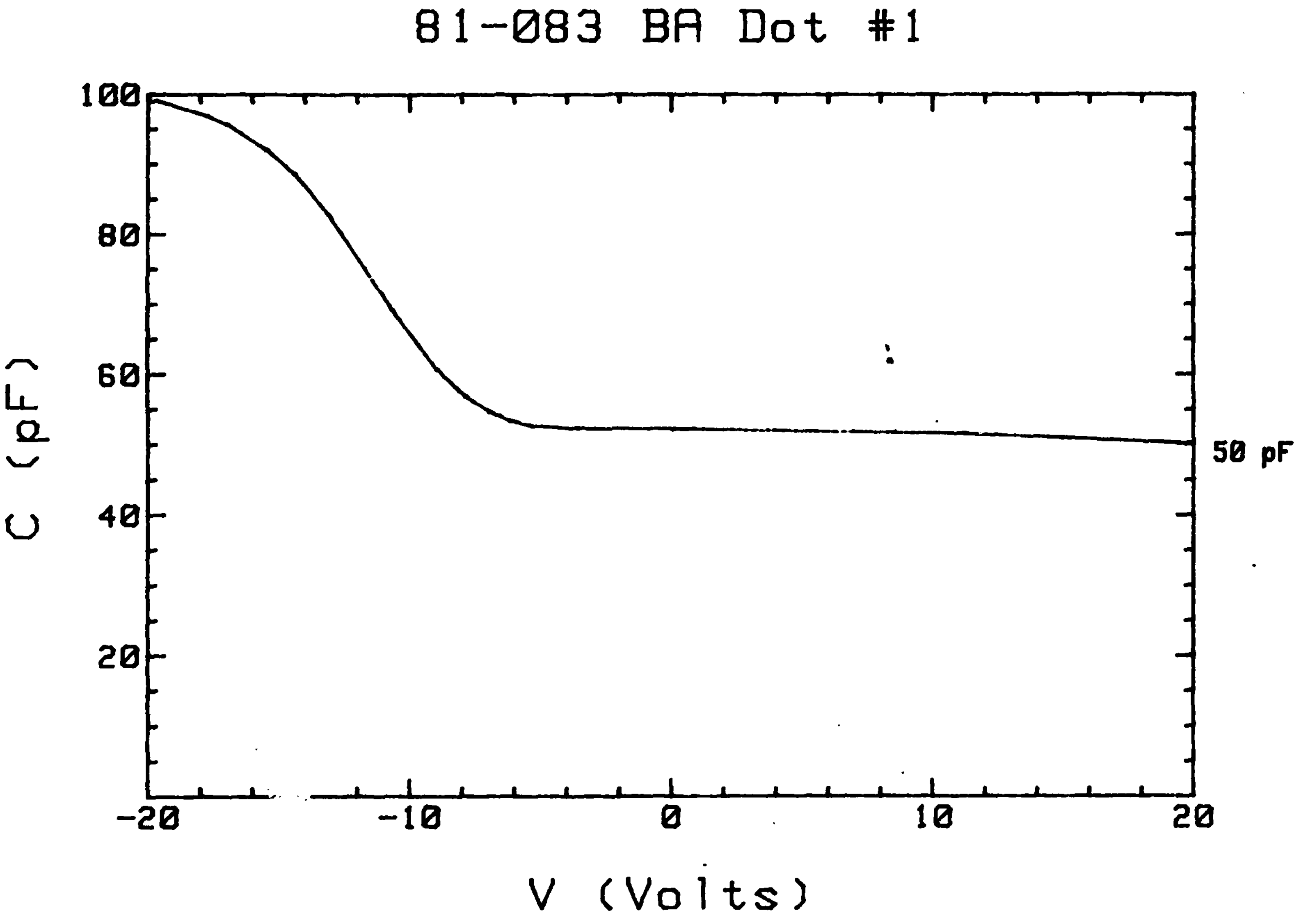

FIGURE 24c

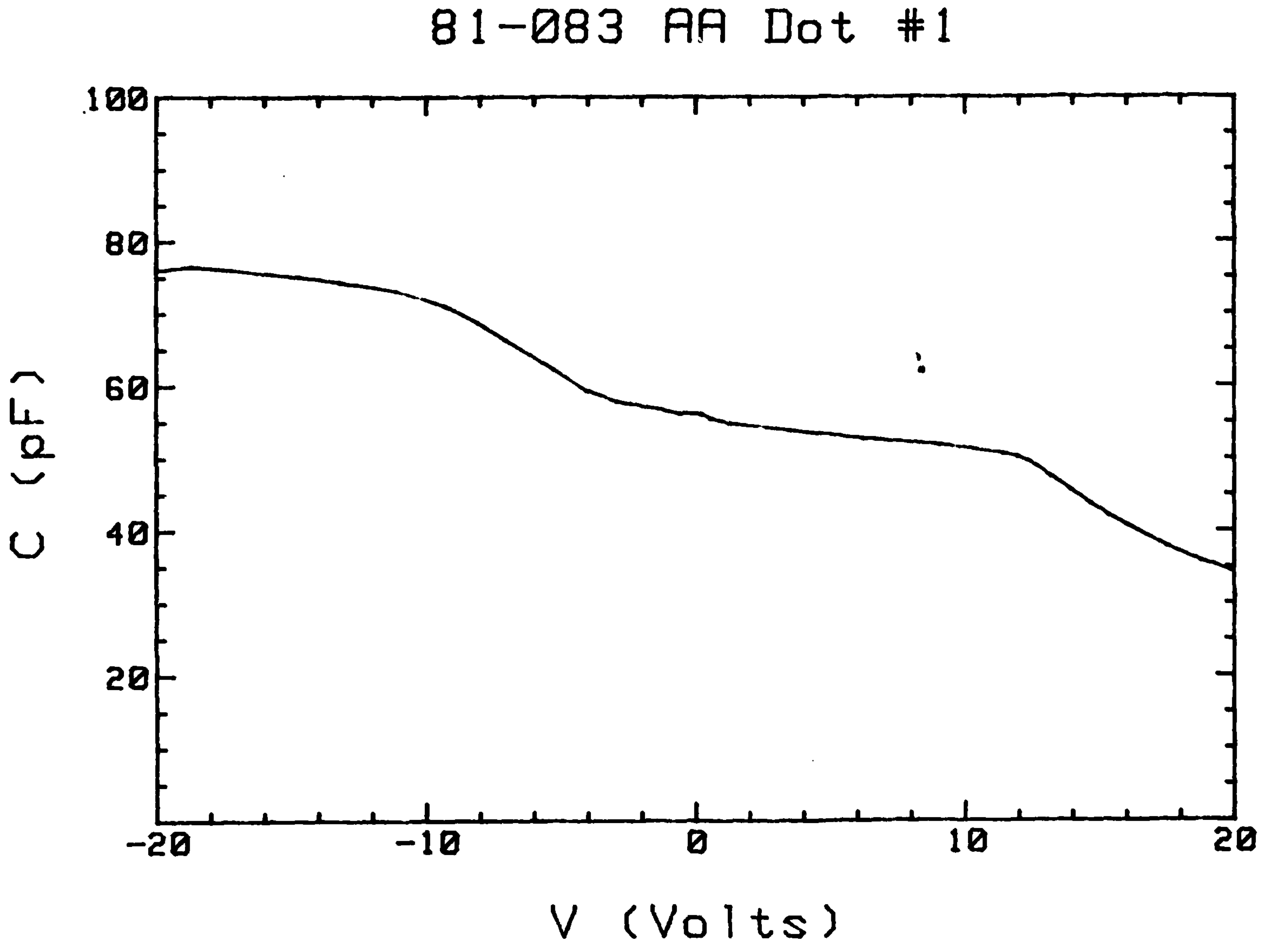

FIGURE 24d

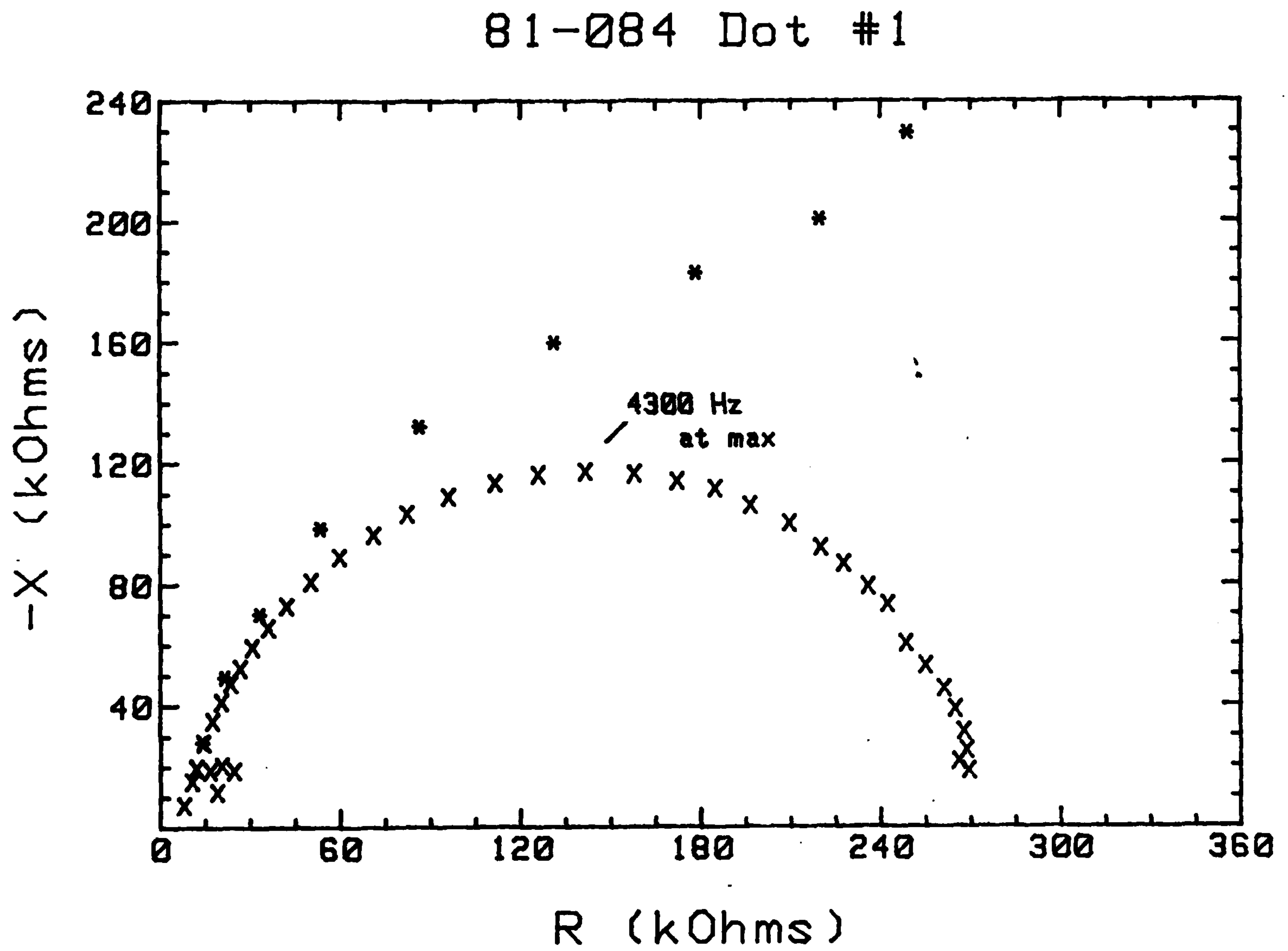

Oscillator
Amplitude : 50 mV

FIGURE 25

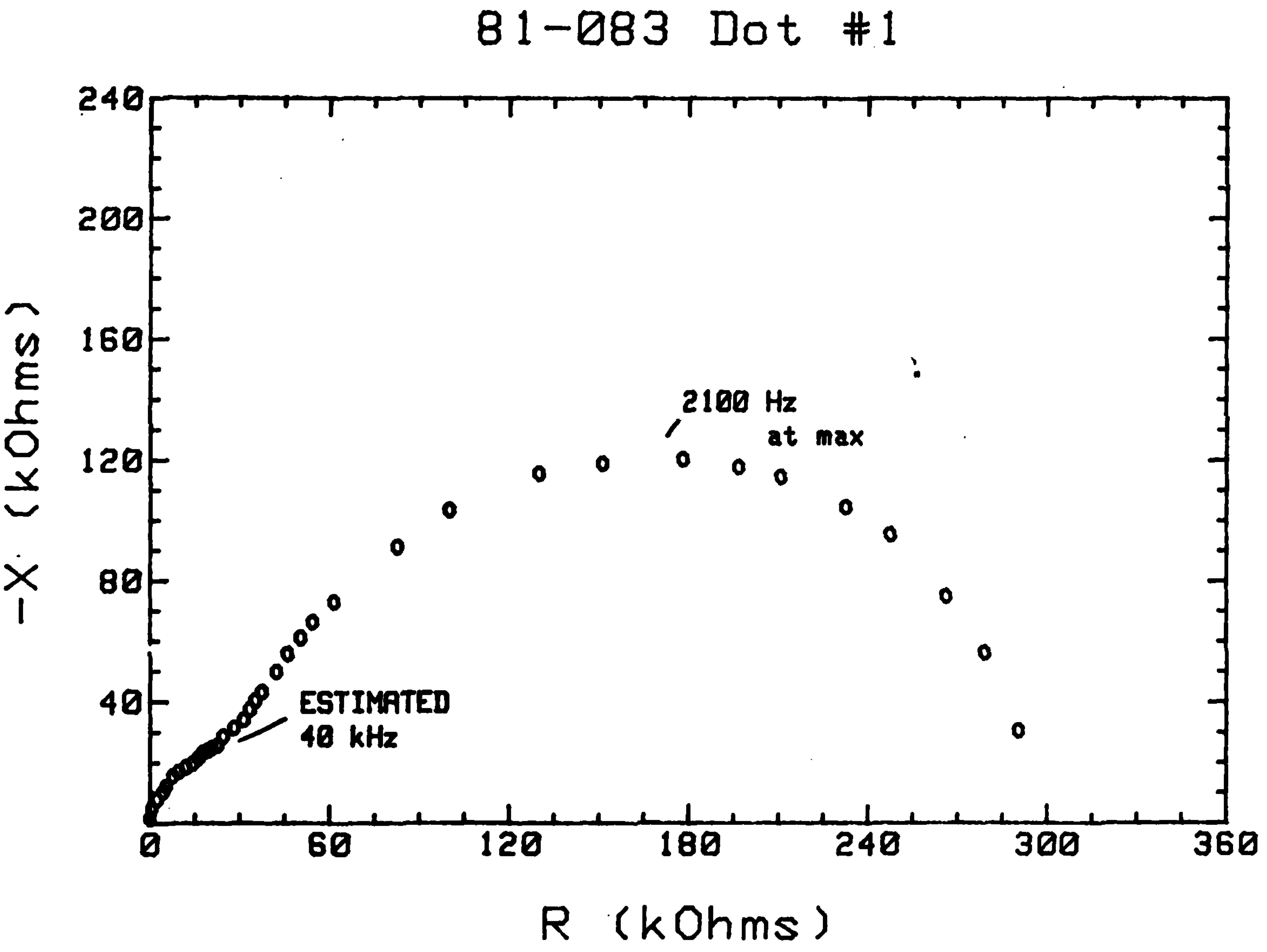

Oscillator
Amplitude : 1V

FIGURE 26

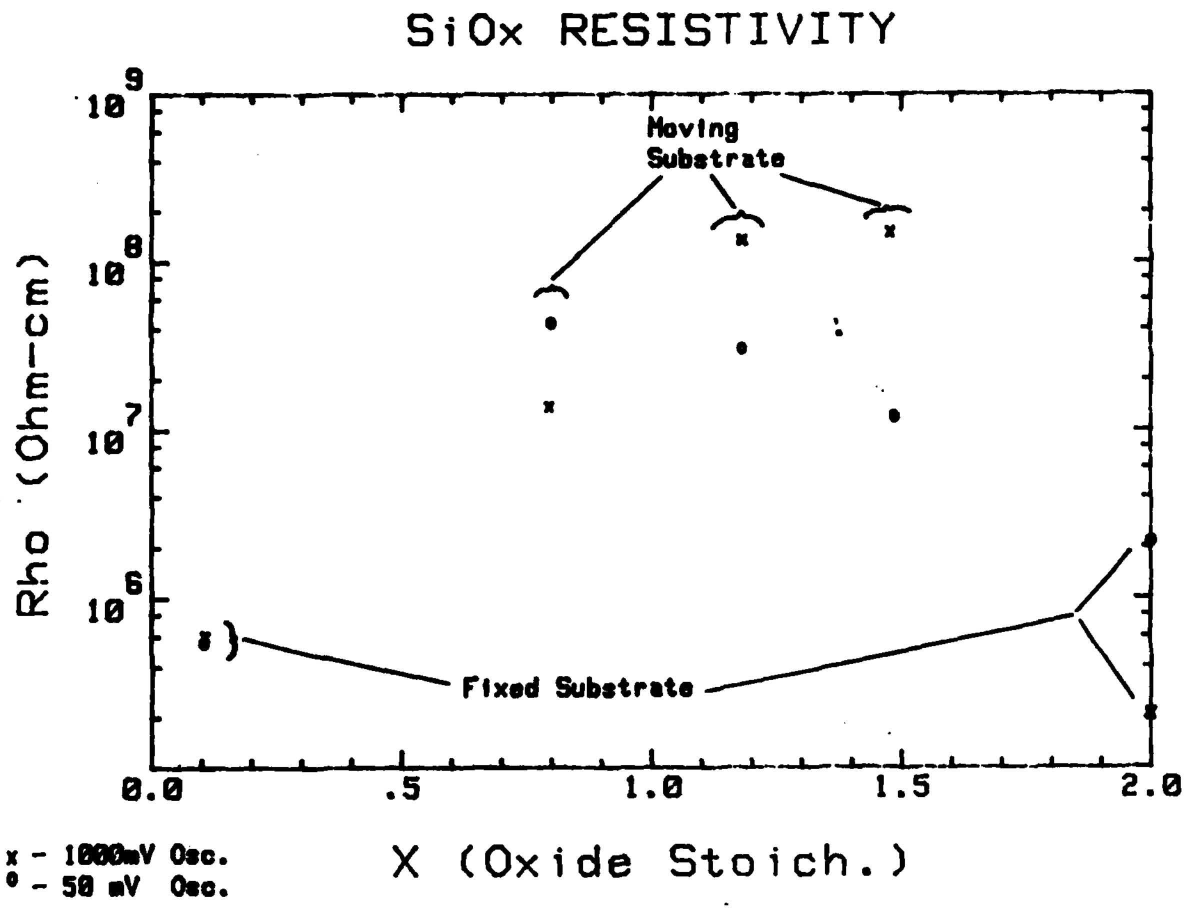
SiOx RESISTIVITY
Rho (Ohm-cm)
10^9
10^8
10^7
10^6
0.0
.5
1.0
1.5
2.0
X (Oxide Stoich.)
Moving Substrate
Fixed Substrate
x - 1000mV Osc.
• - 50 mV Osc.

FIGURE 27

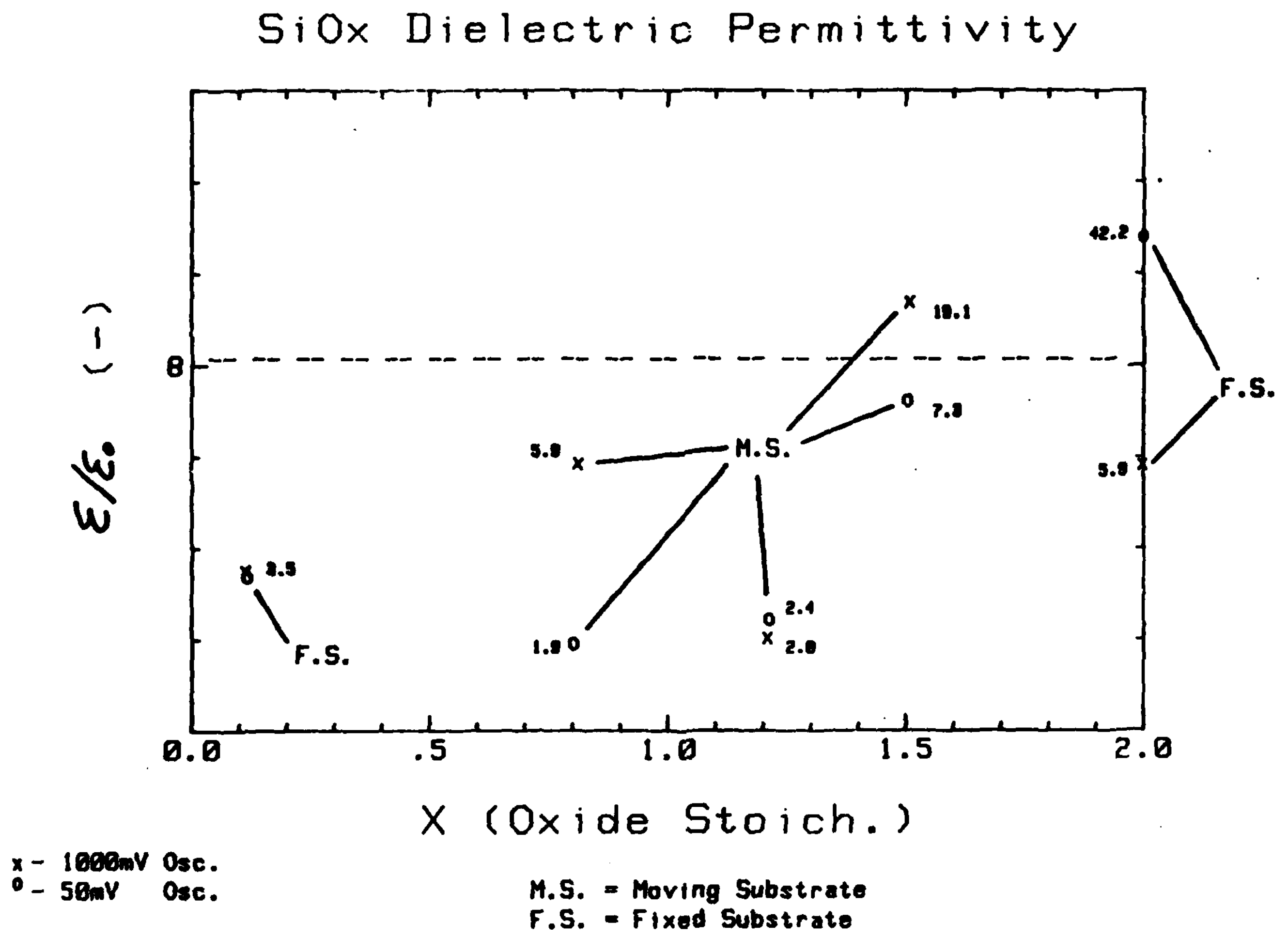
SiOx Dielectric Permittivity
ε/ε₀ (-)
8
0.0
.5
1.0
1.5
2.0
X (Oxide Stoich.)
3.5
F.S.
5.8
1.9
M.S.
19.1
7.3
2.4
2.8
42.2
5.8
F.S.
x - 1000mV Osc.
o - 50mV Osc.
M.S. = Moving Substrate
F.S. = Fixed Substrate

FIGURE 28

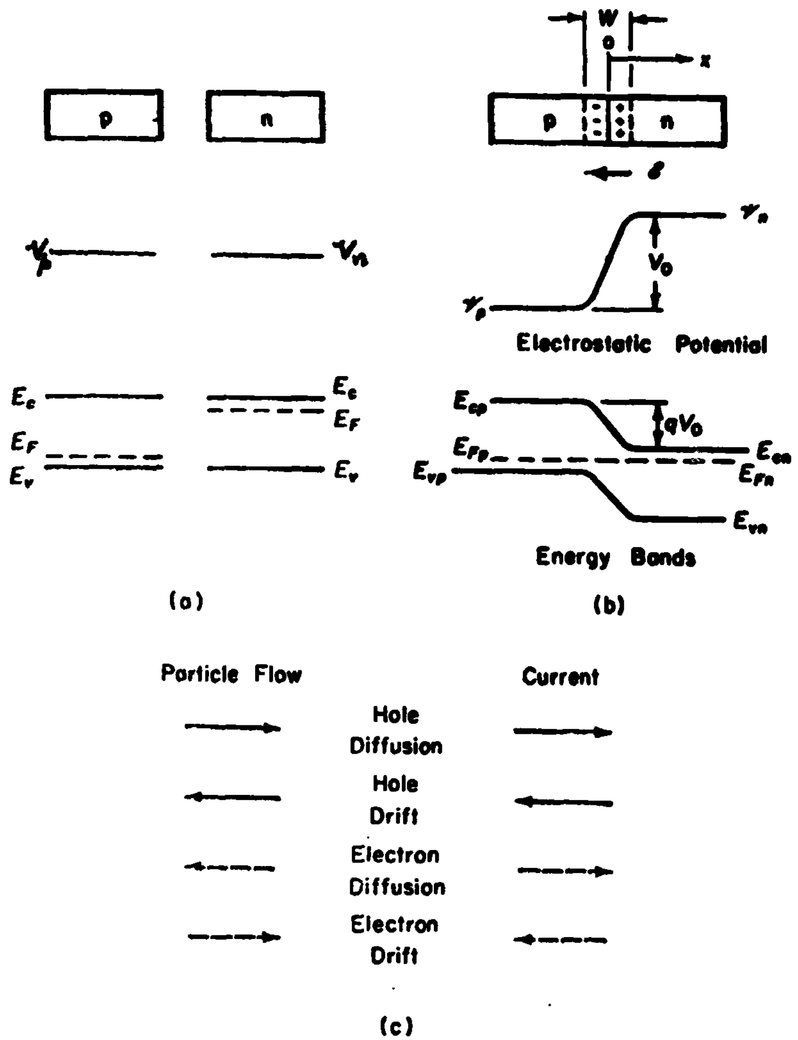

FIGURE 29

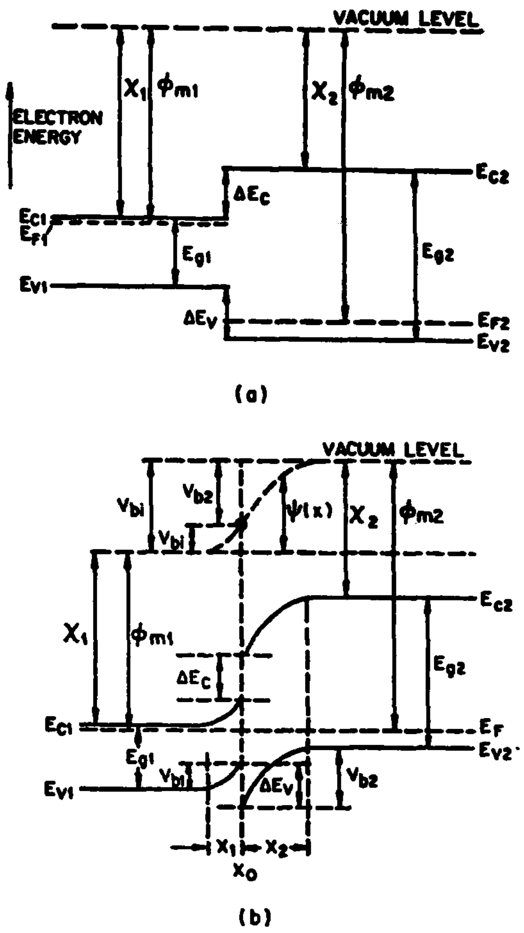

FIGURE 30

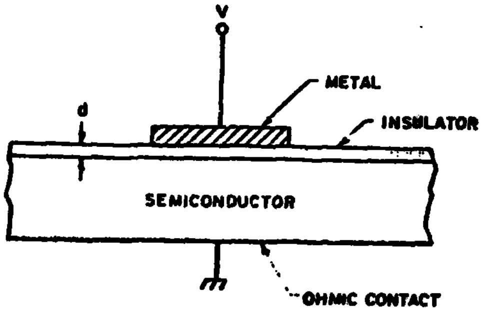

FIGURE 31a

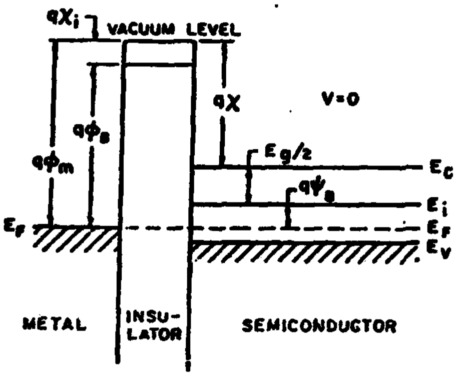

(b) IDEAL MIS DIODE (p-TYPE SEMICONDUCTOR)

FIGURE 31b

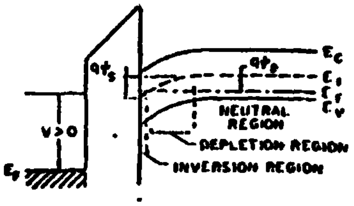

FIGURE 31c

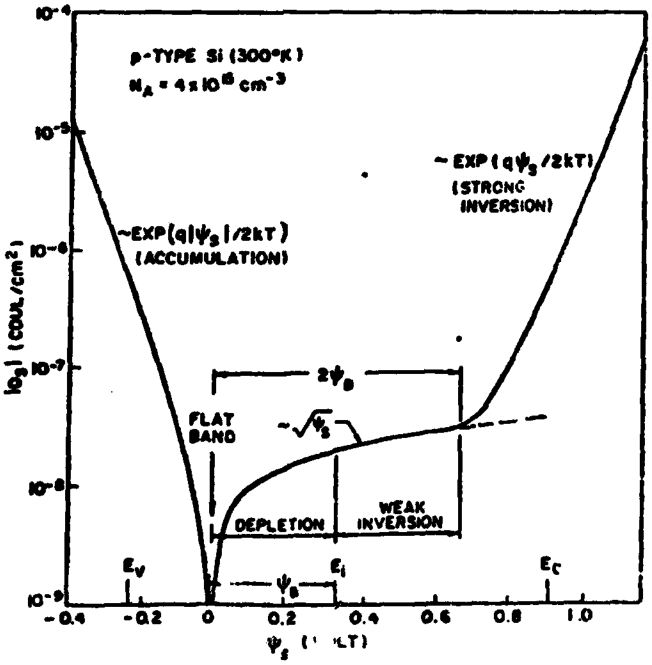

FIGURE 32

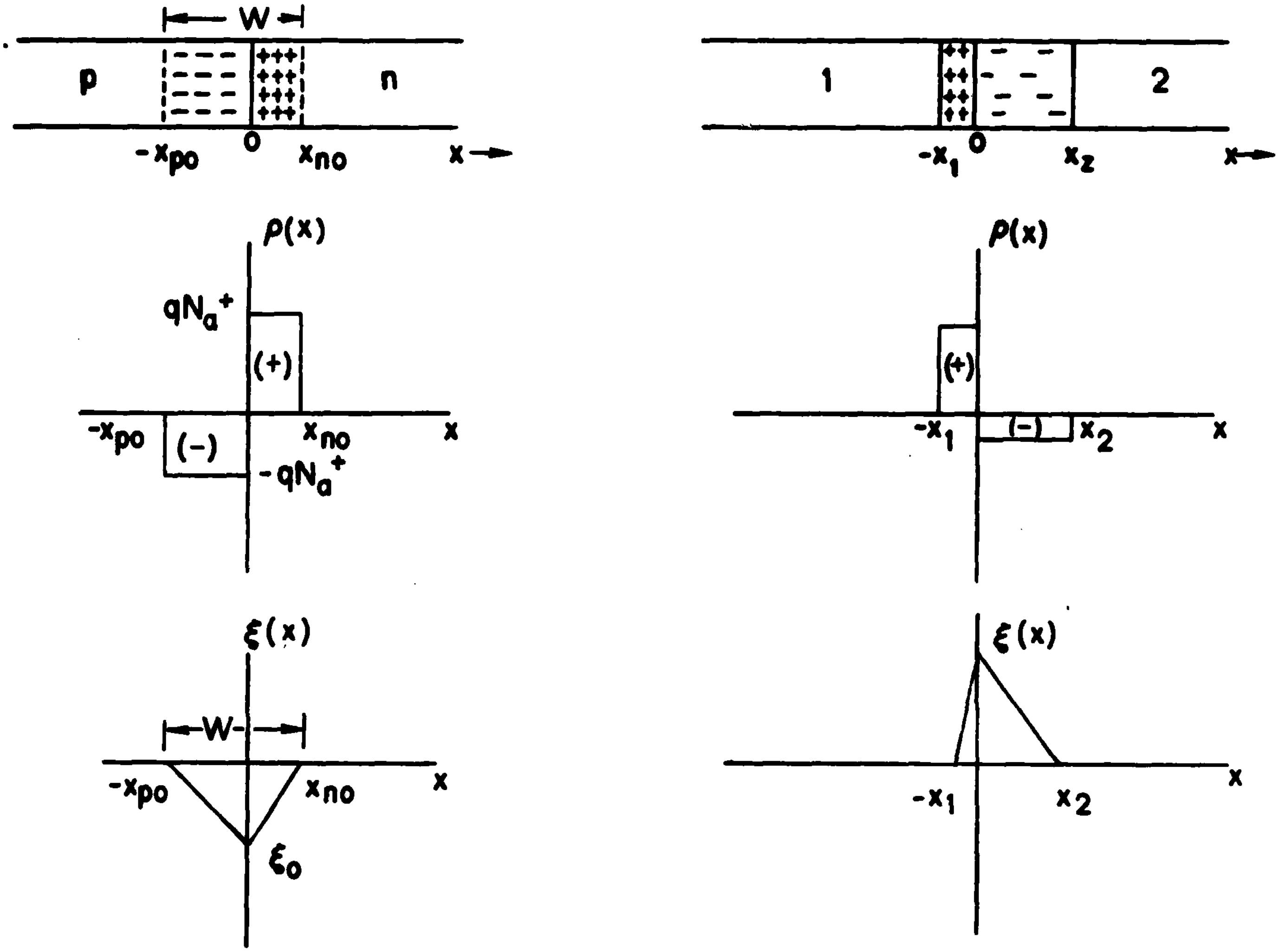
W
p
n
$-x_{po}$
0
x_{no}
x
1
2
$-x_1$
0
x_2
x
$\rho(x)$
qN_a^+
(+)
(−)
$-x_{po}$
x_{no}
$-qN_a^+$
x
$\rho(x)$
(+)
(−)
$-x_1$
x_2
x
$\xi(x)$
W
$-x_{po}$
x_{no}
x
ξ_o
$\xi(x)$
$-x_1$
x_2
x

FIGURE 33

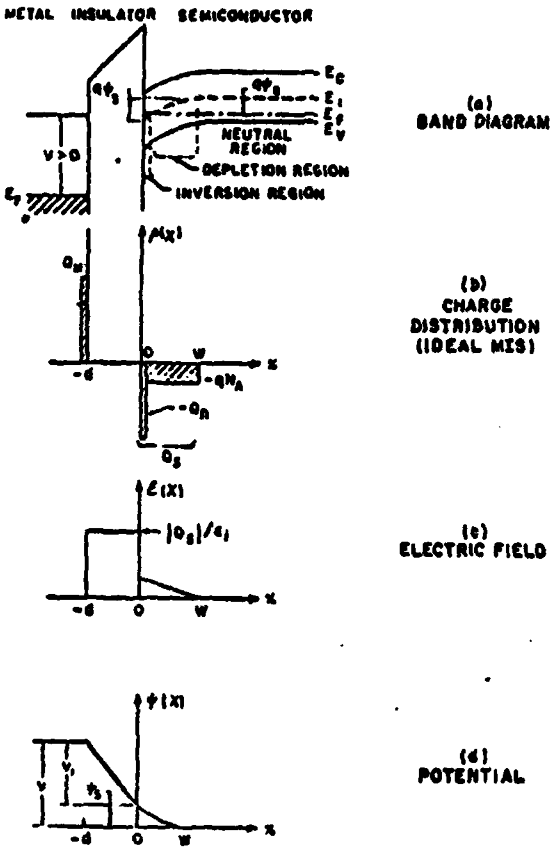

(a) BAND DIAGRAM

(b) CHARGE DISTRIBUTION (IDEAL MIS)

(c) ELECTRIC FIELD

(d) POTENTIAL

FIGURE 34

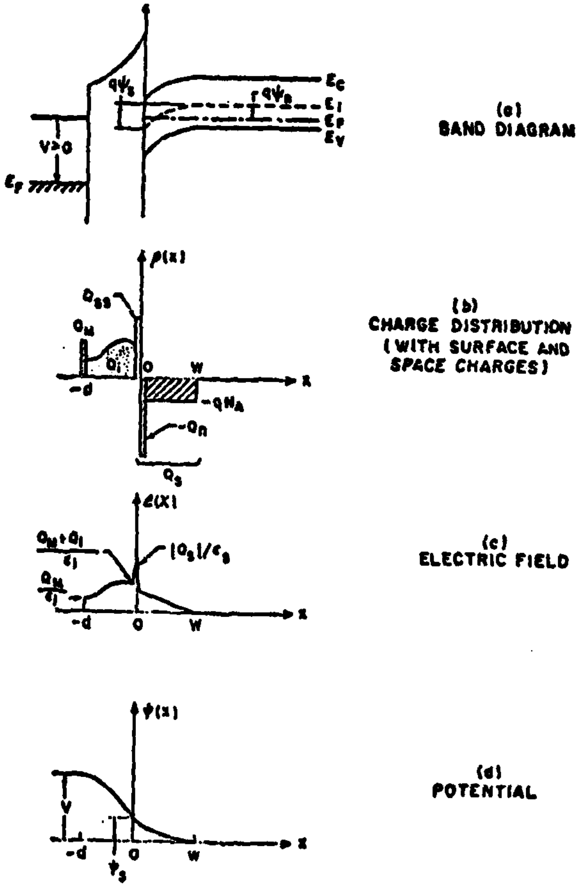

(a) BAND DIAGRAM

(b) CHARGE DISTRIBUTION (WITH SURFACE AND SPACE CHARGES)

(c) ELECTRIC FIELD

(d) POTENTIAL

FIGURE 35

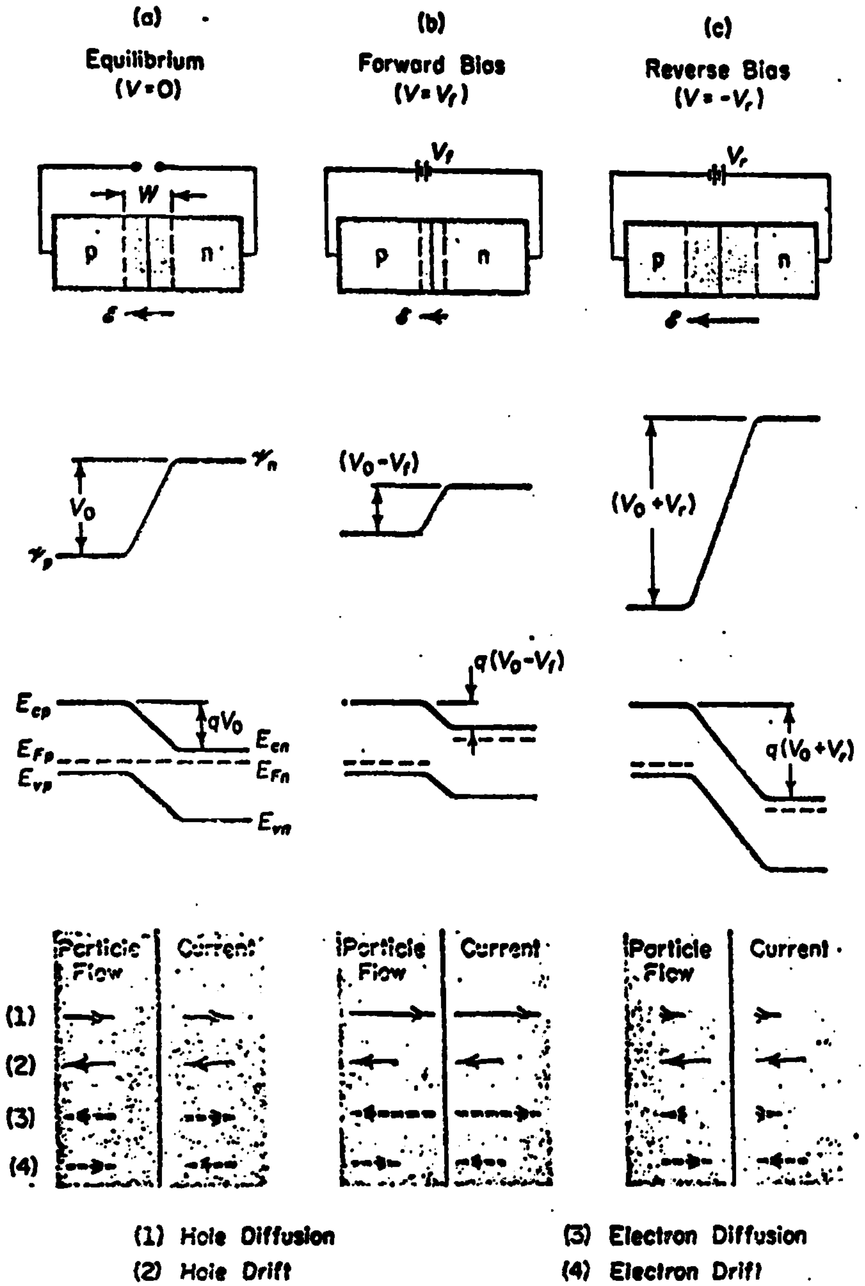

FIGURE 36

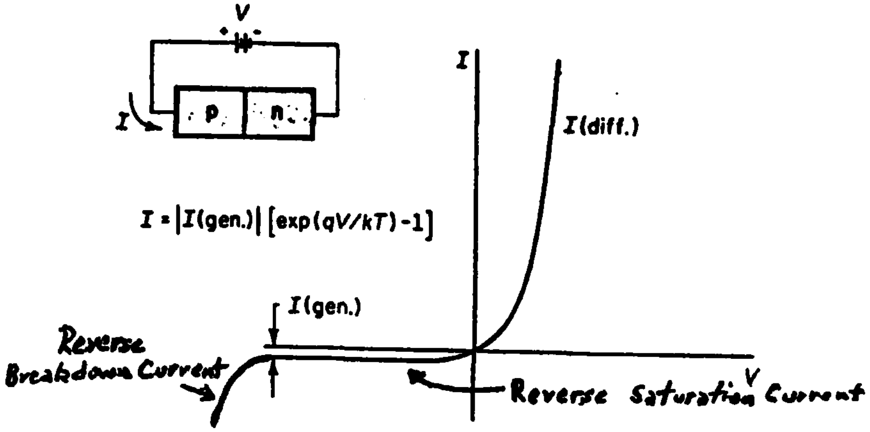

FIGURE 37

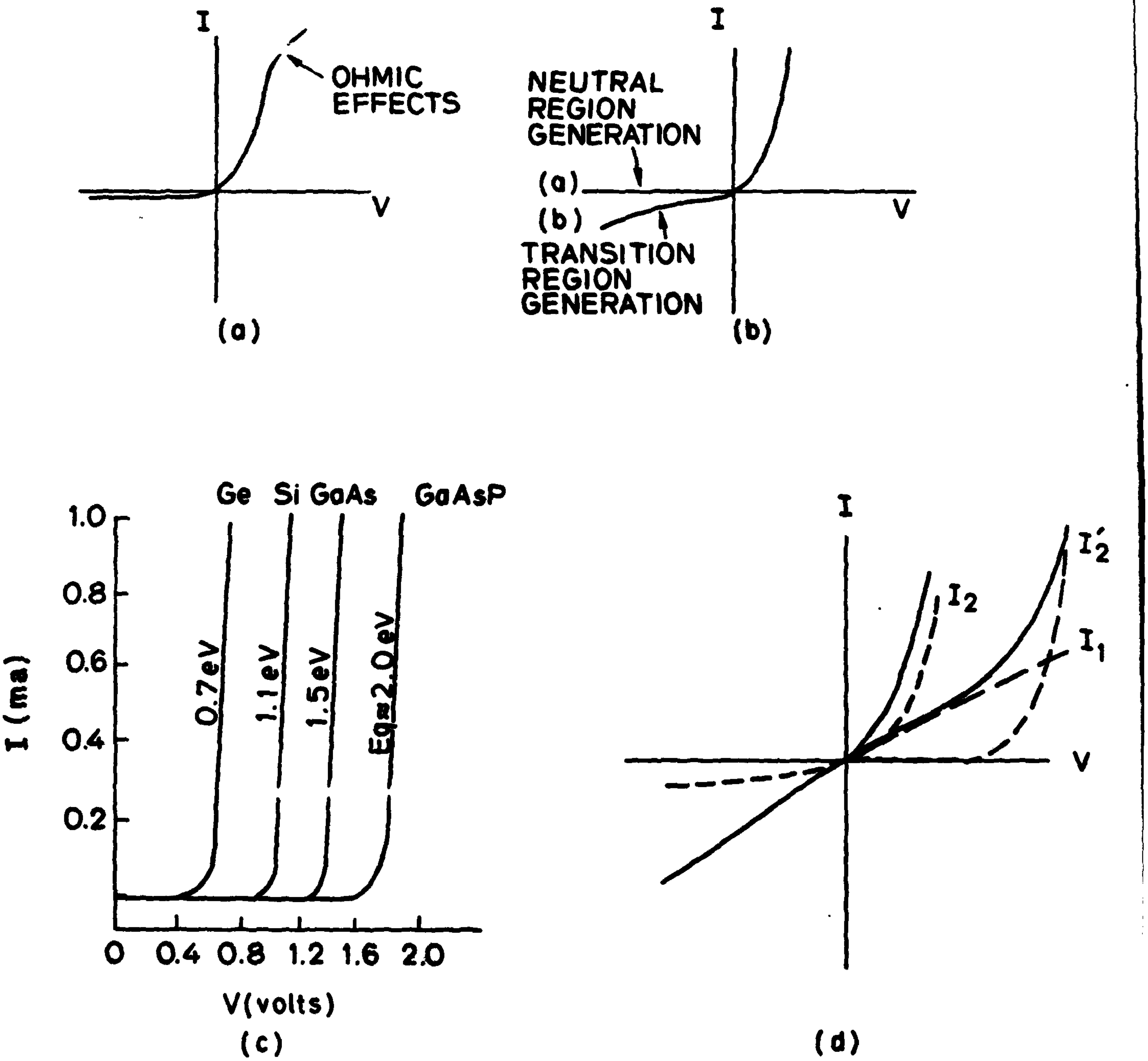
I
V
OHMIC EFFECTS
(a)
I
V
NEUTRAL REGION GENERATION
(a)
(b)
TRANSITION REGION GENERATION
(b)
Ge
Si
GaAs
GaAsP
1.0
0.8
0.6
0.4
0.2
0.7eV
1.1eV
1.5eV
Eg=2.0eV
I (ma)
0
0.4
0.8
1.2
1.6
2.0
V(volts)
(c)
I
I_2'
I_2
I_1
V
(d)

FIGURE 38

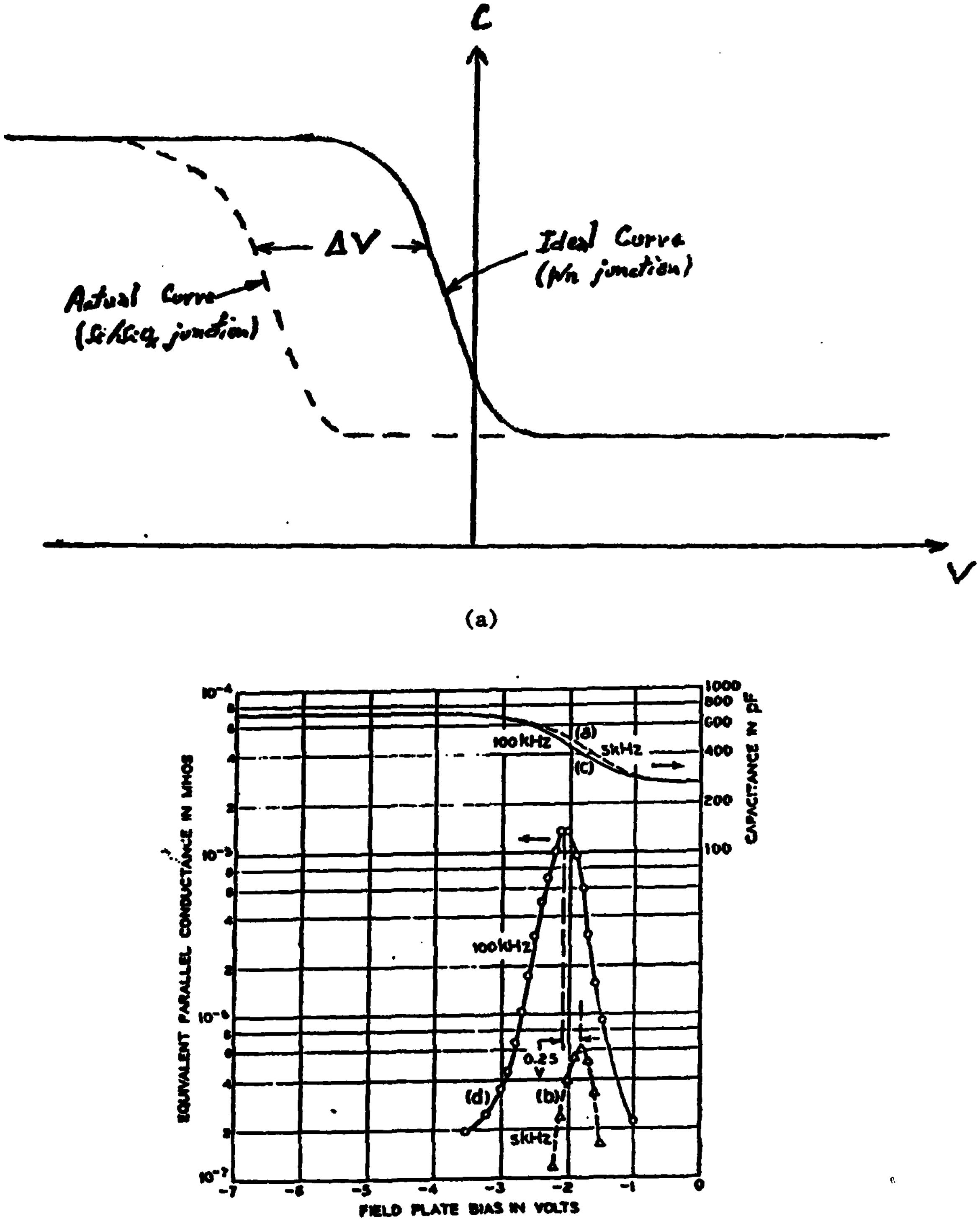
C
V
ΔV
Ideal Curve
(p/n junction)
Actual Curve
(Si/SiO$_x$ junction)
EQUIVALENT PARALLEL CONDUCTANCE IN MHOS
CAPACITANCE IN pF
FIELD PLATE BIAS IN VOLTS
10^{-4}
8
6
4
2
10^{-5}
10^{-6}
10^{-7}
1000
800
600
400
200
100
-7
-6
-5
-4
-3
-2
-1
0
100kHz
5kHz
(a)
(b)
(c)
(d)
0.25 V

(a)

(b)

FIGURE 39

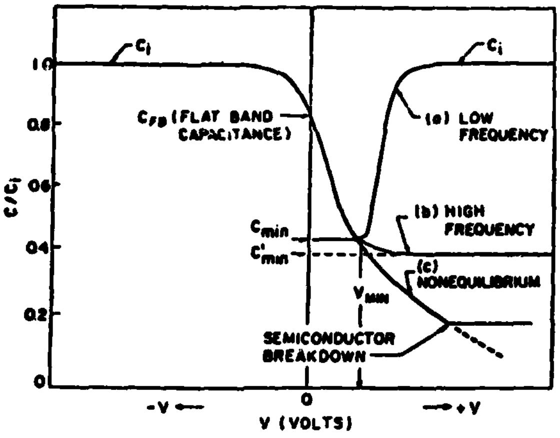

FIGURE 40

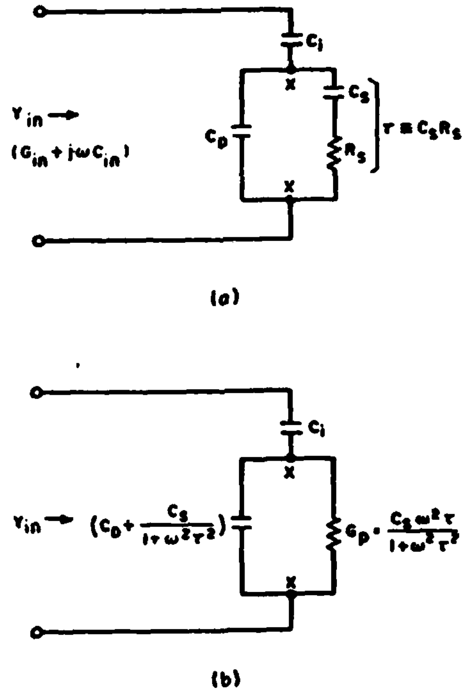

(a)

(b)

FIGURE 41

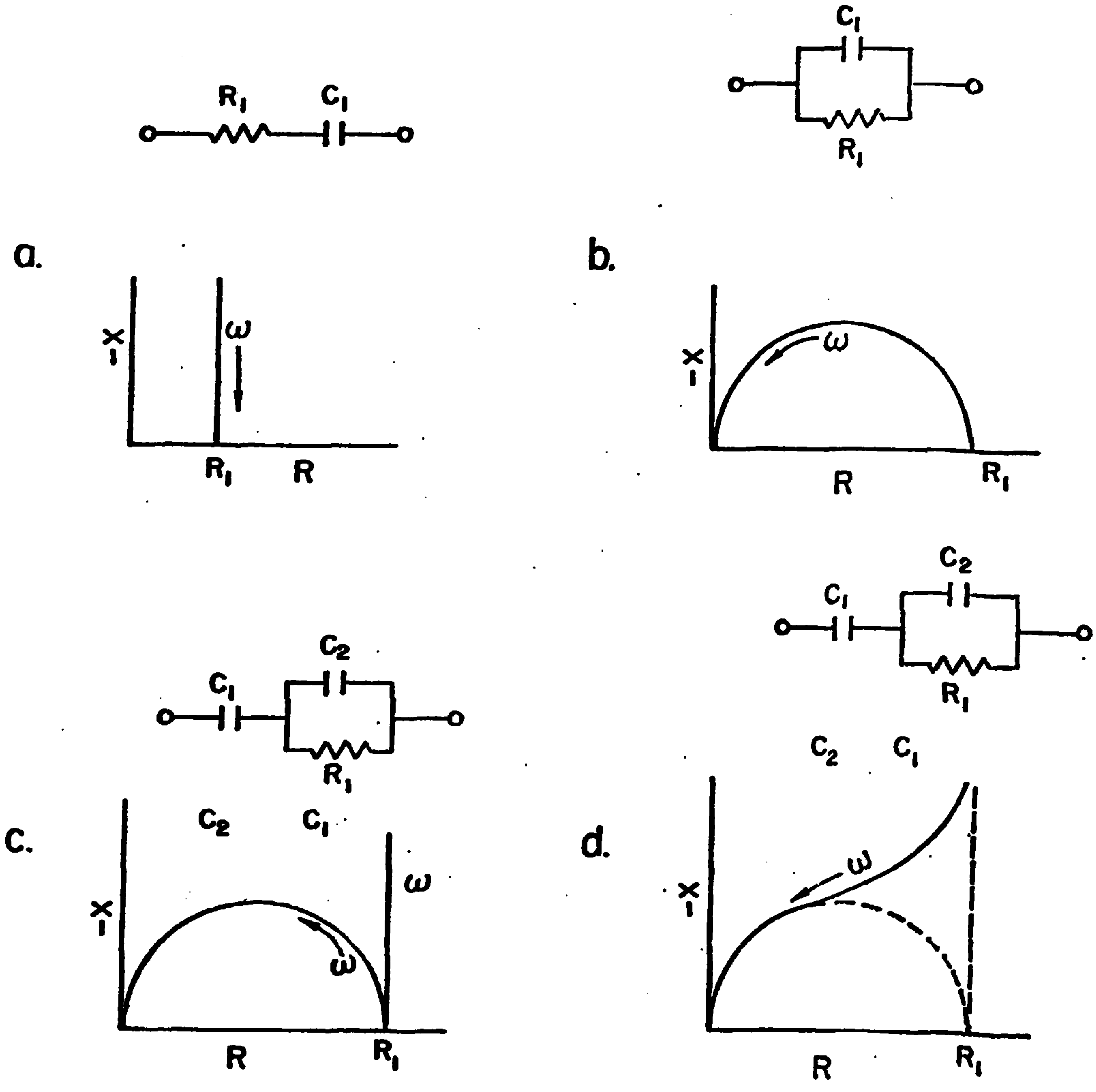

a.
R_1
C_1
X
ω
R_1
R
b.
C_1
R_1
X
ω
R
R_1
c.
C_2
C_1
R_1
C_2
C_1
X
ω
ω
R
R_1
d.
C_2
C_1
R_1
C_2
C_1
X
ω
R
R_1

FIGURE 42

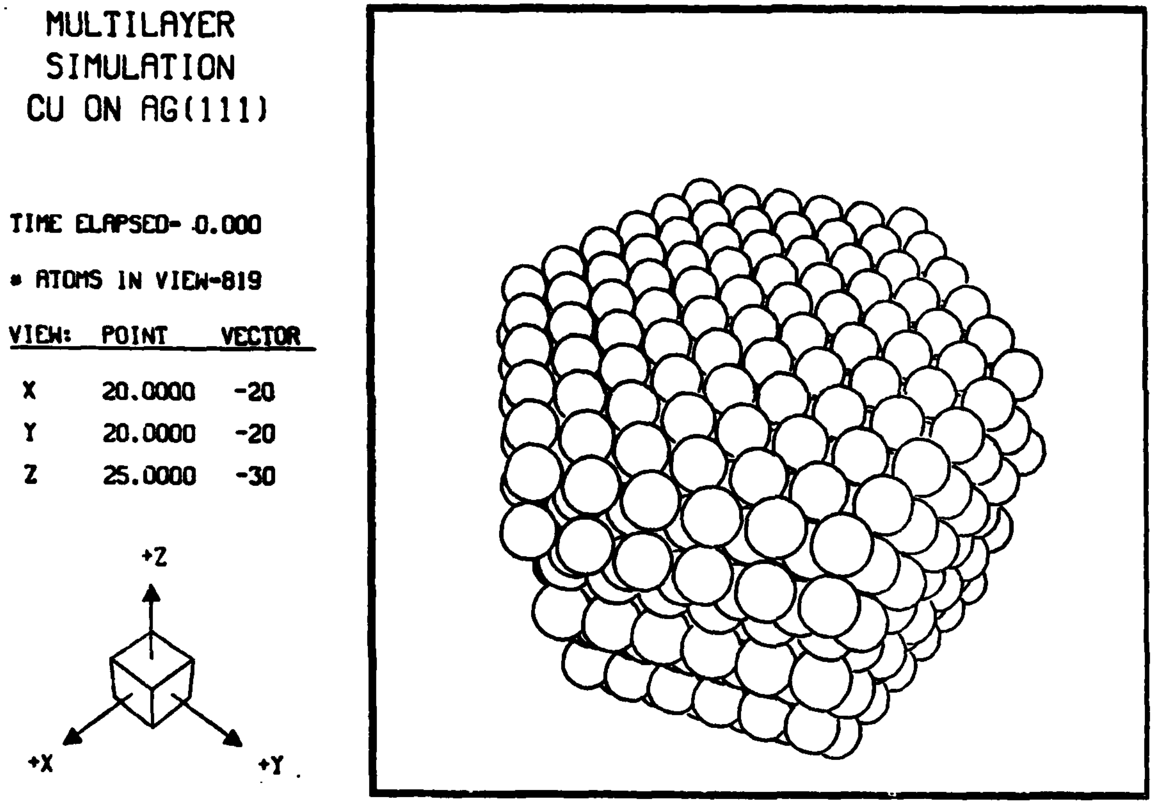

MULTILAYER
SIMULATION
CU ON AG(111)

TIME ELAPSED- 0.000

\# ATOMS IN VIEW=819

VIEW:	POINT	VECTOR
X	20.0000	-20
Y	20.0000	-20
Z	25.0000	-30

FIGURE 43

MULTILAYER
SIMULATION
CU ON AG(111)

TIME ELAPSED- 3.480×10^{-13}

ATOMS IN VIEW-796

VIEW:	POINT	VECTOR
X	10.0000	-10
Y	22.0000	-22
Z	10.0000	-15

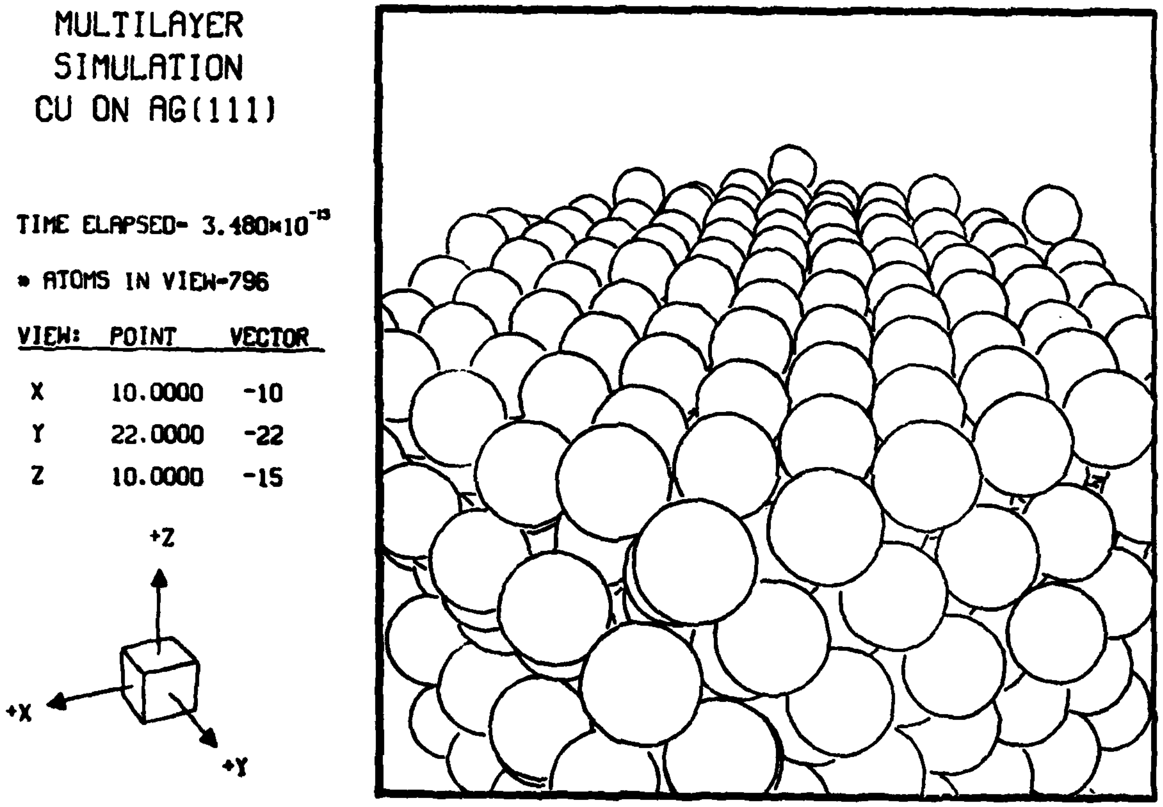

FIGURE 44

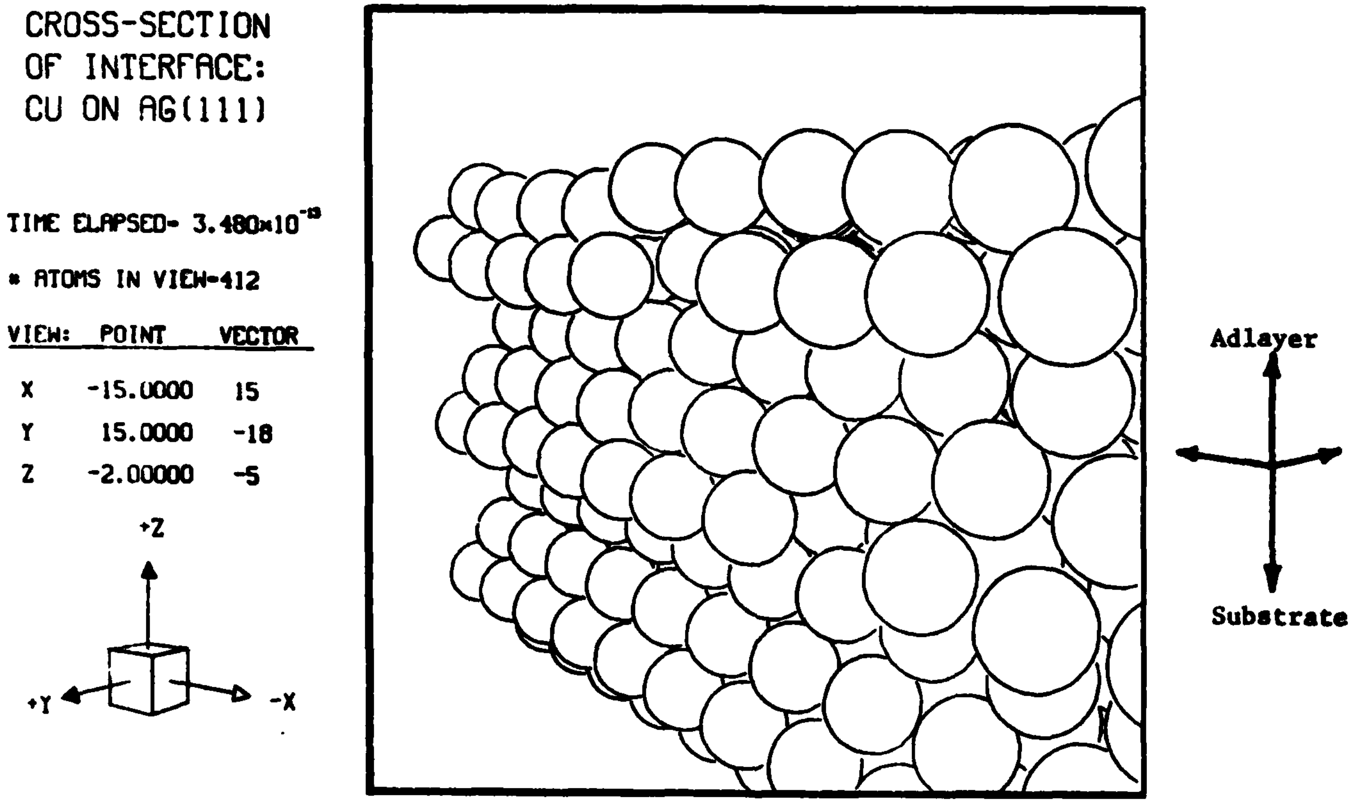
CROSS-SECTION
OF INTERFACE:
CU ON AG(111)
TIME ELAPSED- 3.480x10^-13
* ATOMS IN VIEW-412
VIEW: POINT VECTOR
X -15.0000 15
Y 15.0000 -18
Z -2.00000 -5
+Z
+Y
-X
Adlayer
Substrate

FIGURE 45

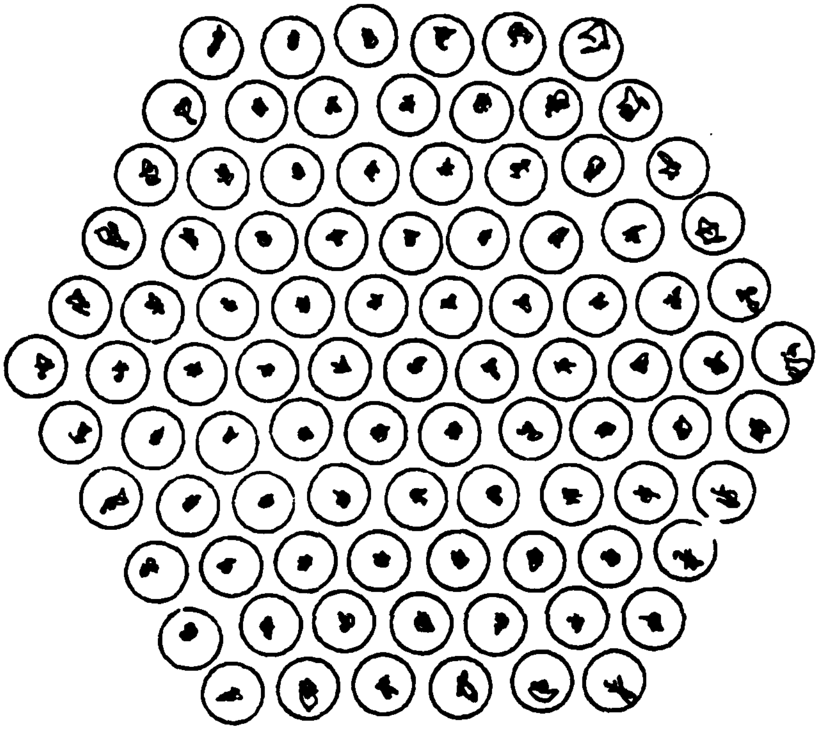

FIGURE 46

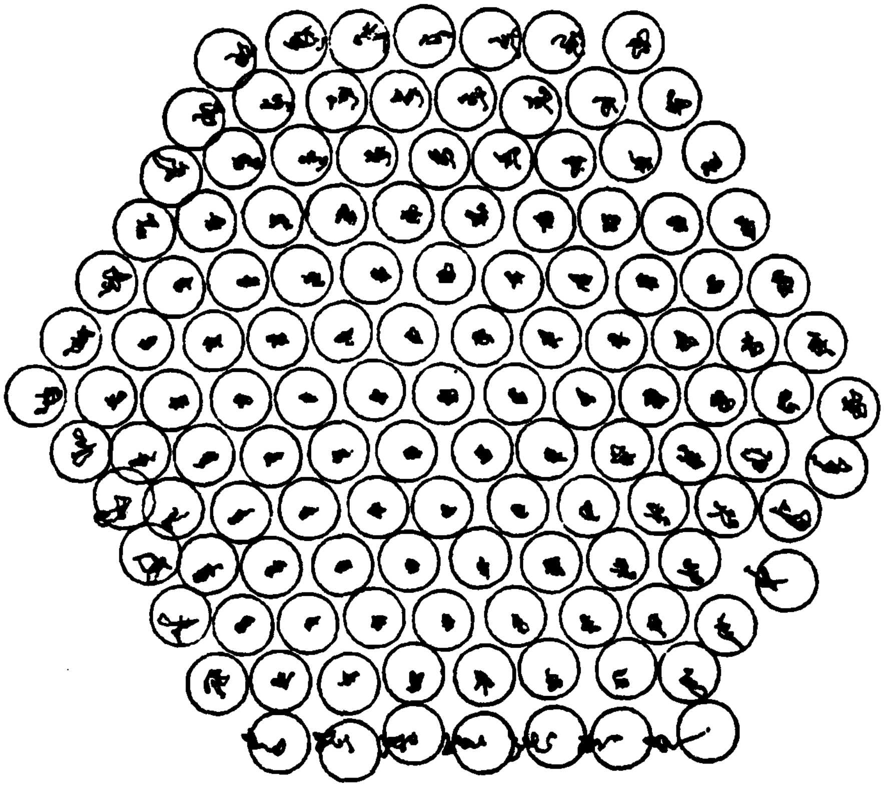

FIGURE 47

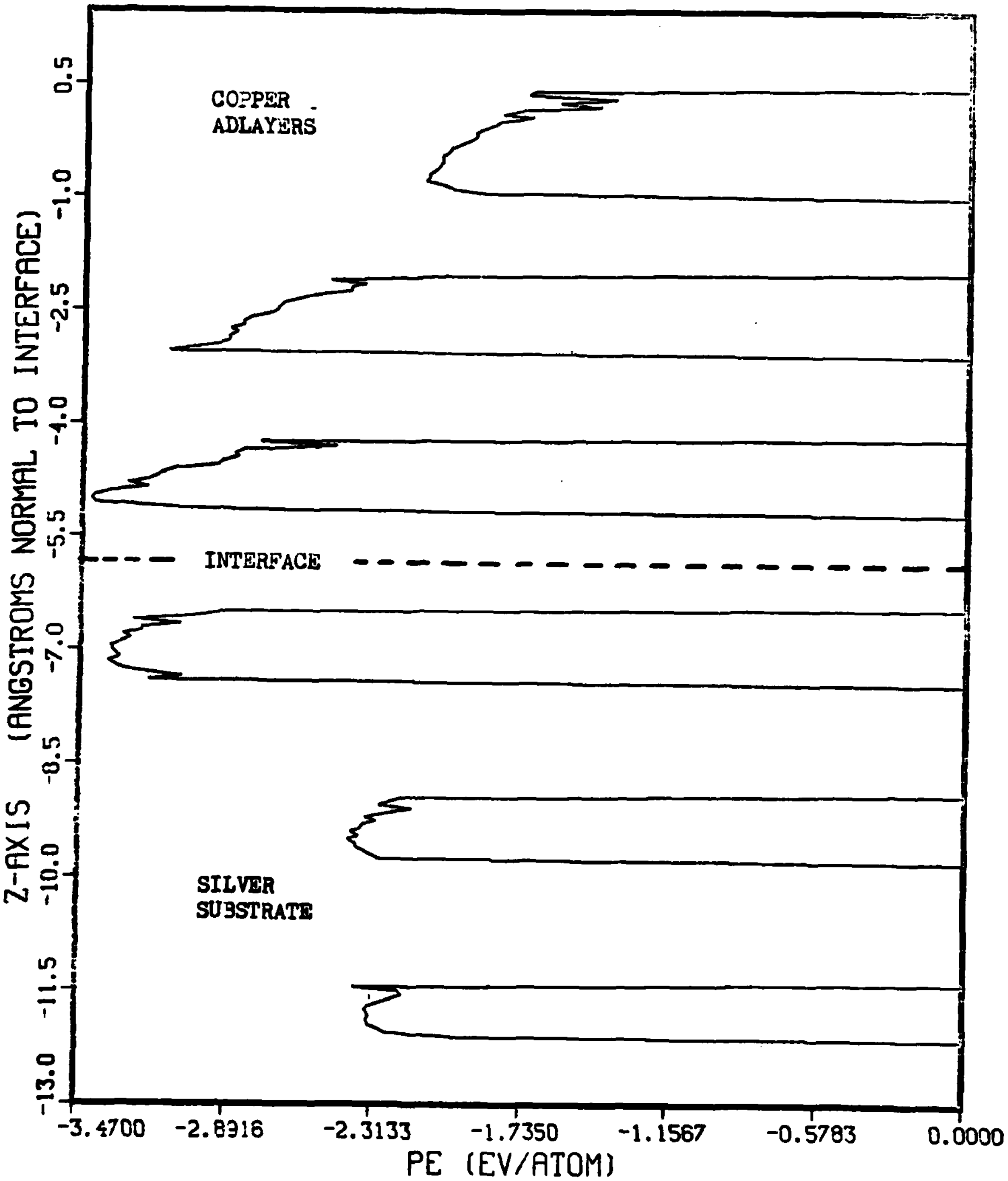
COPPER
ADLAYERS
INTERFACE
SILVER
SUBSTRATE
Z-AXIS (ANGSTROMS NORMAL TO INTERFACE)
0.5
-1.0
-2.5
-4.0
-5.5
-7.0
-8.5
-10.0
-11.5
-13.0
-3.4700
-2.8916
-2.3133
-1.7350
-1.1567
-0.5783
0.0000
PE (EV/ATOM)

FIGURE 48

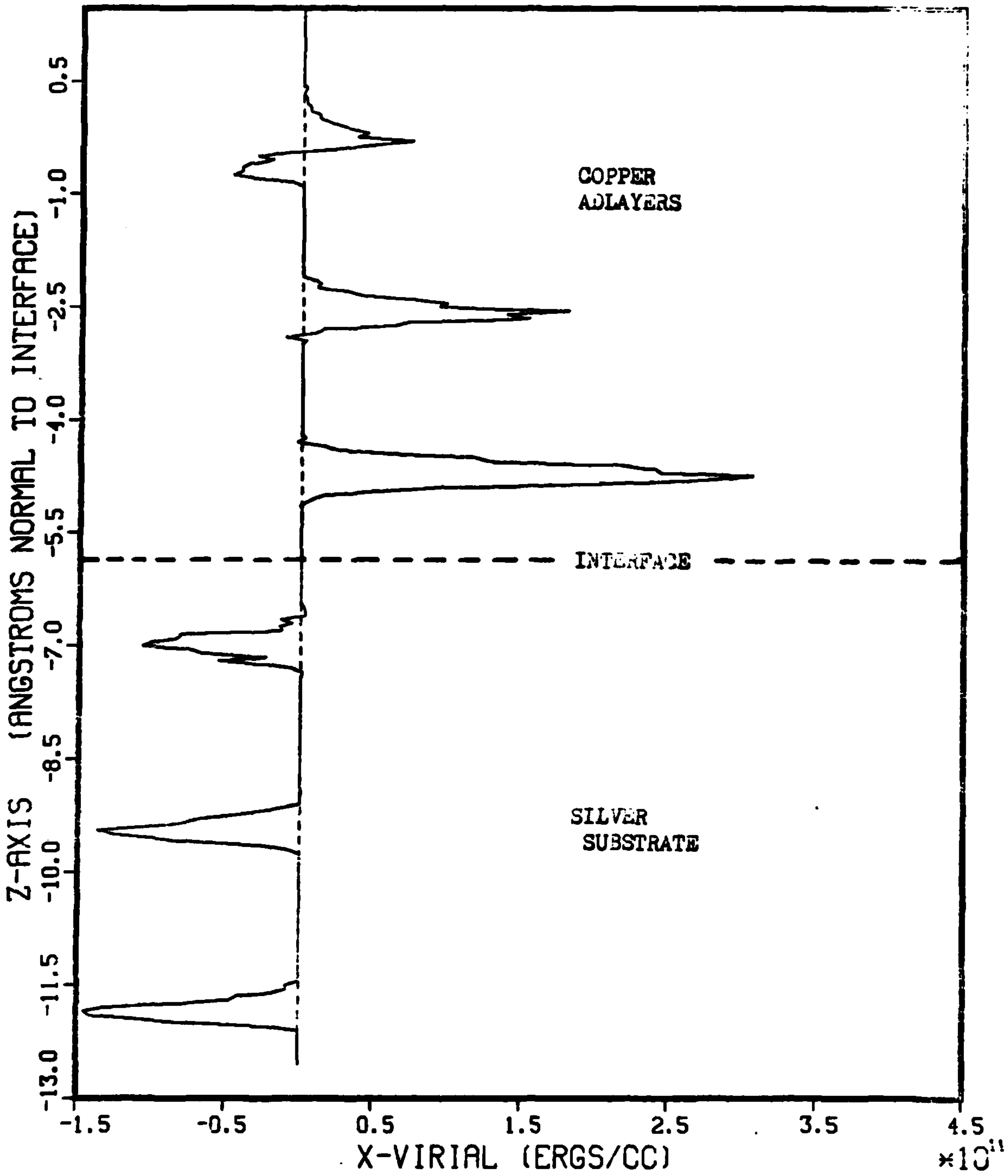
COPPER
ADLAYERS
INTERFACE
SILVER
SUBSTRATE
Z-AXIS (ANGSTROMS NORMAL TO INTERFACE)
0.5
-1.0
-2.5
-4.0
-5.5
-7.0
-8.5
-10.0
-11.5
-13.0
-1.5
-0.5
0.5
1.5
2.5
3.5
4.5
X-VIRIAL (ERGS/CC)
×10¹¹

FIGURE 49